# Project 055 Noise Generation and Propagation from Advanced Combustors

## Georgia Institute of Technology
## Raytheon Technologies Research Center

## Project Lead Investigator

Timothy Lieuwen
Professor
Daniel Guggenheim School of Aerospace Engineering
Georgia Institute of Technology
270 Ferst Drive (M/C 0150)
Atlanta, GA 30332-0150
404-894-3041
tim.lieuwen@aerospace.gatech.edu

## University Participants

**Georgia Institute of Technology (GT)**

- P.I.s: Prof. Timothy Lieuwen, Prof. Suresh Menon, Prof. Adam Steinberg, Dr. Vishal Acharya, Benjamin Emerson, David Wu
- FAA Award Number: 13-C-AJFE-GIT-058
- Period of Performance: February 5, 2020 to September 30, 2024
- Tasks:
    1. **Facility development at GT**
       This task addresses the design of experiments that will be performed at GT. The task involves coordination between the teams to develop and define the aerodynamic design of a rich-quench-lean (RQL), quick quench, lean burn combustor for this study. This task is led by Tim Lieuwen and Adam Steinberg, with support from Ben Emerson and David Wu.
    2. **Simulations of the GT experiment**
       This task includes simulating the GT experiment, with a focus on the pre-combustion flow dynamics, flame dynamics, and post-combustion dynamics of pressure and entropy disturbances. This task is led by Suresh Menon.
    3. **Reduced-order modeling**
       This task consists of creating a reduced-order model (ROM) framework for the unsteady response of the flame and the generation of entropy disturbances due to unsteady heat release. This task is led by Vishal Acharya.

**Raytheon Technologies Research Corporation (RTRC)**

- P.I.s: Dr. Jeffrey Mendoza, Dr. Duane McCormick, Dr. Julian Winkler, Dr. Lance Smith
- FAA Award Number: 13-C-AJFE-GIT-058 (subaward through GT)
- Period of Performance: February 5, 2020 to September 30, 2024
- Tasks:
    4. **Facility development at RTRC**
       This task addresses the design of experiments that will be performed at RTRC. The task involves coordination between the teams to develop and define the aerodynamic design of an RQL combustor for this study. This task is led by Jeffrey Mendoza, Lance Smith, and Duane McCormick.
    5. **Post-combustion modeling**
       This task consists of both post-processing and simulation efforts. First, the post-combustion simulation data from the simulation of the GT experiment are mined to investigate the dynamics of entropy

fluctuations and their transport. Next, simulations are used to model noise propagation in the post-combustion architecture of the engine. The simulations are split across the different sections: nozzle, turbine, and far-field. This task is led by Jeffrey Mendoza and Julian Winkler.

## Project Funding Level

**FAA funding:** $4,500,000 (GT: $2,500,000; RTRC: $2,000,000)
**Cost-sharing:** $4,273,000 (GT: $2,273,000 from AE school; RTRC: $2,000,000 from company funds)
**Total funding:** $8,773,000

## Investigation Team

**Georgia Institute of Technology**

Prof. Tim Lieuwen, (P.I.), lead P.I. responsible for overseeing all tasks; specifically, he leads the GT experiments and design in Tasks 1 and 2, along with Professor Steinberg. In addition, he co-leads the modeling tasks in Task 1 for pre-combustion, flame response, and post-combustion modeling, along with Dr. Acharya.
Prof. Adam Steinberg, (co-P.I.), responsible for design of experiment diagnostics and measurements.
Prof. Suresh Menon, (co-P.I.), responsible for simulations of the GT experiment.
Dr. Vishal Acharya, (co-P.I.; principal research engineer), responsible for all modeling tasks for the pre-combustion, combustion, and post-combustion physics, along with Professor Lieuwen. In addition, as administrative coordinator, he is responsible for general project management, such as project deliverables, group meetings, and interfacing with the FAA project manager.
Dr. Benjamin Emerson, (co-P.I.; principal research engineer), responsible for designing and maintaining experimental facilities, as well as experimental operations and management, and graduate students' safety.
David Wu, (co-P.I.; research engineer-II), responsible for designing and maintaining experimental facilities, as well as experimental operations and management, and graduate students' safety.
Dr. Achyut Panchal, (research engineer), simulation of the GT experiment.
Shivam Patel, (graduate student), maintenance, construction, and operation of the experiment at GT.
Sungyoung Ha, (graduate student), lead experimentalist on the GT rig.
Jananee, (graduate student), responsible for optical diagnostics on the GT rig.
Parth Patki, (graduate student), the hydrodynamics modeling subtask (pre-combustion disturbances).

**Raytheon Technologies Research Corporation**

Dr. Jeffrey Mendoza, (P.I.; technical fellow acoustics), leads the RTRC team and oversees its contributions to the project. He leads the subtasks related to modeling, measurements, and simulation for post-combustion disturbances, nozzle interactions, turbine interactions, and far-field sound propagation.
Dr. Lance Smith, (co-P.I.; technical fellow combustion), design and measurements of the RTRC experiment. He works closely with the GT team to ensure similarities between both experiment setups.
Dr. Duane McCormick, (co-P.I.; principal research engineer), design and measurements of the RTRC experiment as well as finite-element calculations in the design process.
Dr. Julian Winkler, (co-P.I.), responsible for the simulation tasks at RTRC and focuses on post-combustion disturbances, nozzle interactions, turbine interactions, and far-field sound propagation.
Dr. Jordan Snyder, design, measurements, and data processing using tunable diode laser absorption spectroscopy and chemiluminescence in the RTRC combustor rig.
Dr. Kenji Homma, far-field sound propagation simulations.
Dr. Aaron Reimann, ROM and high-fidelity (HiFi) modeling of the propagation of direct and indirect noise sources through the turbine nozzle and supports the far-field sound propagation simulations.
Dr. Sudarshan Koushik, post-processing the GT large eddy simulation (LES) data to model post-combustion disturbances.

## Project Overview

The objective of this project is to develop and validate physics-based design tools that can predict noise production mechanisms and their relative dominance, and ultimately reduce the noise output of future engines. The motivation for this project stems from recent and future advances in aircraft engine technology. High-bypass engine technology has significantly reduced the traditionally dominant engine noise sources, namely fan and jet exhaust noise. Noise generated in the combustor has become a dominant source of engine noise for future advanced aircraft designs. In addition, as

combustors evolve to increase efficiency and decrease pollutant emissions, methods for predicting and mitigating combustion noise have severely lagged, and legacy methods are insufficient to predict noise from next-generation combustors. This drawback has motivated the objective of this project, which addresses the critical need for physics-based design tools. The resultant understanding of noise generation and propagation, along with validated noise prediction tools, will enable more rapid and cost-effective designs of low-noise engines for future aircraft.

The project objectives will be achieved through a program of cooperative experiments, high-fidelity simulations, and physics-based ROM. The physical processes involved are tightly coupled and directly determine the project tasks, as shown in Figure 1.

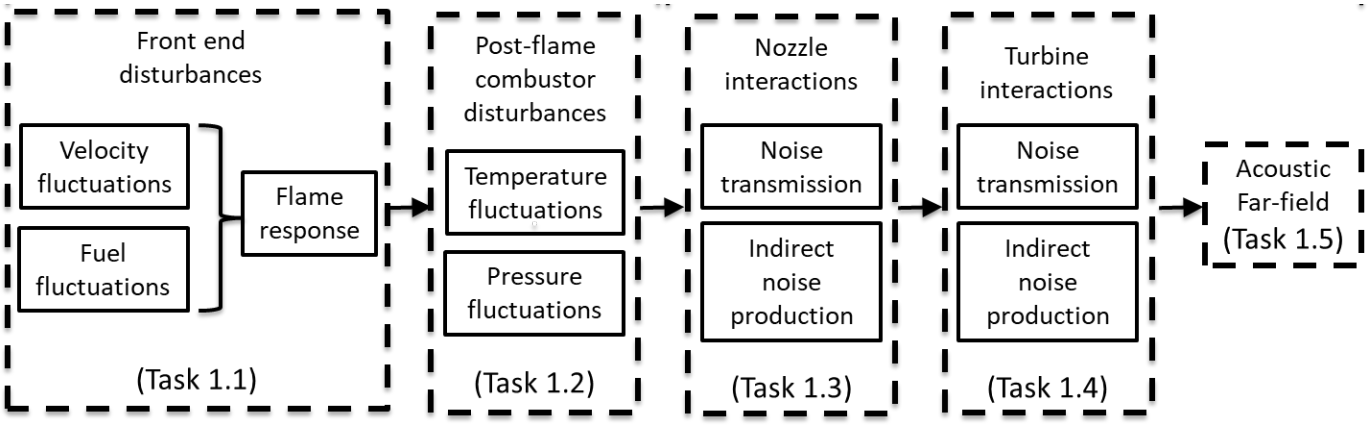


**Figure 1.** Physical processes and project tasks for noise generation.

The physics of noise generation begins with source disturbances upstream of the combustion zone, which involve unsteady dynamics in the flow and incoming fuel (spray), followed by the response of the combustion zone (flame) to these upstream disturbances. The fluctuations in the unsteady heat release led to the generation of pressure and entropy fluctuations. These fluctuations propagate further downstream in the combustor, interact with the nozzle and turbine, and eventually lead to far-field sound generation. Given the complex interplay of unsteady physics in the different parts of the engine, developing a ROM is challenging.

An important goal of this project is to generate high-quality reference data from both measurements and validated high-fidelity simulations, including measurements of the flow, spray, and flame unsteadiness in the head end of the combustor. Subsequently, the secondary combustion zone is characterized. The generation of entropy and pressure disturbances is then characterized through measurements of temperature and pressure fluctuations, followed by measurements of noise reflection and transmission through the turbine and nozzle section, and sound measurements in the far field. The measurements are accompanied by LES and finite-element simulations that are validated against the measurements. Collectively, these data are generated across a range of operating parameters and provide a source database for the modeling task.

The main goal of this project is to develop a robust design tool that can predict noise at operating points for which prior measurements or data are unavailable. To achieve this goal, two major tasks are necessary. First, ROM and frameworks must be developed for different aspects of the engine architecture: flow/spray models, flame response models, entropy generation models, entropy propagation models, nozzle interaction models, turbine interaction models, and far-field noise generation models. The ROM for each of these aspects involves simplifications and assumptions that are validated against the source database. The validation study and iterative improvement of model predictions serve as the second task to achieve this goal.

In this report, we summarize the efforts of both teams from October 2022 to September 2023. The efforts primarily include improvements to the GT rig to achieve a better match with RTRC experiments as well as RTRC rig campaigns with the Continuous Lower Energy, Emissions, and Noise (CLEEN) rig. In addition, ROM frameworks and simulations have been further advanced. A workflow has been established to transfer simulation data to ROM tasks, and multiple subtask

benchmarking targets have been identified. Finally, task input–output relationships among the various transfer functions have been identified, in the first step toward building the toolchain implemented in the design tool.

# Task 1 – Facility Development at GT

Georgia Institute of Technology

## Objective

The objective of this task was to make improvements and additional measurements with the RQL combustor designed in the previous year. The first portion of this year was dedicated to the manufacturing and assembly of new components. After the combustor was installed at the GT facility, diagnostic tools were installed to measure the flame and pressure dynamics. A test matrix was developed and used to enable comparison and validation of the GT and RTRC data, particularly at the overlapping points of the approach condition.

## Research Approach

In the previous years, we conducted an iterative cycle of tests, data analysis, and rig improvements. Last year, the rig was updated with a stronger liner frame, improved windows, and a more reliable igniter. This year, the rig was used to conduct another data campaign. Measurements focused on acoustics data, with companion high-speed chemiluminescence imaging. Test conditions focused on the baseline approach point that was established by Raytheon. A test matrix was established around this point, and was set up with perturbations to investigate different heat release ratios and flow rates for the head end vs. the quench zone. These perturbations were detailed to additionally match (or nearly match) some of the perturbations in the Raytheon test matrix. The test matrix also included an extra combustor inlet temperature perturbation with acoustics data only, to understand the sensitivity of tonal noise that can confound the interpretation of broadband noise. The RTRC test points have been redacted from this report, and only GT parameters are presented herein. Figure 2 shows the test matrix design.

| Chemiluminescence Data? | Notes | Test | Total Airflow Factor | Swirl / (Sw + Q) | Fuel % | P3 [psi] (upstream of swirler) | T3 [F] | Swirler Phi | Global phi | Quench/Main Split | Main Air [lb/s] | Quench Air [lb/s] | Window Air [lb/s] | Total Air [lb/s] | Primary Fuel [lb/hr] | Secondary Fuel [lb/hr] | Total Fuel [lb/hr] | FAR4 | Total Air Engine | FAR4 Eng |
|---|---|---|---|---|---|---|---|---|---|---|---|---|---|---|---|---|---|---|---|---|
| Yes | Z0. Shakedown (Approach point) | Z0 | | 29% | 100% | 118 | 752 | 1.487 | 0.37 | 2.50 | 0.207 | 0.517 | 0.103 | 0.827 | 22.6 | 52.7 | 75.2 | 0.025 | 1.034 | 0.020221 |
| Yes | **1. Low swirler flow, match global phi** | 1 | 100% | 26% | 100% | 118 | 752 | 1.662 | 0.37 | 2.91 | 0.185 | 0.539 | 0.103 | 0.827 | 22.6 | 52.7 | 75.2 | 0.025 | 1.034 | 0.020221 |
| Yes | **2. High swirler flow, match global phi** | 2 | 100% | 32% | 100% | 118 | 752 | 1.346 | 0.37 | 2.17 | 0.228 | 0.495 | 0.103 | 0.827 | 22.6 | 52.7 | 75.2 | 0.025 | 1.034 | 0.020221 |
| Yes | **3. Low swirler flow, match swirler phi** | 3 | 100% | 26% | 89% | 118 | 752 | 1.487 | 0.33 | 2.91 | 0.185 | 0.539 | 0.103 | 0.827 | 20.2 | 47.1 | 67.3 | 0.023 | 1.034 | 0.018093 |
| Yes | **4. High swirler flow, match swirler phi** | 4 | 100% | 32% | 110% | 118 | 752 | 1.487 | 0.41 | 2.17 | 0.228 | 0.495 | 0.103 | 0.827 | 24.9 | 58.2 | 83.1 | 0.028 | 1.034 | 0.022342 |
| Yes | **5. High FAR4.** Drop airflow a little to maintain P | 5 | 92% | 29% | 115% | 118 | 752 | 1.830 | 0.46 | 2.45 | 0.193 | 0.473 | 0.103 | 0.769 | 26.0 | 60.6 | 86.5 | 0.031 | 0.961 | 0.025004 |
| No | **6. Low T3.** Raise airflow a little to maintain P | 6 | 104% | 29% | 100% | 118 | 552 | 1.415 | 0.36 | 2.45 | 0.217 | 0.532 | 0.103 | 0.852 | 22.6 | 52.7 | 75.2 | 0.025 | 1.065 | 0.01962 |
| | | | | | | | | | | | | | | | | | | #DIV/0! | | |

**Figure 2.** Test matrix design for the 2023 test campaign.

| | Case numbers | Core air (g/s) | Quench air (g/s) | Fuel (g/s) | T3 (K) (± 5K) | P upstream of swirler (psi) | Notes |
|---|---|---|---|---|---|---|---|
| Match (Z0) | 001, 002 | 94 | 235 | 9.5 | 655 | 124 | |
| Low swirler flow, match global phi (Z1) | 003, 004 | 84 | 245 | 9.55 | 655 | 122 | |
| High swirler flow, match global phi (Z2) | 007, 008 | 104 | 225 | 9.37 | 655 | 114 | |
| Low swirler flow, match swirler phi (Z3) | 009, 010 | 84 | 245 | 8.52 | 655 | 119 | |
| High swirler flow, match swirler phi (Z4) | 005, 006 | 104 | 225 | 9.72 | 655 | 120 | |
| High FAR (Z5) | 011, 012 | 88 | 215 | 11 | 655 | 117 | |
| Near lean blowoff 1 | 013, 014 | 94 | 235 | 9.28 | 655 | 114 | |
| Near lean blowoff 2 | 015, 016 | 94 | 235 | 9.96* | 655 | 115 | Fuel flow rate measurement seems off a bit |
| Rich | 017, 018 | 94 | 235 | 12.65 | 655 | 127 | |

**Figure 3.** Achieved test conditions.

A series of test campaigns was conducted to work through the test matrix. The actual test points achieved are shown in Figure 3. Repeat tests were conducted for all cases, to assess repeatability. We first review the repeatability of the measurements. Figures 4-9 compare proper orthogonal decomposition through principal orthogonal dynamics (POD) analyses of the chemiluminescence data, showing the first six modes. The figures compare the mode shapes and temporal spectra, as well as the modal energies. The RTRC test points have been redacted from this report, and only GT parameters are presented herein. In general, these comparisons showed excellent repeatability when each test point was revisited.

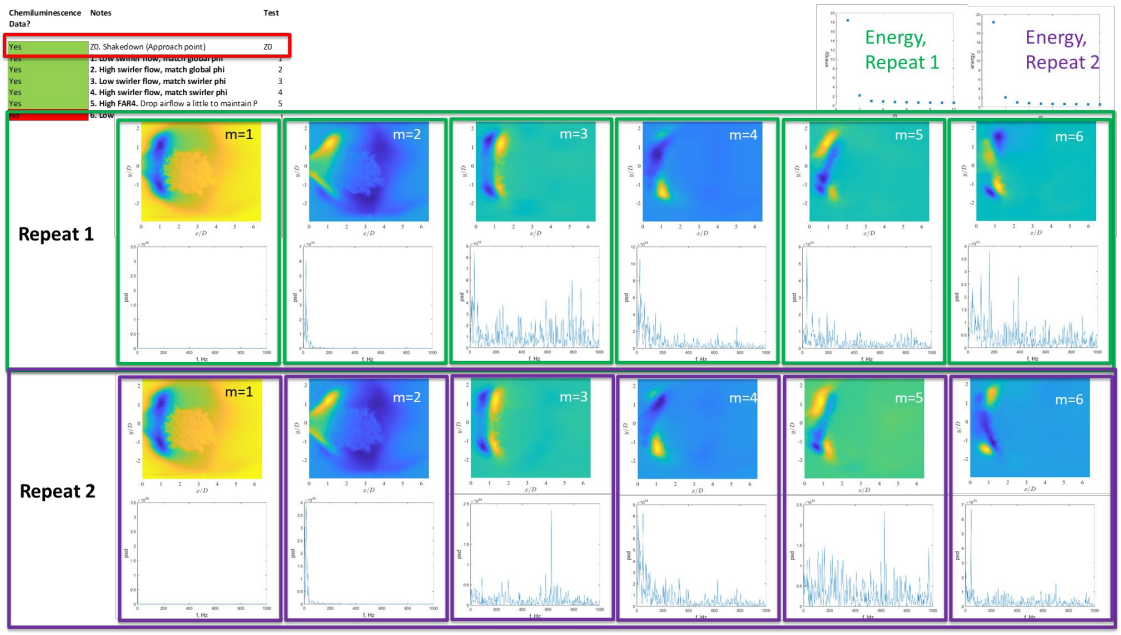


**Figure 4.** GT combustor repeatability study, baseline (Z0) approach condition.

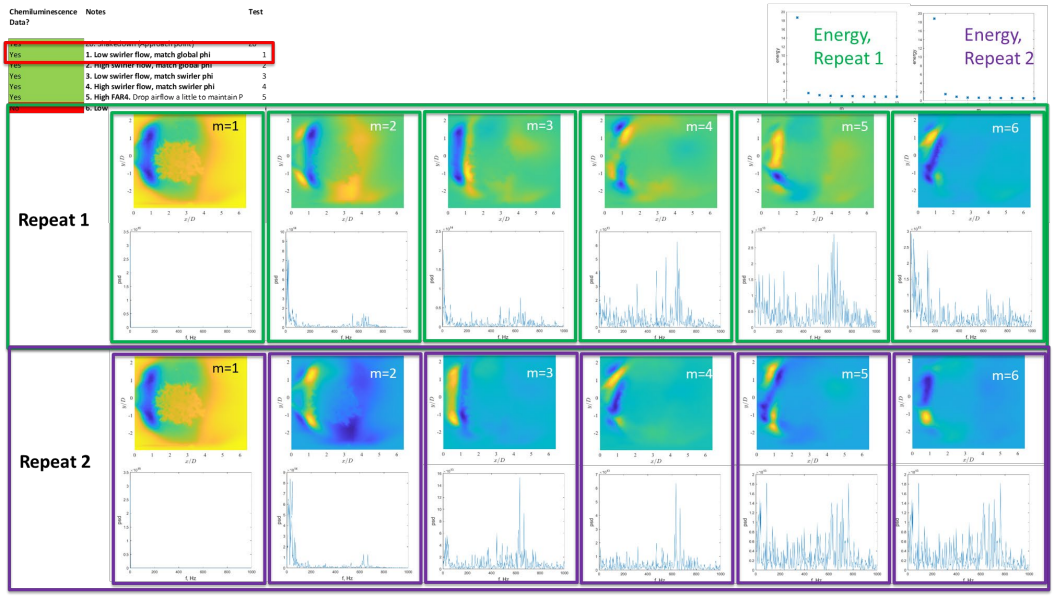


**Figure 5.** GT combustor repeatability study, condition 1.

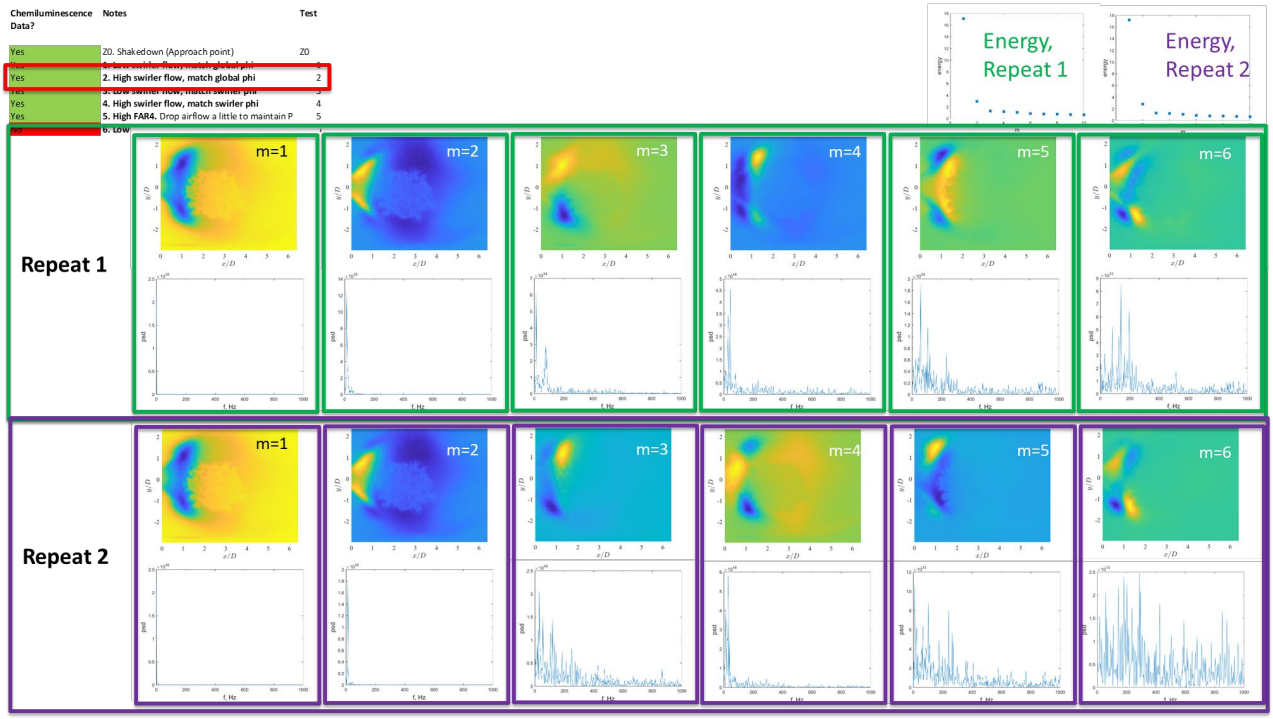


**Figure 6.** GT combustor repeatability study, condition 2.

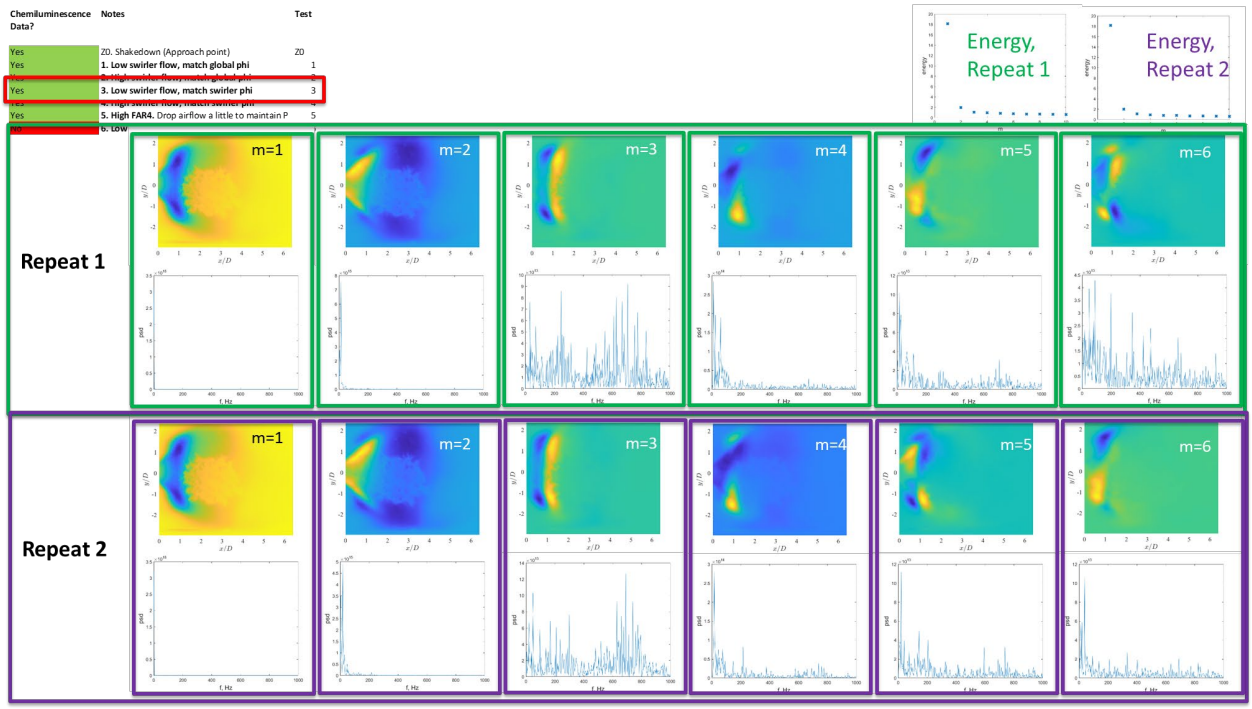


**Figure 7.** GT combustor repeatability study, condition 3.

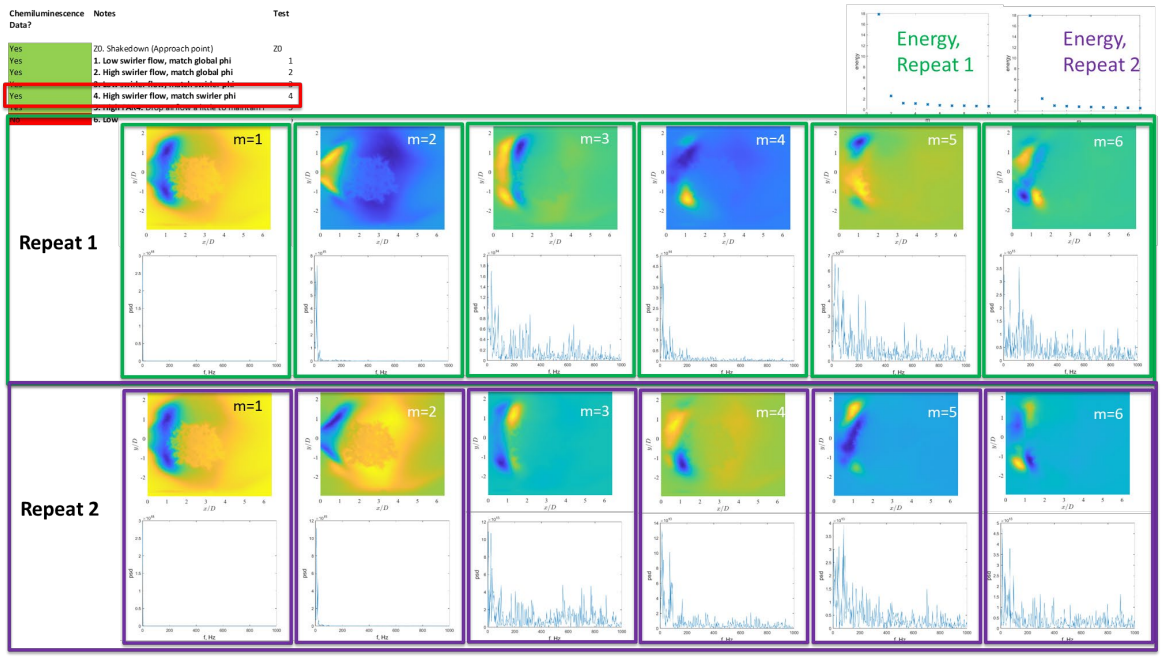


**Figure 8.** GT combustor repeatability study, condition 4.

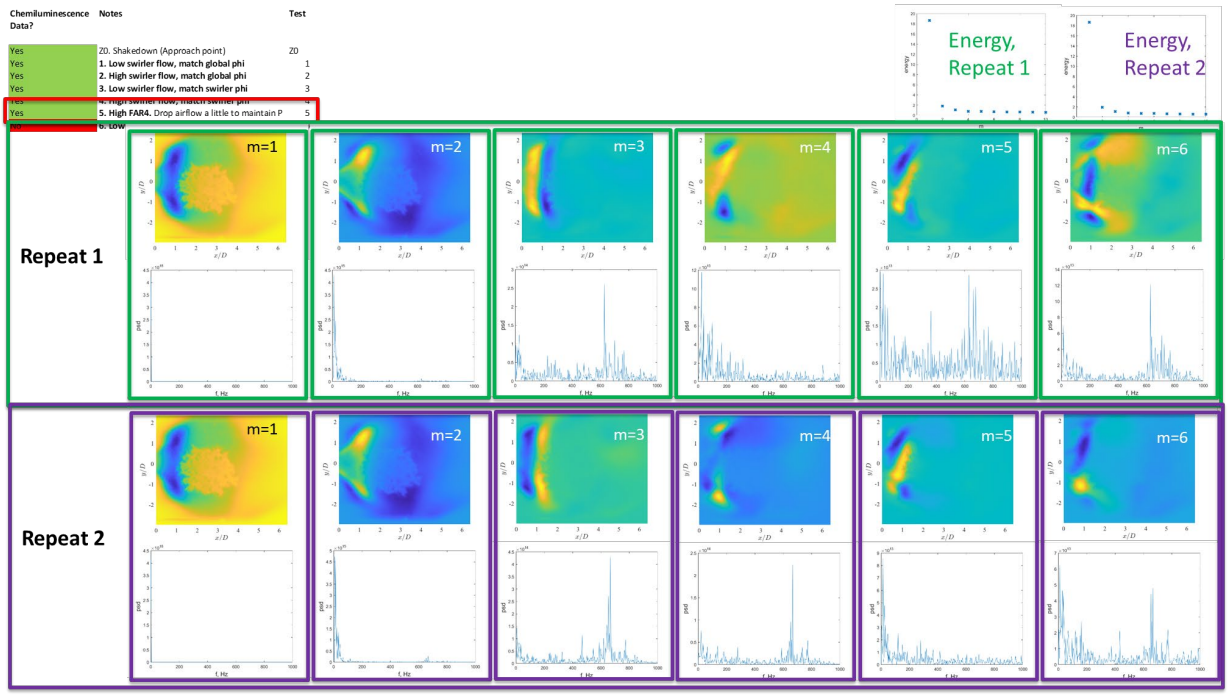


**Figure 9.** GT combustor repeatability study, condition 5.

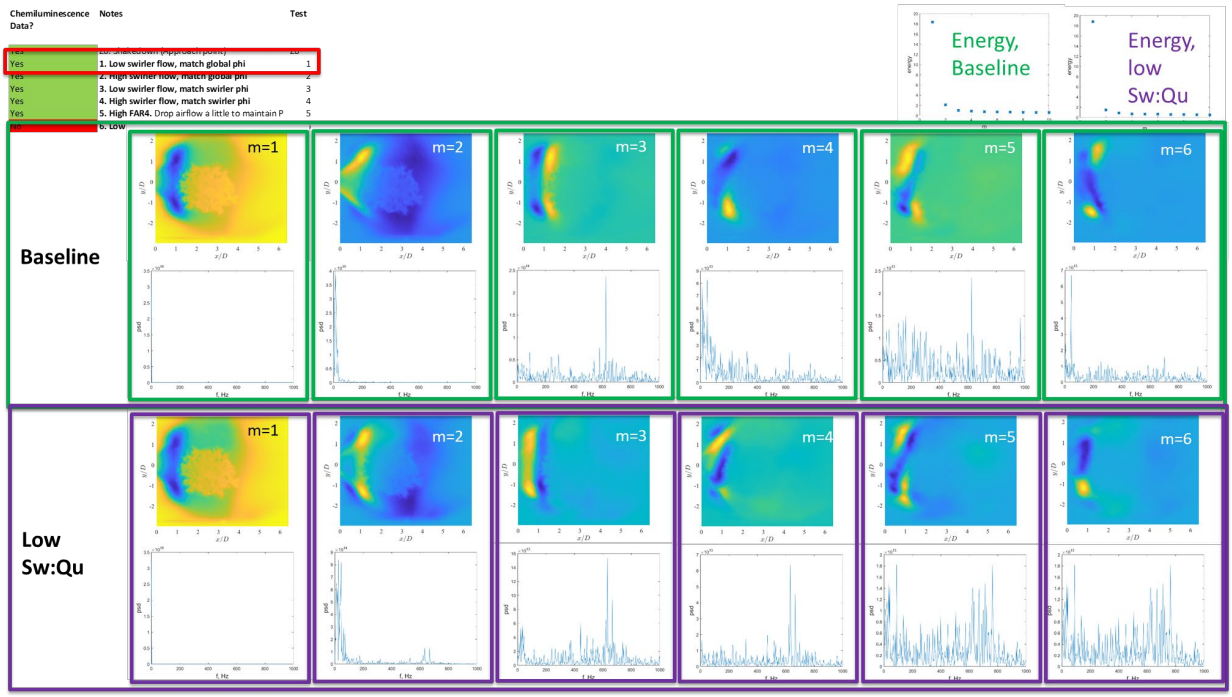


**Figure 10.** GT combustor study, first six chemiluminescence POD modes; comparison of condition 1 to the baseline (Z0) approach condition. Effect of reduced swirler-to-quench flow.

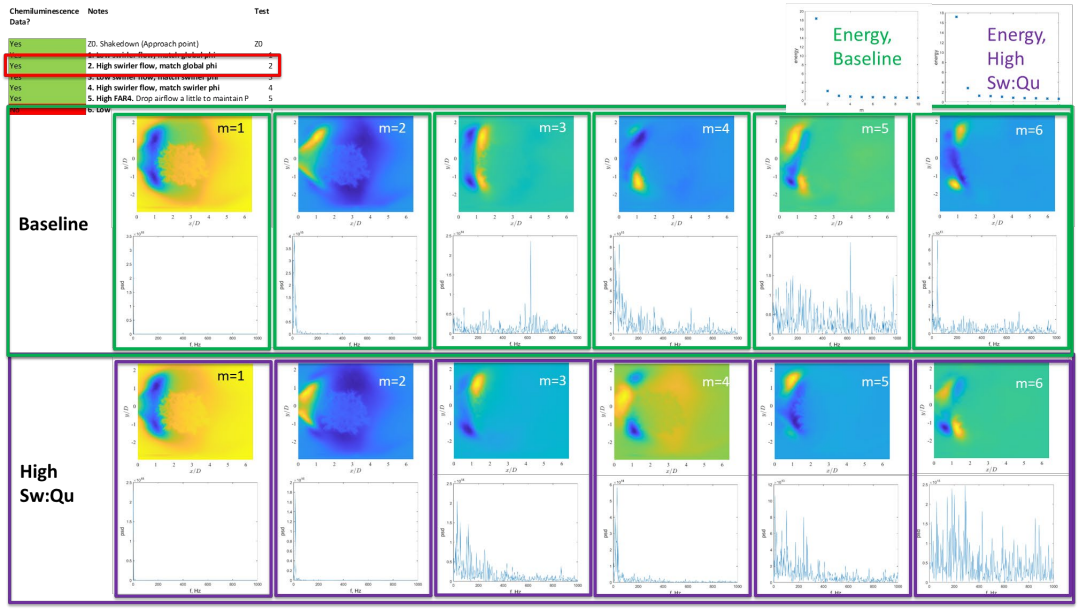


**Figure 11.** GT combustor study, first six chemiluminescence POD modes; comparison of condition 2 to the baseline (Z0) approach condition. Effect of increased swirler-to-quench flow.

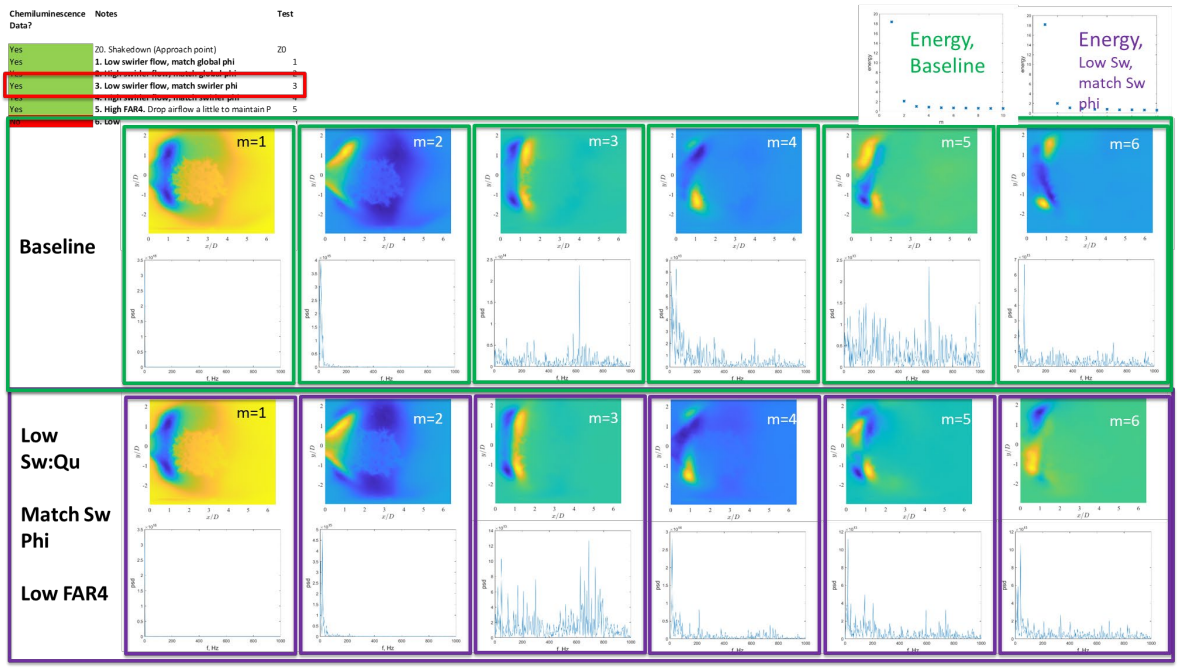


**Figure 12.** GT combustor study, first six chemiluminescence POD modes; comparison of condition 3 to the baseline (Z0) approach condition. Effect of reduced quench equivalence ratio (reduced quench zone heat release) relative to head-end heat release.

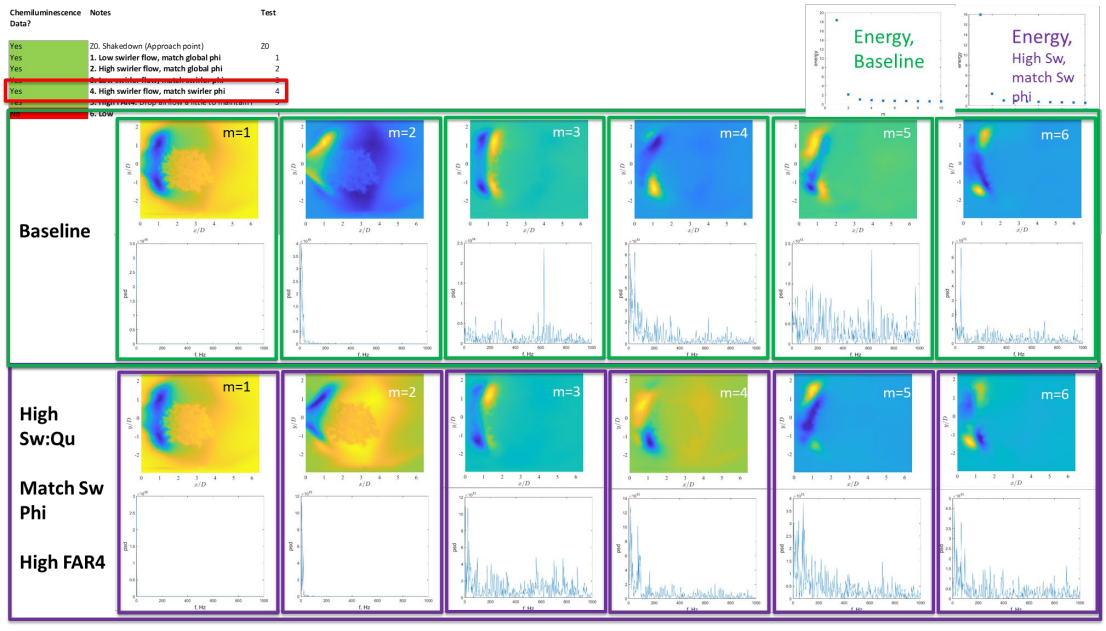


**Figure 13.** GT combustor study, first six chemiluminescence POD modes; comparison of condition 4 to the baseline (Z0) approach condition. Effect of increased quench equivalence ratio (increased quench zone heat release) relative to head-end heat release.

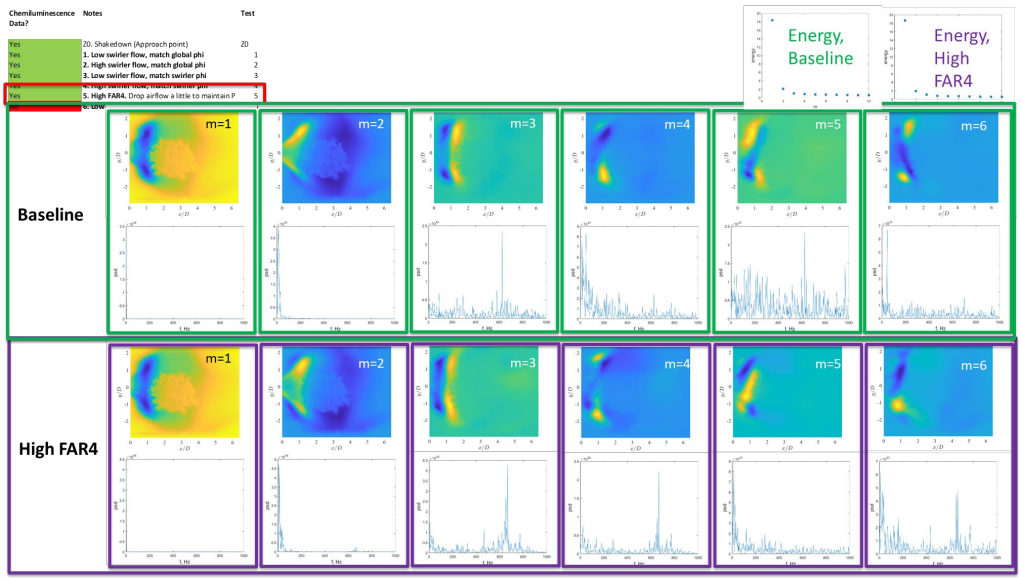


**Figure 14.** GT combustor study, first six chemiluminescence POD modes; comparison of condition 5 to the baseline (Z0) approach condition. Effect of increased overall heat release (increased FAR4, increased turbine inlet temperature).

Next, we review comparisons of the acoustic data from each case to the baseline (Z0) approach case. The most notable result is the sensitivity of tonal noise (~600 Hz) to these perturbations. Interestingly, these perturbations substantially manipulate the quench zone, and the chemiluminescence images of the head end are insensitive to these operating-condition perturbations. These observations suggest that this mid-range frequency (~600 Hz) noise is produced in the quench zone.

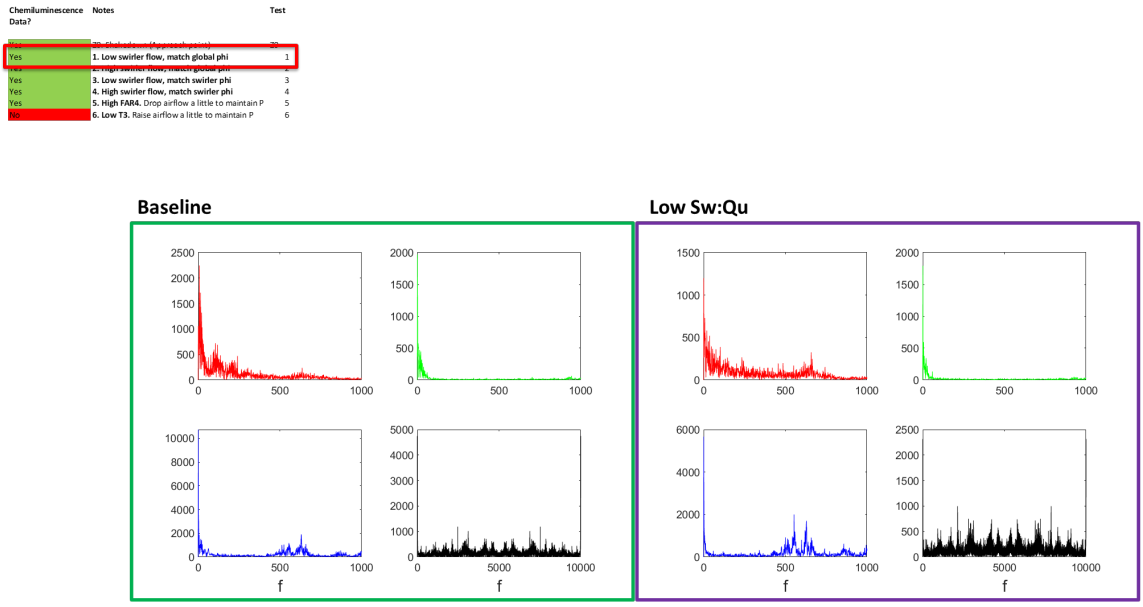


**Figure 15.** GT combustor study, acoustic spectra from the four ramp acoustic ports; comparison of condition 1 to the baseline (Z0) approach condition. Effect of reduced swirler-to-quench flow.

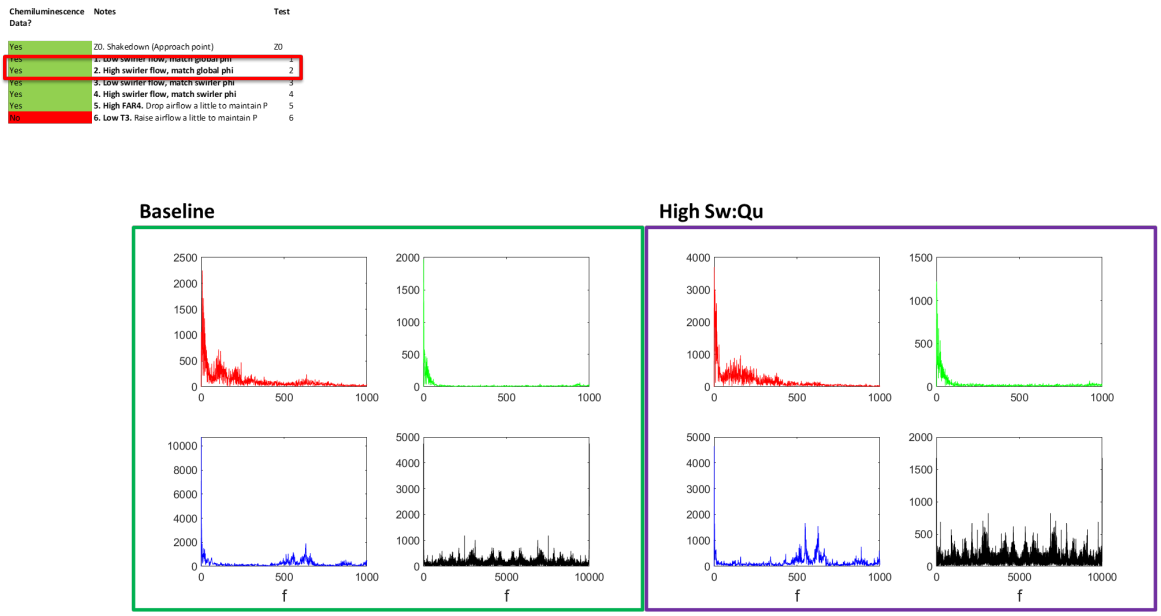


**Figure 16.** GT combustor study, acoustic spectra from the four ramp acoustic ports; comparison of condition 2 to the baseline (Z0) approach condition. Effect of increased swirler-to-quench flow.

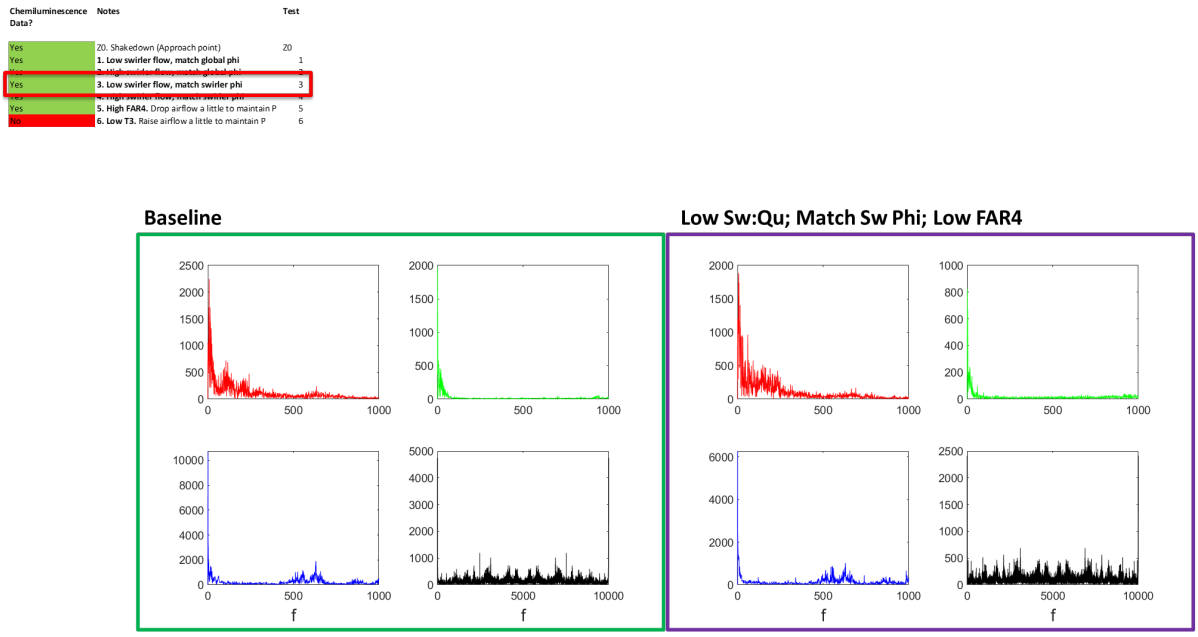


**Figure 17.** GT combustor study, acoustic spectra from the four ramp acoustic ports; comparison of condition 3 to the baseline (Z0) approach condition. Effect of reduced quench equivalence ratio (reduced quench zone heat release) relative to head-end heat release.

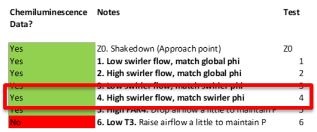

| Chemiluminescence Data? | Notes | Test |
|---|---|---|
| Yes | Z0. Shakedown (Approach point) | Z0 |
| Yes | **1. Low swirler flow, match global phi** | 1 |
| Yes | **2. High swirler flow, match global phi** | 2 |
| [illegible] | [illegible] | [illegible] |
| Yes | **4. High swirler flow, match swirler phi** | 4 |
| [illegible] | **5. High FAR4.** Drop airflow a little to maintain P | [illegible] |
| No | **6. Low T3.** Raise airflow a little to maintain P | 6 |

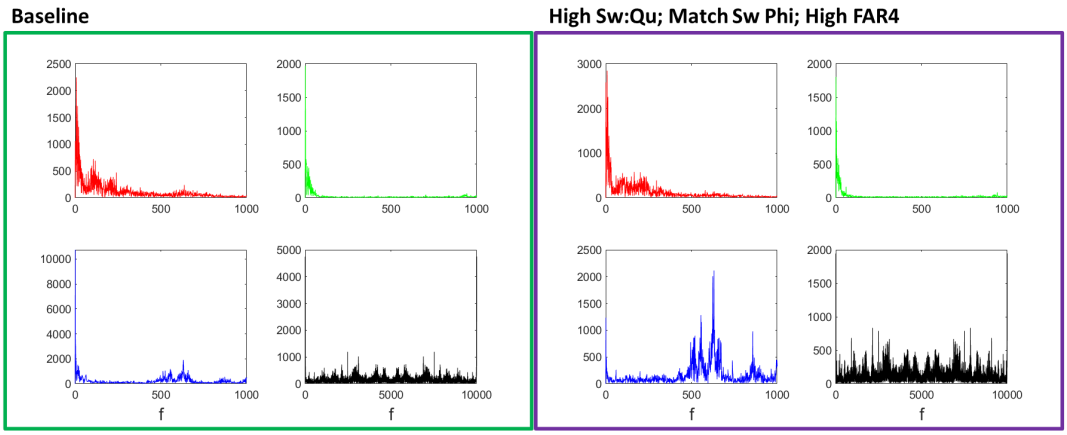


**Figure 18.** GT combustor study, acoustic spectra from the four ramp acoustic ports; comparison of condition 4 to the baseline (Z0) approach condition. Effect of increased quench equivalence ratio (increased quench zone heat release) relative to head-end heat release.

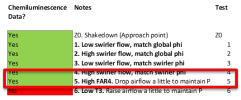

| Chemiluminescence Data? | Notes | Test |
|---|---|---|
| Yes | Z0. Shakedown (Approach point) | Z0 |
| Yes | **1. Low swirler flow, match global phi** | 1 |
| Yes | **2. High swirler flow, match global phi** | 2 |
| Yes | **3. Low swirler flow, match swirler phi** | 3 |
| [illegible] | **4. High swirler flow, match swirler phi** | [illegible] |
| Yes | **5. High FAR4.** Drop airflow a little to maintain P | 5 |
| [illegible] | **6. Low T3.** Raise airflow a little to maintain P | 6 |

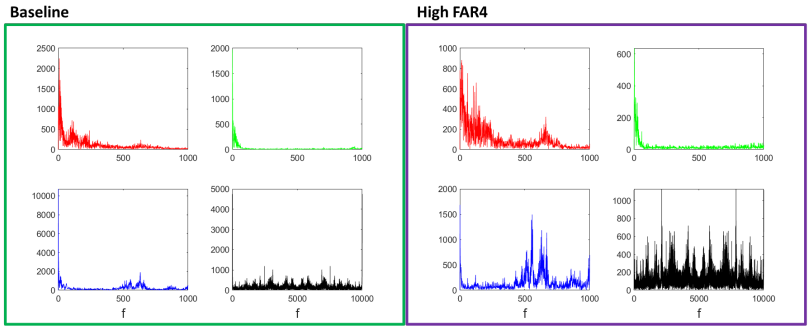


**Figure 19.** GT combustor study, acoustic spectra from the four ramp acoustic ports; comparison of condition 5 to the baseline (Z0) approach condition. Effect of increased overall heat release (increased FAR4, increased turbine inlet temperature).

We attempted to correlate the acoustic pressure signals with the heat release rate (HRR) data from the high-speed chemiluminescence. Correlations with the spectra of the HRR from the head-end zone with the acoustic data were poor, thereby suggesting coupled physics in the quench zone. During this analysis, the GT team realized that the analysis of HRR vs. acoustics coherence is a nuanced and requires further development for the differentiation of direct noise, indirect noise, narrowband sound, and background noise. A major pivot in this task has been the development of these methods and dissemination to the combustion community. These developments are further detailed in this report.

## Milestones

- The GT team has completely re-designed the combustor and its structural support/plumbing layout.
- The GT team has completed a test cell cleanout and procurement, manufacturing, and assembly of a new combustor.
- The GT team has shaken down the combustor, overcome all hurdles uncovered in the shakedown, and begun testing the new combustor.

## Major Accomplishments

The designed RQL combustor was manufactured and installed at the GT facility. The rig has been re-designed and rebuilt to enable higher-quality data, better durability, and improved matching to the RTRC rig.

## Publications

None.

## Outreach Efforts

None.

## Awards

None

## Student Involvement

- **Amalique Acuna (GT):** Graduate Student. Mr. Acuna works on and operates the experiment at GT. Mr. Acuna has graduated.
- **Shivam Patel (GT):** Graduate Student. Mr. Patel is funded on a NASA ULI contract, but he actively contributes to the maintenance, construction, and operation of the experiment at GT.
- **Sungyoung Ha (GT):** Graduate Student. Mr. Ha is the lead experimentalist on the GT rig.
- **Jananee (GT):** Graduate student. Jananee is responsible for the optical diagnostics on the GT rig.
- **Archit Bapat (GT)**: Graduate student. Mr. Bapat is funded as a teaching assistant. He is assisting with the optical diagnostics on the GT rig.

## Plans for Next Period

The GT rig team plans to continue the measurement campaign during the next period, with the inclusion of additional diagnostic methods throughout the process.

# Task 2 – Simulations of the GT Experiment

Georgia Institute of Technology

## Objectives

The first objective of this task is to validate and justify the compressible reactive LES approach for modeling the GT experimental rig at match point. In addition to the match point, the second objective is to evaluate the LES's ability to capture trends across different conditions. The last objective is to collect time-dependent three-dimensional (3D) snapshots of conservative variables from the LES for GT experimental conditions and transfer those findings to the RTRC and GT modeling teams. Sample post-processing scripts for computing additional variables from the 3D snapshots will also be provided.

## Research Approach

### Solver details

A fully compressible Eulerian finite-volume formulation for the gas phase and a Lagrangian formulation for the liquid phase are used in this study. An eddy-viscosity approach with a one-equation subgrid kinetic energy ($k_{sgs}$) model is used for the closure of gas-phase subgrid-scale fluxes. Because regions in which turbulence is not well established may exist in the plenum or outflow duct, the $k_{sgs}$-equation coefficients are set to constant values rather than being dynamically computed. Subgrid dispersion for spray particles is modeled with a stochastic separated flow model. Modeling of dense spray,

corresponding compressible volume blockage effects, and breakup are also available, as we have previously shown, but these conditions are not considered herein; instead, a dilute injection of spray is considered. A well-established secondary breakup model based on Kelvin–Helmholtz instability is used, and its effect is evaluated in this study.

The combustion is modeled via a finite-rate kinetics approach, by using a two-step, six-species mechanism for kerosene. Subgrid closure for turbulent combustion is provided by a simplified partially stirred reactor model, wherein the mixing time ($\tau_m$) is computed locally by using $k_{sgs}$, and the chemical time ($\tau_c$) is precomputed for the operating conditions from laminar premixed flame solutions under stoichiometric conditions. Further details about our modeling approach can be found in our recent works and are not repeated herein, for brevity.

The equations are solved at GT with the in-house solver LESLIE. LESLIE is a well-established multi-block, structured, fully compressible finite-volume solver. A hybrid second-order central and third-order upwind method is used for the gas-phase evolution. A fourth-order Runge–Kutta solver is used for solving the Lagrangian equations. For computational efficiency, instead of tracking individual Lagrangian particles, the particles are grouped together in "parcels," which are tracked in a Lagrangian manner. A particle-per-parcel value of 8 is used in this work, which has been shown to provide a good balance between accuracy and efficiency for gas-turbine combustor LES.

The current version of the GT compressible solver contains three parts: CFDPreProc, LESLIE, and CFDPostProc. CFDPreProc is a pre-processor that can perform functions such as creating a grid and setting boundary conditions. LESLIE is a core compressible solver that conducts multi-phase reactive LES. The latest LESLIE code (improved during the Year 2 efforts) outputs 3D snapshots of conservative variables that are directly solved for in our compressible framework, including the density, momentum, total energy, and partial densities. Primitive variables remain required for the computation of noise-related quantities; therefore, CFDPostProc CFD post-processing software is used to read the conservative variable-based 3D snapshots and compute additional primitive quantities. This code is provided to the RTRC and GT ROM teams along with the 3D snapshots. The conservative variables form an exclusive and exhaustive set of variables; therefore, all other quantities can be computed from this set.

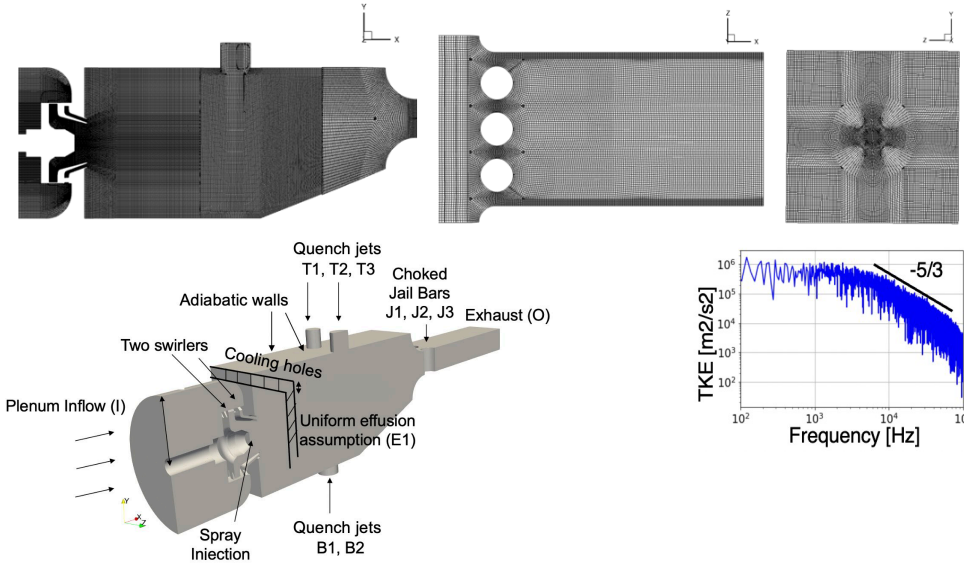


**Figure 20.** Computational domain for LES. Top: schematics for the multi-block structured grid (main combustor at the center *x*–*y* plane, region behind the jail bars at the center *x*–*z* plane, and shear-layer region at the *y*–*z* plane located at one-third of the axial length of the main combustor). Bottom left: entire computational domain, with key features and corresponding boundary conditions. Bottom right: turbulent kinetic energy (TKE) spectra in the shear layer, showing the inertial subrange captured by LES.

**Computational configuration**

The computational configuration is shown in Figure 20. The flow from the inlet plenum enters the combustion chamber via two concentric swirlers (one axial and one radial). After the reaction zone, three quench jets on the top, and two on the bottom, are available to reduce the temperature. In addition, multiple small cooling holes are present on the dome plate to decrease the wall temperature. The flow exits the outflow duct through jail bars, which act as a nozzle that chokes the flow.

The boundary conditions are consistent with the findings from GT experiments. All gas-phase inlet boundary conditions are constant mass flow inlets, on the basis of experimental data inputs. The inflow boundary condition (ahead of the inlet plenum [I] and dilution holes [T1, T2, T3, B1, and B2]) is modeled with a characteristic Navier–Stokes boundary condition. The mass flow rate for the main inflow (I) is set as 93.89 g/s (according to GT rig inputs). The total mass flow rates through the top (T1, T2, and T3) or bottom (B1 and B2) dilution holes are 117.03 g/s. The incoming air is at 673.3 K. The flow through the jail bar (J1, J2, and J3) chokes and pressurizes the combustor to the nominal target. With choking, the outflow (O) is supersonic at the domain outlet. The outflow following the choked nozzle is modeled with a sponge boundary condition, but no waves are expected to travel upstream into the combustor chamber from this region, because the nozzle is choked. The quench holes are not resolved; therefore, they are modeled with a porous boundary condition. The mass flow rate specified through the quench holes is 46.72 g/s.

The Lagrangian spray droplets are injected in a stochastic manner with two concentric injectors. The mass flow rate is 2.4 g/s through the primary injector and 6.89 g/s through the secondary injector. In the absence of any experimental measurements for this injector, a log-normal size distribution with Sauter mean diameter of 30 μm and 55 μm is injected in the absence or presence of secondary breakup modeling, respectively. These modeling choices are similar to previous gas-turbine LES (Patel & Menon, CF, 2008, Panchal & Menon, CF, 2022). The primary injector is modeled as a solid cone injector with a 60° angle; the secondary injector surrounds the primary injector and is modeled as a hollow cone injector with 90° and 120° inner and outer angles, respectively. The injection temperature of the liquid fuel is 330 °K, and the velocities are set to 25 m/s. This dilute injection occurs 1 mm downstream of the actual injector plate. This injection procedure is empirical but could be improved in the future, on the basis of experimental insights.

The multi-block structured grid has 6.8 million cells and 4,571 blocks, and grid clustering is applied to the near region of the shear flow from the swirler and jail bars. For handling geometrical complexities, six multi-block structure grids are generated with hanging nodes, which are stitched together via an interpolation technique of the same order as the numerical scheme used. Shear layers are resolved with 10–15 points across, and the swirlers have 10 or more points along their span, in agreement with previous LES. Small quench holes on the dome plate are not resolved, but a pre-specified mass flow rate is injected through these holes with a porous boundary condition, as discussed below. For demonstrating the sufficiency of the LES grid, the turbulent kinetic energy is computed at a representative point in the shear layer, as shown in Figure 20, to capture the inertial subrange. This result has been confirmed at other points within the combustor, e.g., cooling jets, swirling shear layer, etc., but these data are not shown herein, for brevity.

The LES solver is parallelized, and the simulations are run on 1,440 cores. The flow-through time of the combustor is estimated to be 8 ms, according to the entire length of the computational domain and a reference bulk velocity of 30 m/s. Initial transients are neglected for at least the two flow-through times or until the chamber pressure and volume-integrated HRR stabilize. The statistics are then collected over at least 10 additional flow-through times. A simulation for a single flow-through time uses 51,840 CPU hours on GT's supercomputing cluster (Partnership for an Advanced Computing Environment-Phoenix) with Intel Ivy-bridge i7 processors.

**Operating conditions**

After updating the CFD geometry to match the GT experimental rig during year 2, we considered three operating conditions in year 3, all with the same rig. The first simulation, "baseline," matches the "Z0" GT and RTRC baseline operating conditions and maintains chamber pressure at a target of 0.87 MPa. To evaluate the LES's ability to predict trends in operating conditions and to generate more data for ROM development, we consider two additional conditions. The next condition uses a higher fuel–air ratio (FAR), in which the fuel mass flow rate is increased by 15%, and the total air mass flow rate is reduced by 8% to maintain the same chamber pressure. This condition coincides with one of the high-FAR conditions in the experimental campaign. The third test is a numerical experiment considering a modified quench-jet configuration, wherein T1 and T3 are shut off, and all air that would come from the quench jets through the top instead comes through the center jet T2. These details are summarized in Table 1. All simulations were run with the same solver and model choices.

**Table 1.** List of simulated operating conditions.

| | Fuel mass flow rate | Air mass flow rate | Quench configuration |
|---|---|---|---|
| Match-point/baseline | 9.29 g/s | 374.67 g/s | T1, T2, T3, B1, B2 |
| High-FAR | 10.68 g/s | 344.69 g/s | T1, T2, T3, B1, B2 |
| Quench-1 | 9.29 g/s | 374.67 g/s | T2, B1, B2 |

**Validation**

For validation and justification of the LES approach, we compare the simulation results at baseline conditions against GT experiments, as shown in Figure 21(b). The chemiluminescence data from the GT experiments is compared against the numerical time-averaged line-of-sight HRR predictions (in the absence of CH* or OH* from simulations), and show a reasonable match in terms of the flame structure.

Next, to evaluate noise predictions, pressure spectra are computed at several locations within the combustor and are compared against experiments, as shown in Figure 21(c). The probe locations follow both the GT and RTRC experimental rigs; one probe is on the bulkhead, and the remaining four are on the bottom ramp of the combustor before the jail bars, as shown in Figure 21(a). Near the experimental values (250 Hz and 700 Hz), the pressure power spectral density (PSD) from LES shows peaks at 300 Hz and 750 Hz. The sharp decrease in the PSD after 1000 Hz is also present in both rigs, although the GT experiments show a much sharper decline. To reduce the noise from the frequency data, Welch averaging with a sampling frequency of 36 Hz and 50% overlap is used over the entire 166 ms of LES data. As discussed further below, signal sizes longer than 100 Hz appear to be sufficient for LES signal processing in the range of 100–5000 Hz. The same processing methods are also used for the experimental data, but the total signal length is much longer (several seconds).

**Sensitivity to modeling and processing choices**

Year 2 simulations did not use a secondary breakup model, and their effects had not yet been evaluated. The effect of secondary breakup modeling and LES post-processing methods on flame and noise predictions have now been evaluated. As noted earlier, in the absence of any data for spray atomization and injection, an empirical injection is used. Simulations without a secondary breakup model inject droplets with a Sauter mean diameter of 30-μmdroplets, whereas simulations with a wave breakup model based on Kelvin–Helmholtz instability (Reitz, 1989) inject 55-μm droplets and allow them to break into smaller droplets through a physics-based approach on their own.

The LES results with and without breakup modeling at the baseline operating condition are compared in Figure 22. In the absence of secondary breakup modeling, the larger droplets require a longer time to evaporate, thus resulting in a less-than ideal HRR, as shown in Figure 22(b). The flame structure is also affected, as shown in Figure 22(a), and the flame structure predicted with secondary breakup modeling is more compact and closer to the experimental measurements in Figure 21(b). The overall flame and flow structures remain qualitatively similar with or without the secondary breakup model; however, the pressure spectra show significant sensitivity. The 750-Hz frequency, which is also prominent in the experiments, is largely missing from the LES predictions without the secondary breakup model. We hypothesized that the changes in the vaporization rate and the HRR due to the secondary breakup modeling might affect the dynamics and thus the pressure signature. Because using a physics-based secondary breakup model is physically a more correct approach, and the results also better match the experimental findings, all other simulations in this work use this default option.

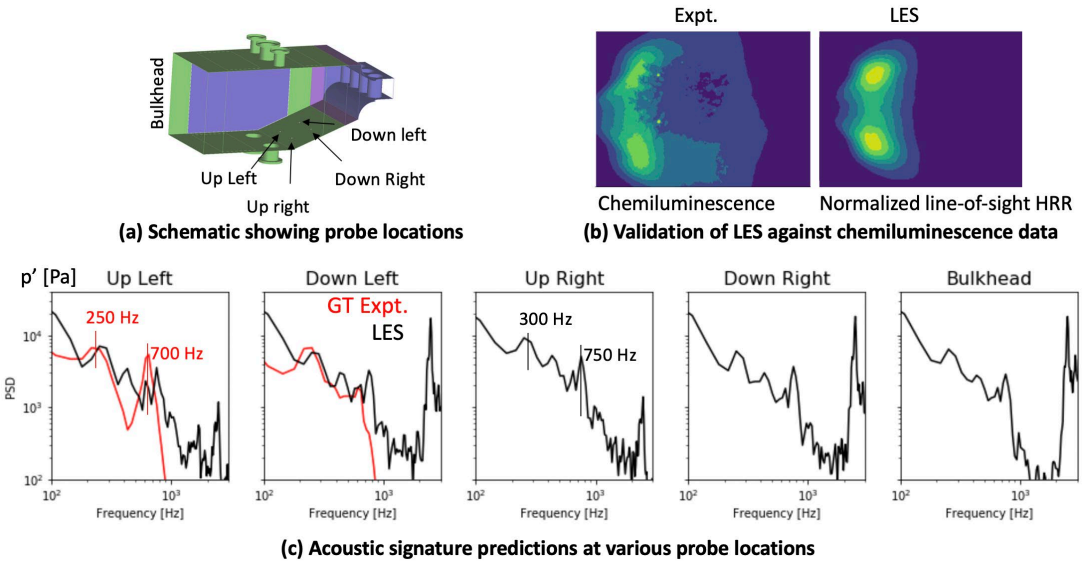


**Figure 21.** Validation of LES results under baseline conditions against GT experiments. (a) Schematic showing probe locations where acoustic data are collected. (b) Comparison of CH* chemiluminescence data against normalized time-averaged line-of-sight HRR data from LES. (c) Acoustic signature predictions from LES at five probe locations, and comparison against available data from GT experiments. LES results are over a 166-ms time window.

Next, to evaluate the effects of various LES post-processing options on the computed spectra, we conducted several tests on the baseline dataset. Several key conclusions are presented, but the corresponding results are not shown herein for brevity.

- Signal lengths of 50, 100, and 150 ms collected from LES were evaluated. We concluded that 100 ms is sufficiently long to satisfactorily capture frequencies between 100 and 5000 Hz.
- A sampling frequency of $10^4$ Hz is sufficient for predictions up to 1000 Hz. Higher frequencies may require a faster sampling rate. The current LES collects 3D snapshots at $10^4$ Hz and probe data at $10^6$ Hz.
- Local averaging near the probe location does not significantly affect spectra computed with Welch averaging.

**Flow and flame structure**

The LES can capture 3D unsteady large-scale flow, flame, and spray structures. Representative contours at an instant on *z*- and *y*-center slices are shown in Figure 23 for the baseline case. Furthermore, time-accurate LES results are averaged over eight flow-through times. The corresponding mean axial velocity and mean temperature are shown in Figure 24 on the *z*-center slice for both the baseline and quench-1 conditions. The instantaneous flow shows resolved large-scale turbulence within the combustor and also indicates that the flow remains choked at the jail bar nozzle at all times, thus maintaining the pressure. The flow converts from subsonic to supersonic at this point, and the supersonic flow after the nozzle shows a complex shock structure.

As a result of the swirl, a low-pressure zone is created in the center, and a vortex breakdown bubble (VBB) (also known as a central toroidal recirculation zone) is formed. This behavior has been observed for many other gas-turbine combustors and is a key feature of swirling flows. This combustor has two swirlers, but the observed VBB features remain qualitatively similar to those in past studies with a single swirler. Correspondingly, a negative velocity is observed in the center, as shown by the instantaneous axial velocity contours on the *z*-center slice in Figure 23(a) and time-averaged contours in Figure 24(a, b). The swirling shear layers are highly turbulent and can provide a zone for vaporization and flame stabilization. Because of the swirling jets, corner recirculation zones are also observed. The instantaneous velocity contours show the effects of the cooling jets near the corners, but these jets dissipate quickly after injection. The quench jets significantly affect the overall flow field by disrupting the continuation of the VBB, at least in the *z*-center slice shown here.

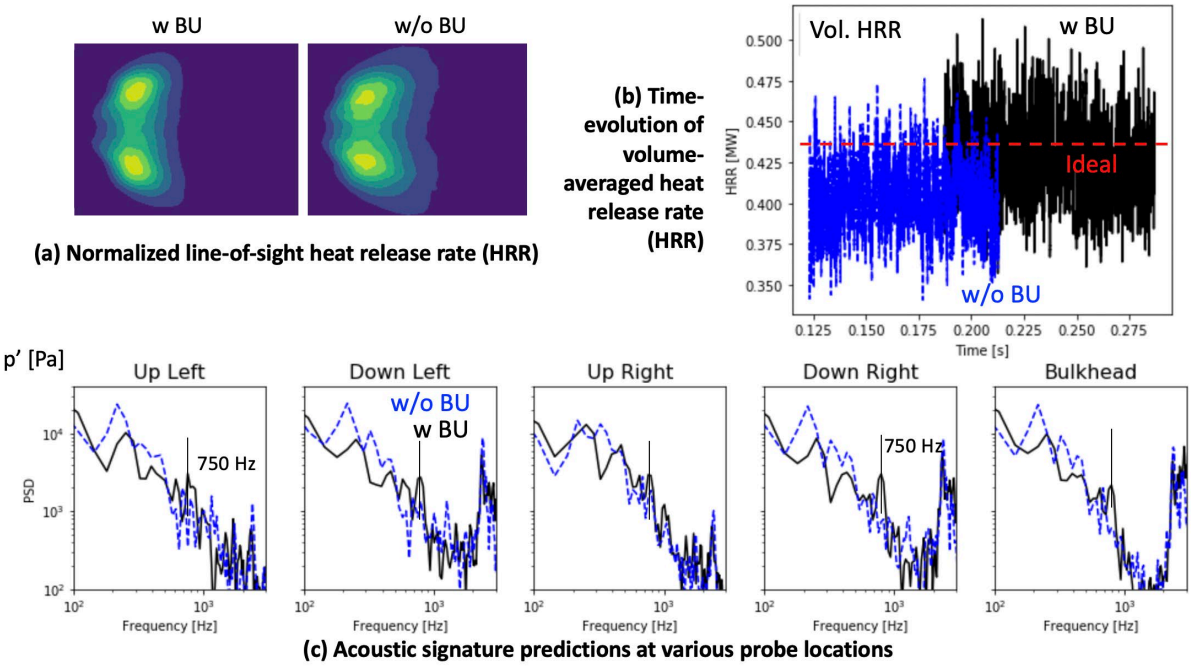


**Figure 22.** Comparison of LES results with and without secondary breakup modeling in terms of (a) normalized time-averaged line-of-sight HRR data, (b) time-evolution of volume-averaged HRR (with horizontal dashed line showing the ideal HRR, assuming 100% burning), and (c) acoustic signatures at various probe locations. Validation of LES results at baseline conditions against GT experiments. Results over a 100-ms time window are shown to enable one-to-one comparison.

The circulation zone of the VBB remains hot and is filled with combustion products produced by burning. Because of the high temperature, spray vaporization occurs in the surrounding regions. Fuel burning occurs in the shear layers, and the effects of large-scale turbulence on the burning are also apparent (not shown). The quench jets mix with the products, and highly turbulent mixing is observed.

The flow and flame structures are similar for baseline and high-FAR conditions, and their comparison is not shown herein, for brevity. However, because of the changed quench jet configuration, the quench-1 configuration shows a significant modification in the flow field, particularly after the entrance of the quench jet. Because of the increased mass-flow rate through T2, the jet can penetrate almost all way toward the bottom of the combustor, as shown in Figure 24(d). The axial flow adjusts to go from around it (not visible in the *z*-normal plane), and the jet penetration into the combustor increases by almost 80%. Although the volume-integrated HRR increases for the high-FAR case, as expected, quench-1 does not show a noticeable change in global quantities, although the flow structure is different.

**Dynamics**

Various quantities, i.e., chamber pressure, volume-integrated HRR, volume-integrated evaporation rate, and mass flow rates through various planes, are continuously monitored during the simulation. To obtain a global measure, the HRR and evaporation rate are also integrated over the entire volume of the combustor, and their time sequence is collected. Their oscillations can contribute to noise generation. In addition, as briefly described above, pressure at various probe locations within the combustor is collected, and Welch averaging is used to compute the PSD.

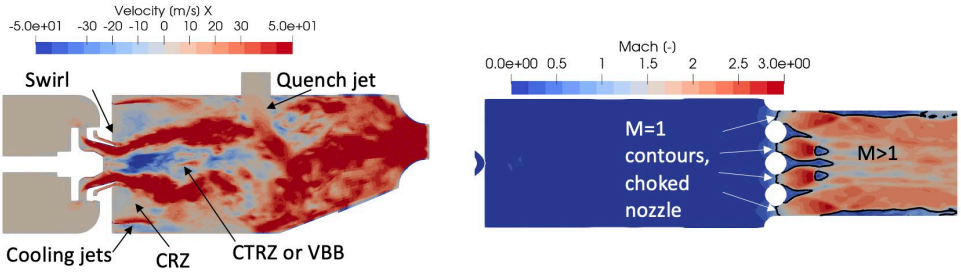


**(a) Axial velocity [m/s] on z-slice** **(b) Mach number on y-slice**

**Figure 23.** Instantaneous axial velocity and Mach number predicted from LES, shown on the center *z* slice under the baseline operating condition. CRZ: corner recirculation zone; CTRZ: central toroidal recirculation zone; VBB: vortex breakdown bubble.

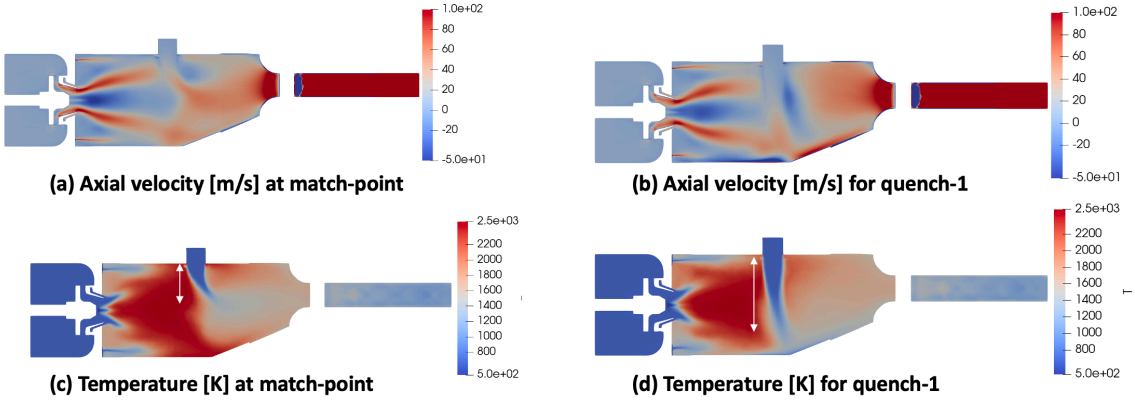


**(a) Axial velocity [m/s] at match-point** **(b) Axial velocity [m/s] for quench-1**

**(c) Temperature [K] at match-point** **(d) Temperature [K] for quench-1**

**Figure 24.** Time-averaged axial velocity (a,b) and temperature (c,d) on the center *z* slice, predicted from LES at baseline (a,c) and quench-1 (b,d) conditions. The white arrow shows the extent of T2 jet penetration into the domain. Time averaging is over an 80-ms time window to allow for one-to-one comparison.

The results for the baseline configuration (Figure 21) show peaks at 300, 750, 2400, and 4800 Hz. To understand the significance of these findings, we conducted further analyses. Figure 25 shows magnitude and phase of PSD at $f$ = 2400 Hz and $f$ = 4800 Hz, plotted on the top wall along the axial direction. These results show the magnitude decreasing and the phase changing sign at nodes, whereas the reverse occurs at antinodes. Furthermore, for this combustor, $f_0 = c/2L$ is estimated to be approximately 1300 Hz, where $L$ is the length between the dump plane and the nozzle, and $c$ is the speed of sound in non-reactive conditions. These results show a clear presence of a longitudinal acoustic mode between the dump plane and the jail bar nozzle at 2400 Hz and its higher-order harmonic at 4800 Hz.

These findings explain the higher frequencies; however, frequencies lower than 1000 Hz, which are usually the focus for broadband noise, remained poorly understood. Consequently, we conducted a POD analysis of line-of-sight HRR fields. Key results are shown in Figure 26. The findings indicated that the most energetic mode for the HRR is a monopole, showing a 700-Hz frequency. The next set of higher-order modes have lower intensity, but the 700-Hz peak is associated with longitudinal and transverse dipole modes in the HRR. Modes of an even higher order (i.e., quadrupole, etc.) do not show any presence of this frequency. These results suggest a coupling between the HRR and pressure at 700 Hz (direct or indirect), but the underlying mechanism remains unclear and requires further evaluation.

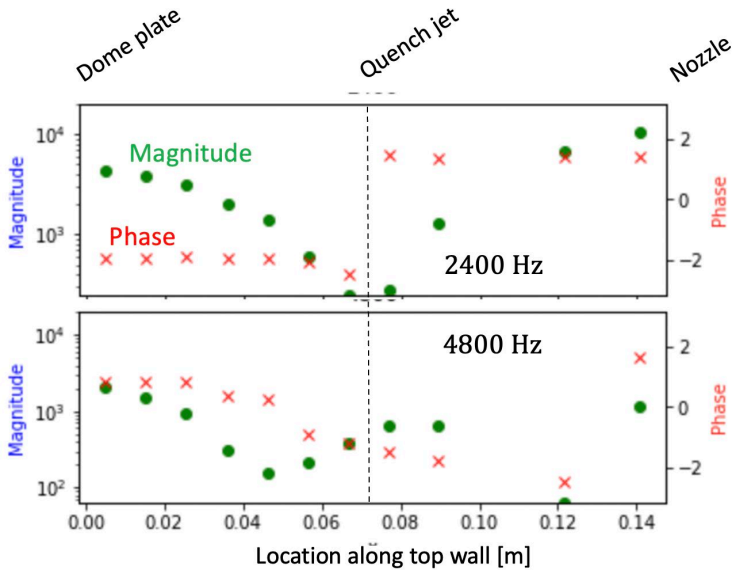


**Figure 25.** Magnitude and phase of pressure fluctuations plotted along the combustor top wall at $f$ = 2400 and 4800 Hz. Results are over a 100-ms time window.

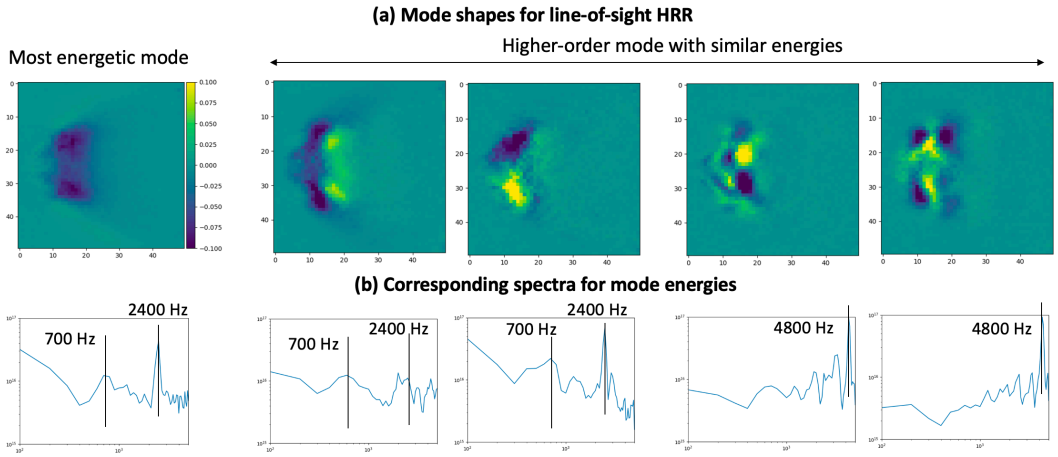


**Figure 26.** Modes of line-of-sight averaged HRR, computed with POD. The mode shapes are shown in (a), and the corresponding energies in the frequency space are shown in (b).

Having gained some understanding of the flame/flow structure and dynamical modes predicted within this combustor, we next compared the dynamics under baseline, high-FAR, and quench-1 conditions, as shown in Figure 27. Spectra of volume-integrated HRR are also compared. High FAR shows a significant increase in the content for $f$ < 700 Hz, with almost no change for $f$ >1000 Hz. This finding may suggest that the increase HRR plays a role and is qualitatively similar to the experimental observations, although a one-to-one comparison remains to be conducted. In contrast, for quench-1, in which the HRR is not affected, but the cooling mechanism is affected, an increase in content for $f$ >1000 Hz (at least at certain locations) is observed without any significant change for $f$ < 1000 Hz. Understanding the mechanisms underlying these changes requires further analyses of the results, as is currently underway.

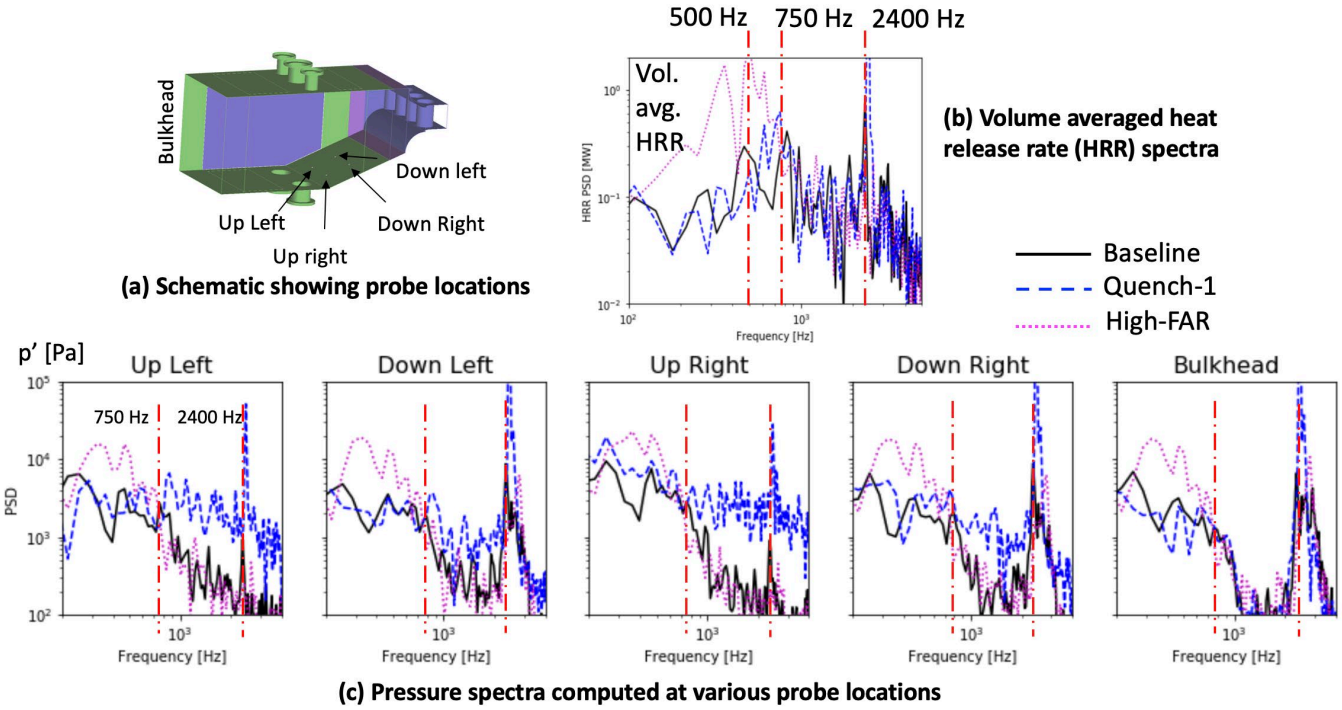


**Figure 27.** Comparison of HRR (b) and pressure spectra (c) among operating conditions: baseline, quench-1, and high FAR from LES computation. Panel (a) shows the various probe locations for pressure. All spectra are computed over an 80-ms time window to allow for one-to-one comparison.

**Data output and transfer**

The simulations output 3D snapshots of conservative variables, as noted above. The output frequency of these outputs is $10^4$ Hz, and at least 1,000 such snapshots are output for each case over the span of a 100-ms simulation time. The snapshots are collected only after the initial transients for the first two flow-through times have been neglected. A single 3D snapshot is ~1 GB in size. The CFDPostProc software and sample post-processing scripts can (a) compute primitive quantities, such as pressure, temperature, density, and reaction rates; (b) compute derivatives; (c) compute time-averaged quantities; and (d) interpolate data onto another rectangular grid from these files.

In addition to the 3D gas-phase snapshots, the Lagrangian data of the parcel are saved at the same frequency and are available for computing the spray droplet statistics. A post-processing script that translates the Lagrangian quantities onto a Eulerian grid via filtering is also available. A single droplet snapshot is ~50 MB in size.

Because the 3D gas-phase snapshots are rather large, they could not be collected at higher frequencies. However, the simulation collects high-frequency data at $10^6$ Hz for ~200 probe points distributed throughout the computational domain. These points are uniformly placed along the *x*/*y*/*z* directions within the combustor, through the nozzle, and within the exit plenum. These data can be used for accurately computing the frequency characteristics of the system.

Finally, although time-averaged statistics (mean, root mean square [RMS]) can be computed by using the output 3D snapshots, fine-grained time averaging is also conducted within the code, and the mean and RMS primitive quantities are output for the entire 3D domain. These quantities include the primitive variables, such as velocity, temperature, pressure, density, species mass fractions, and reaction rates. The size of a single time-averaged file is ~4 GB.
A summary of available data, processing software, and their use by RTRC (direct noise and indirect noise) and GT ROM teams (hydrodynamics and flame) is provided in Figure 28.

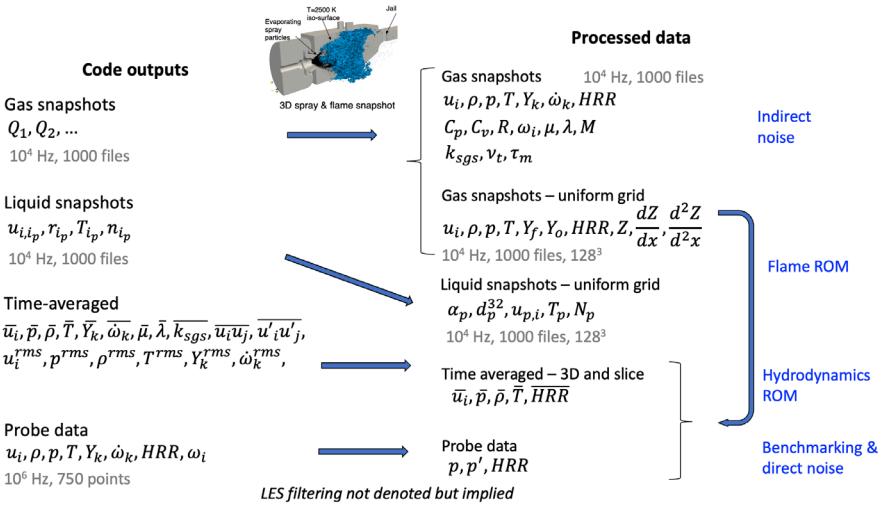


**Figure 28.** Schematic showing the LES data-processing workflow.

## Milestones

- Validation of LES completed at baseline conditions against GT experiments.
- Reactive flow LES conducted at three operating conditions, two from the GT and RTRC experimental campaign.
- Collection of at least 1,000 3D snapshots for each operating condition; provision of data for baseline operating conditions to GT ROM and RTRC teams; data at other conditions awaiting further processing and transfer.
- Creation and updating of a post-processing pipeline for 3D gas-phase and spray snapshots; available to GT ROM team and RTRC as needed.

## Major Accomplishments

Efforts during the first 2 years focused primarily on updates in rig geometry and establishing a workflow for the CFD simulations. In Year 3, validation of LES against experiments was completed, and two additional conditions were considered; 3D snapshots, high-frequency probe data, and time-averaged statistics were collected; and post-processing scripts were developed to aid GT ROM and RTRC teams.

## Publications

### Published conference proceedings

Panchal, A., & Menon, S. (2023, January 23). Large eddy simulation of combustion noise in a realistic gas turbine combustor. *AIAA SCITECH 2023 Forum*. AIAA SCITECH 2023 Forum, National Harbor, MD & Online.

## Outreach Efforts

None.

## Awards

None.

## Student Involvement

- **Penescu Flavius** (currently an undergraduate student, planning to pursue a Master's degree with a thesis) conducted reactive LES with modified quench jet configuration.
- **Leo Kastenberg** (currently an undergraduate student, planning to pursue a master's degree with a thesis) worked on developing post-processing scripts for 3D snapshots.
- **Maxwell Hall** (undergraduate) partly worked on post-processing the high-frequency trace data.

## Plans for Next Period

The next period under this funding will focus on continued analyses of the available LES data under three operating conditions to understand the significance of the observed frequencies and their relevance in noise generation. The LES dataset for the remaining two operating conditions will be provided to the GT ROM and RTRC teams. We will transition to modeling tone noise and will make corresponding changes in the geometry/grid/boundary conditions in the next period of funding.

# Task 3 – Reduced-Order Modeling

Georgia Institute of Technology

## Objective

The overarching objective of this task is to create quick-action ROMs to accurately predict various aspects of noise generation mechanisms that are then collectively feed into a design tool for noise prediction. The specific objective of the GT ROM task focuses on the head-end physics in the architecture, namely the flow and spray dynamics, flame dynamics, and generation of entropy disturbances by the flame. The spray/flow dynamics feeds into the flame dynamics, thus causing direct combustion noise. The flame dynamics also results in entropy disturbances, which in turn lead to indirect combustion noise at the nozzle. The flame response modeling and the model for the generation of entropy disturbances are provided as inputs to the post-combustion models that will be developed by RTRC. Depending on the prediction results obtained from the RTRC models, these head-end models will be iteratively refined.

## Research Approach

In this reporting period, we focused on ROM tasks pertaining to hydrodynamics, flame dynamics, and entropy generation. We studied the hydrodynamics of a swirling jet by using an in-house hydrodynamic stability analysis tool that captures the leading-order coherent dynamics of the flow field. The goal of the tool is to measure the flow response by studying the velocity disturbances resulting from simulated external forcing noise. The hydrodynamics will eventually result in a velocity model that will be used with the flame dynamics model to generate heat release. We further studied the contributions of different chemical source terms contributing to entropy generation for a premixed flame, excluding the diffusion effects.

**Hydrodynamics modeling**

In this reporting period, we advanced the previously developed hydrodynamic forced response framework to measure the swirling jet global mode response to an imposed boundary forcing function. In this framework, we studied swirling jets as amplifier flows, which, in the literature, have been shown to alter the flow response in the presence of the external noise that can occur during combustion. Apart from the well-known advantages of swirling jets as canonical flow fields in combustion systems, swirling flows usually result in unsteady hydrodynamic structures that can couple with acoustics. Modeling and predicting the hydrodynamic structures can be important, particularly in the presence of combustion, because these structures can interact with and perturb the flame. Hydrodynamic stability analysis has emerged as a tool for modeling the dynamics of swirling flows in recent decades. This type of analysis is particularly useful for predicting receptivity, or the range of frequencies amplified by the flow. That is, hydrodynamics provides a transfer function from the background turbulence to large-scale vortical disturbances (which disturb the flame and consequently produce direct noise). Additionally, hydrodynamic stability analysis is particularly valuable for parametric studies determining the sensitivity of the flow response to major design parameters, thus providing a powerful engineering tool. Traditional global hydrodynamic stability analyses have focused on instability generated within the domain (unforced or natural hydrodynamics). Our effort has been to model how the flow response can be altered if instability is introduced at the inlet in a more global framework.

To study the global mode response to an imposed forcing function, we use the time-averaged combustor flow fields supplied as part of the LESs performed for this project. We decompose the 3D velocity fields into two two-dimensional (2D) slices with the same axial coordinate, denoted the $x$ slice and $y$ slice, as displayed in Figure 29. We then conduct a coordinate transform into cylindrical coordinates. Transforming the data into cylindrical coordinates is advantageous in establishing an axisymmetric geometry for our model.

The governing equations for this analysis include the linearized continuity and momentum equations in their incompressible form:

$$\nabla \cdot \vec{u}' = 0$$
$$\frac{\partial \vec{u}'}{\partial t} + \left(\bar{\vec{u}} \cdot \nabla\right)\vec{u}' + \left(\vec{u}' \cdot \nabla\right)\bar{\vec{u}} + \frac{\nabla p'}{\bar{\rho}} - \nu \nabla^2 \vec{u}' = 0 \quad (1)$$

For this analysis, we use a bi-global stability analysis framework, which allows the calculated modes to significantly vary along two coordinates. Using the axisymmetric configuration of the problem, the velocity and pressure disturbances are assumed to take the following harmonic form shown below. The amplitude of the mode is a function of the radial and spatial coordinates, whereas temporal and azimuthal periodicity is maintained by using the frequency $\omega$ and azimuthal wave number $m$. The azimuthal wave number, $m$, captures the helical modes of swirling jets of interest.

$$g'(r,\theta,z,t) = \hat{g}(r,z)e^{-i(\omega t - m\theta)} \quad (2)$$

The assumption of a bi-global mode in the linearized governing equations results in a set of four coupled partial differential equations. Appropriate boundary conditions for each equation are presented in Table 2.

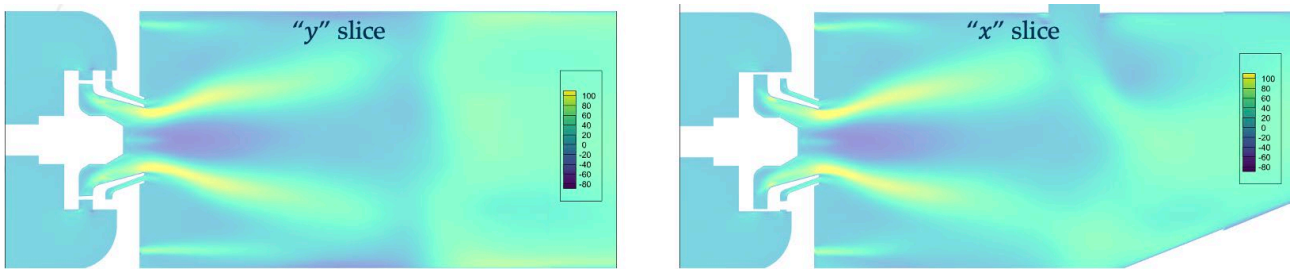


**Figure 29.** Axial velocity contours of a sliced 3D flow field in Cartesian coordinates.

**Table 2.** Boundary conditions for each equation.

| | Axis | Walls | Inlet | Outlet |
|---|---|---|---|---|
| **Radial velocity** | $u_r' = 0$ | $u_r' = 0$ | $u_r' = A_0 e^{-i\omega t}$ | $u_r' = 0$ |
| **Tangential velocity** | $u_t' = 0$ | $u_t' = 0$ | $\frac{\partial u_t'}{\partial \mathbf{n}} = 0$ | $u_t' = 0$ |
| **Axial velocity** | $\frac{\partial u_z'}{\partial \mathbf{n}} = 0$ | $u_z' = 0$ | $\frac{\partial u_z'}{\partial \mathbf{n}} = 0$ | $u_z' = 0$ |
| **Pressure** | $\frac{\partial p'}{\partial \mathbf{n}} = 0$ | $\frac{\partial p'}{\partial \mathbf{n}} = 0$ | $\frac{\partial p'}{\partial \mathbf{n}} = 0$ | $p' = 0$ |

At the centerline, we assume no fluctuations in radial or tangential velocity, to conform with an axisymmetric flow. At the wall, all velocity disturbances must vanish. At the inlet, we impose the inhomogeneous Dirichlet boundary condition for the velocity normal to the inlet plane, to simulate the external boundary forcing for this problem. For the outlet, homogeneous Dirichlet boundary conditions are imposed for velocity and pressure disturbance amplitudes.

We developed a code to solve the equations by using finite elements in COMSOL software. To validate the code, we used a historical dataset with an axisymmetric base flow. Natural hydrodynamics was tested with an unforced global analysis. We correlated the growth rates of unstable modes with the Strouhal number (oscillatory frequencies) to validate the linear trend predicted in the literature, and we ensured that the code accurately captured the unstable solutions.

After validation with historical data, the model was used to obtain bi-global modes for LES base flow data. A snapshot of a forced global mode shape of the axial velocity with a forced inhomogeneous Dirichlet boundary condition at the inlet is shown in Figure 30. The bulk of the disturbances can be qualitatively observed to occur in the shear layers of the flow domain.

To quantitively measure the flow response to forcing, we formulated a transfer function to observe the response in shear layers of forced modes. In a one-dimensional (1D) setting, we probe the axial velocity of modes at axial location ($z/d_{Sw} = 1.32$) and march radially through the shear layer to measure the amplitude of disturbance. Nine probes are placed at the axial location to evaluate the magnitude of the axial velocity disturbance, as shown in Figure 31.

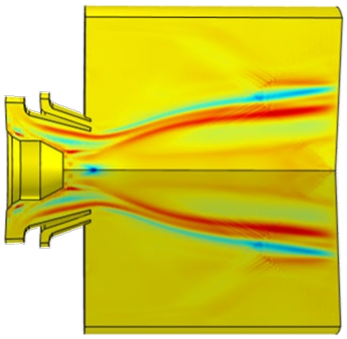

**Figure 30.** Mode shape of axial velocity disturbance modes at $f = 150$ Hz, on the basis of LES baseflow data.

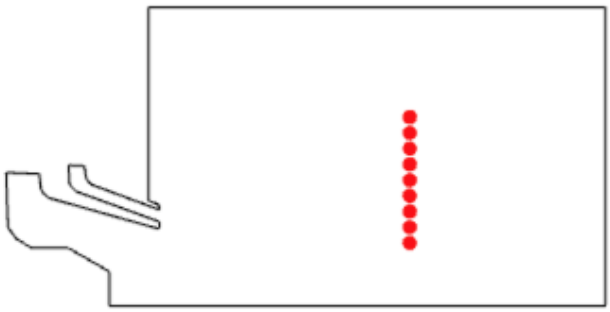

**Figure 31.** One-dimensional probe window for the empirical transfer function.

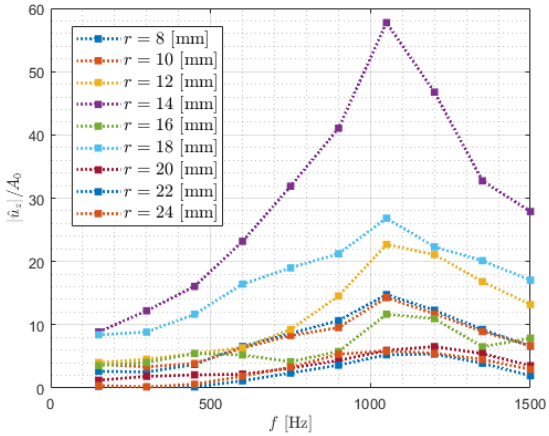


**Figure 32.** One-dimensional empirical transfer function at $z/d_{Sw} = 1.32$.

The normalized amplitude of the axial velocity disturbance ($|\hat{u}_z|/A_0$), where $A_0$ is the amplitude of the inlet velocity forcing, serves as the empirical transfer function for a forced, vortical flow response at frequency $f$. Figure 32 shows the 1D empirical transfer function as a function of forcing frequency. Frequencies for which axial velocity modes are amplified by the inlet introduced disturbance are visible in the figure. The model predicts than the $f = 1050$ Hz mode causes the greatest amplification.

The empirical transfer function was extended across the flow domain, such that flow response was measured by a matrix of 5,673 probes varying across the radial and axial directions. The matrix of probes captures radial, axial, and azimuthal velocity flow disturbances generated because of the imposed forcing. Flow response was again measured as a function of forcing frequency in terms of the Strouhal number: $St = fd/u_0$.

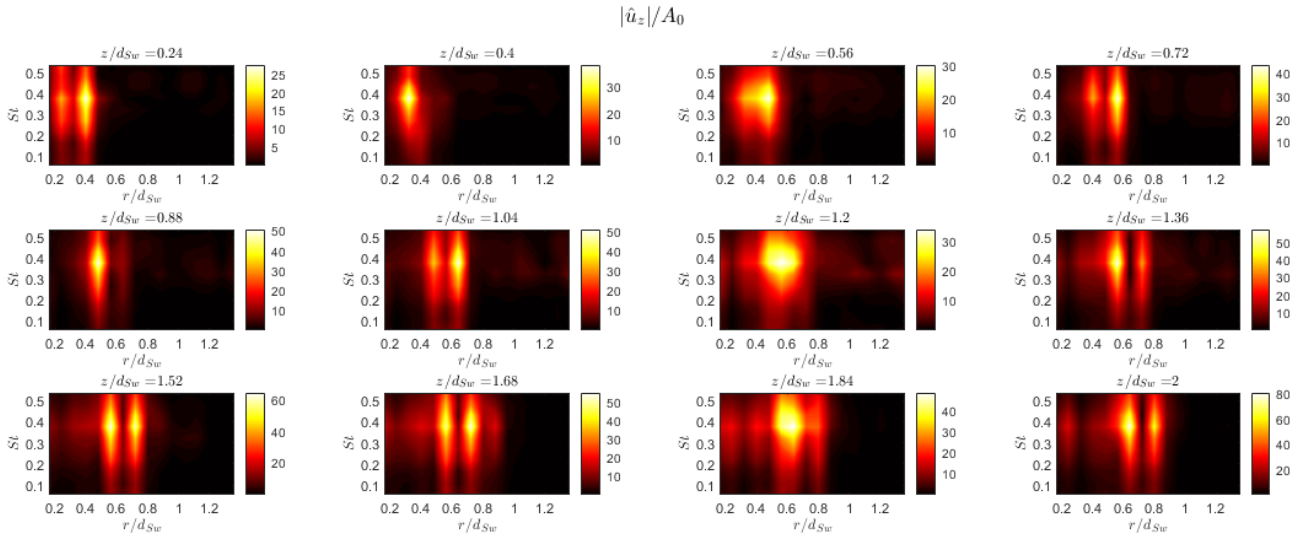


**Figure 33.** Two-dimensional empirical transfer function in an axially and radially varying probe window.

Figure 33 shows the 2D in-space empirical transfer function at various axial locations of the flow domain. The amplification due to forcing is strong around the $f = 1050$ Hz mode for most axial locations. Generally, the amplification strength increases downstream through the flow domain, and at certain axial locations, the inlet introduced forcing is amplified by much as 80 times. The $f = 1050$ Hz or $St = 0.375$ mode is again predominantly responsible for this amplification.

**Flame response modeling**

In the prior reporting periods, we presented the flame response framework for spray flames, along with example flame configurations. The results focused on mean and dynamical flame shapes, as well as the global flame response through the spatially integrated unsteady heat release. All these results focused on static spray parameters with dynamics stemming from only velocity fluctuations. Velocity fluctuations result in spray dynamics: oscillating spray parameters, which have been the focus in the current reporting period. The configuration used for this framework is shown in Figure 34, with fuel droplets injected in a center duct and air injected in the outer ducts. The fuel flows in the inner duct with $0 < r < R_F$, and the air/oxidizer flows in the outer ducts with $R_F < r < R$. The fuel exits the duct and enters the combustion zone as a mixture of fuel gas and a spray of liquid fuel droplets; after evaporation and diffusive mixing, the spray diffusion flame is modeled.

The gaseous ($Z$) and droplet mixture ($Z_d$) fractions are one-way coupled through vaporization of the droplet, which generates fuel gas. Because we consider spray dynamics, the vaporization physics is tightly coupled with the mixture fraction as:

$$\begin{aligned}\frac{\partial Z_d}{\partial t}+u_z\frac{\partial Z_d}{\partial z}+u_r\frac{\partial Z_d}{\partial r}&=\frac{1}{Pe_d}\left(\frac{\partial^2 Z_d}{\partial r^2}+\frac{\partial^2 Z_d}{\partial z^2}\right)-\Gamma_V(Z)Z_d\\ \frac{\partial Z}{\partial t}+u_z\frac{\partial Z}{\partial z}+u_r\frac{\partial Z}{\partial r}&=\frac{1}{Pe_g}\left(\frac{\partial^2 Z}{\partial r^2}+\frac{\partial^2 Z}{\partial z^2}\right)+\Gamma_V(Z)Z_d\end{aligned} \tag{3}$$

In contrast to the earlier formulation, in which $\Gamma_V$ was a constant and independent of the mixture fraction, here we couple $\Gamma_V$ to the system because of the focus on spray dynamics, thus resulting in a non-linear set of equations. We linearize this system and expand to obtain the steady-state mixture fractions (subscript 0), governed as follows:

$$\begin{aligned}u_{z,0}\frac{\partial Z_{d,0}}{\partial z}+u_{r,0}\frac{\partial Z_{d,0}}{\partial r}-\frac{1}{Pe_d}\left(\frac{\partial^2 Z_{d,0}}{\partial r^2}+\frac{\partial^2 Z_{d,0}}{\partial z^2}\right)+\Gamma_V(Z_0)Z_{d,0}&=0\\ u_{z,0}\frac{\partial Z_0}{\partial z}+u_{r,0}\frac{\partial Z_0}{\partial r}-\frac{1}{Pe_g}\left(\frac{\partial^2 Z_0}{\partial r^2}+\frac{\partial^2 Z_0}{\partial z^2}\right)-\Gamma_V(Z_0)Z_{d,0}&=0\end{aligned} \tag{4}$$

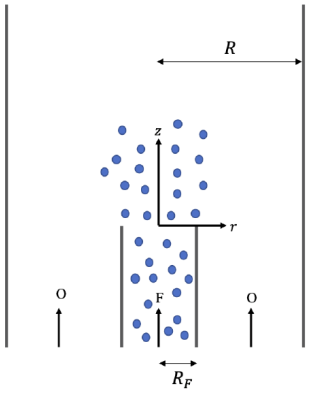


**Figure 34.** Schematic of the ducted spray flame configuration. Fuel droplets are injected in the center duct (blue), and oxidizer gas is injected in the outer ducts.

The fluctuations in the mixture fractions (subscript 1) are then governed by the following equations:

$$\begin{aligned}\frac{\partial Z_{d,1}}{\partial t}+u_{z,0}\frac{\partial Z_{d,1}}{\partial z}+u_{r,0}\frac{\partial Z_{d,1}}{\partial r}-\frac{1}{Pe_d}\left(\frac{\partial^2 Z_{d,1}}{\partial r^2}+\frac{\partial^2 Z_{d,1}}{\partial z^2}\right)+\Gamma_V(Z_0)Z_{d,1}&=-\left(\Gamma'_{V,0}(Z_0)Z_{d,0}\right)Z_1-u_{z,1}\frac{\partial Z_{d,0}}{\partial z}-u_{r,1}\frac{\partial Z_{d,0}}{\partial r}\\ \frac{\partial Z_1}{\partial t}+u_{z,0}\frac{\partial Z_1}{\partial z}+u_{r,0}\frac{\partial Z_1}{\partial r}-\frac{1}{Pe_g}\left(\frac{\partial^2 Z_1}{\partial r^2}+\frac{\partial^2 Z_1}{\partial z^2}\right)+\left(\Gamma'_{V,0}(Z_0)Z_{d,0}\right)Z_1&=\Gamma_V(Z_0)Z_{d,1}-u_{z,1}\frac{\partial Z_0}{\partial z}-u_{r,1}\frac{\partial Z_0}{\partial r}\end{aligned} \tag{5}$$

The boundary conditions are the same as before. The above system is solved for both the droplet and gaseous mixture fractions. However, the equations are notably non-linear in the steady-state mixture fractions, owing to the nature of coupling spray dynamics into the system. However, the system dynamics remains linear (subscript 1). Using the steady state and dynamics of the mixture fractions, we can then consider the heat release dynamics. Derived from the previous report, the normalized unsteady HRR dynamics or flame transfer function is defined as:

$$\hat{F}=\frac{\int_0^{L_{f,0}}\left.\frac{\partial \hat{Z}_1}{\partial r}\right|_{r=\xi_0(z)}dz+\int_0^{L_{f,0}}\hat{\xi}_{1,n}\left.\left[\frac{\partial^2 Z_0}{\partial r\partial z}\sin\theta_0-\frac{\partial^2 Z_0}{\partial r^2}\cos\theta_0\right]\right|_{r=\xi_0(z)}dz}{\int_0^{L_{f,0}}\left.\frac{\partial Z_0}{\partial r}\right|_{r=\xi_0(z)}dz} \tag{6}$$

Here, $L_{f,0}$ is the mean flame height, and transverse diffusion is assumed to be dominant over axial diffusion. The local mean flame angle is denoted $\theta_0$ and is determined from the mean flame position as follows:

$$\tan\theta_0(z) = \frac{d\xi_0(z)}{dz} \tag{7}$$

For illustration, let us consider the following flow field:

$$\begin{aligned} u_{z,0} &= u_0 \qquad u_{z,1} = u_0 \cos(\mathrm{St}(t - k_c z)) \\ u_{r,0} &= u_{r,1} = 0 \end{aligned} \tag{8}$$

Here, $\mathrm{St} = \omega R/u_0, k_c = u_0/u_c$ are the non-dimensional frequency (Strouhal number) and a non-dimensional disturbance convection parameter. Figure 35 shows the variation in the gain (amplitude) and phase of the flame transfer function for different effects of spray dynamics. The baseline gaseous diffusion flame case (no spray) is shown in black. We consider two cases: spray-only injection (red) and partial liquid injection (blue). The spray-only injection case corresponds to the injection of fuel in only its liquid/spray form. We first consider the spray-only case without any spray dynamics, as shown by the solid red curve. When spray dynamics is included, the flame transfer function noticeably changes to the dashed red curve, thus indicating the importance of including this aspect of physics. If we consider the case with partial injection of fuel gas and fuel droplets (blue), the effect of disturbance propagation, $k_c$, is evident (dashed blue vs. dotted blue). This parameter notably affects the nature of constructive/destructive interference; consequently, although the qualitative nature of the curves remains unchanged, key features such as peaks and minima are shifted in the Strouhal number space.

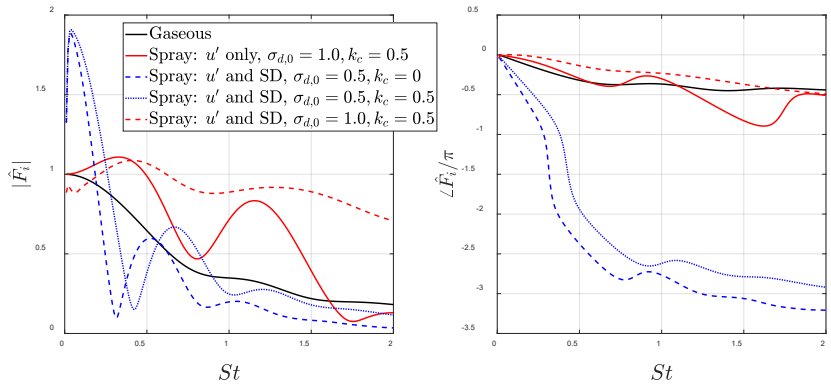


**Figure 35.** Effects of spray dynamics on the global flame response, showing gain (left) and phase (right).

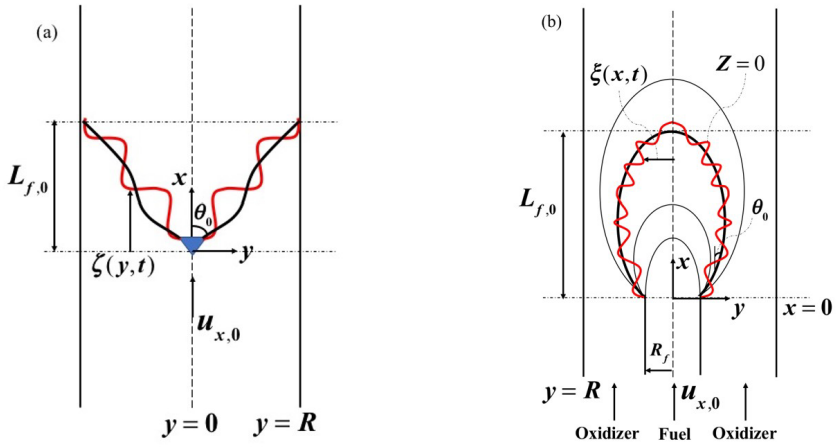


**Figure 36.** Schematic of (a) premixed and (b) non-premixed flame configurations.

**Estimation of flame-generated entropy**

In the previous report, we showed that for air-breathing systems under relevant operating conditions, the heat release is the major source term at the flame for entropy generation.

$$\rho\frac{Ds}{Dt}=\frac{\dot{q}}{T}$$
$$\Rightarrow \rho\left(\frac{\partial s}{\partial t}+\vec{u}\cdot\nabla s\right)=\dot{s}_{gen}=\frac{\dot{q}''}{T_b}\delta(\vec{x}-\vec{x_f}) \quad (9)$$

We define an entropy transfer function, which is the ratio of a normalized entropy fluctuation and the normalized excitation amplitude:

$$\Im_s=\frac{(\hat{s}_1/\tilde{S})}{(\hat{F}_1/F_0)} \quad (10)$$

Here, $\tilde{S}=\dot{Q}_0/\rho T_b R u_{x,0}$, and $\hat{F}_1/F_0$ is the excitation amplitude normalized by its mean value. For most practical configurations, flames are convectively non-compact for a broad range of frequencies of interest; thus, these non-compactness (or equivalently phase cancellation) effects are significant and profound. Although general results can be developed independently of flame geometry/configuration in the convectively compact case, the problem is generally configuration dependent. We consider two model problems for premixed and non-premixed flames, as shown in Figure 36. An explicit expression for the HRR fluctuations of a premixed and non-premixed flame can be derived. Calculations show that, in response to velocity fluctuations, entropy fluctuations are not generated by a premixed flame. This zero-response result also holds if the results are generalized to include the flame stretch sensitivity, thus leading to burning rate fluctuations for reasons discussed later. For the non-premixed flame configuration, in the high Peclet limit, we obtain the same result showing that velocity-driven flames may have a flame response but not an overall entropy response.
Using a linear perturbation expansion, we decompose Eq. (9) into two equations for the perturbation and mean as:

$$\frac{\partial s_1}{\partial t}+\vec{u_0}\cdot\nabla s_1=-\vec{u_1}\cdot\nabla s_0+\left(\frac{\dot{s}_{gen}}{\rho}\right)_1 \quad (11)$$

$$\vec{u_0}\cdot\nabla s_0=\left(\frac{\dot{s}_{gen}}{\rho}\right)_0 \quad (12)$$

Assuming harmonic velocity disturbances propagating in the axial direction, we have:

$$u_{x,1} = \varepsilon_{u,x} u_{x,0} f_x(x) e^{-i\omega t}$$
$$u_{y,1} = \varepsilon_{u,y} u_{x,0} f_y(x) e^{-i\omega t} \tag{13}$$

Here, $f_x$ and $f_y$ are complex functions describing the change in disturbance magnitude and spatial phase dependence, and similarly, equivalence ratio perturbation evolving axially is defined by:

$$\phi_1 = \varepsilon_\phi \phi_0 f_\phi e^{-i\omega t} \tag{14}$$

Expanding Eq. (11) in the frequency domain and simplifying results in:

$$-i\omega \hat{s}_1 + u_{x,0}\frac{\partial \hat{s}_1}{\partial x} = -\hat{u}_{x,1}\frac{\partial s_0}{\partial x} - \hat{u}_{y,1}\frac{\partial s_0}{\partial y} + \frac{\hat{S}_{L,1} h_{R,0}\delta(x-\zeta_0(y))}{T_{b,0}\sin\theta_0} + \frac{S_{L,0}\hat{h}_{R,1}\delta(x-\zeta_0(y))}{T_{b,0}\sin\theta_0}$$
$$- \frac{S_{L,0} h_{R,0}\hat{T}_{b,1}\delta(x-\zeta_0(y))}{T_{b,0}^2\sin\theta_0} + \frac{S_{L,0} h_{R,0}\delta(x-\zeta_0(y))}{T_{b,0}}\frac{\partial \hat{\zeta}_1}{\partial y}\cos\theta_0 - \hat{\zeta}_1\frac{S_{L,0} h_{R,0}\delta'(x-\zeta_0(y))}{T_{b,0}\sin\theta_0} \tag{15}$$

Expanding Eq. (12) results in:

$$\frac{\partial s_0}{\partial x} = \frac{h_{R,0}\delta(x-\zeta_0(y))}{T_{b,0}} \tag{16}$$

After integrating with respect to $x$, differentiating with respect to $y$, and substituting the fluctuating flame position solution, Eq. (15) simplifies to:

$$\hat{s}_1 = \int_0^x \varepsilon_\phi f_\phi(x')\frac{h_{R,0}}{T_{b,0}}\left[\frac{\partial(h_R/h_{R,0})}{\partial(\phi/\phi_0)} - \frac{\partial(T_b/T_{b,0})}{\partial(\phi/\phi_0)}\right]\delta(x'-\zeta_0(y))e^{-\frac{i\omega}{u_{x,0}}(x'-x)}dx'$$
$$- \int_0^x \varepsilon_{u,y} f_y(x')\frac{h_{R,0}}{T_{b,0}}\left[\frac{1}{h_{R,0}}\frac{dh_{R,0}}{dy} - \frac{1}{T_{b,0}}\frac{dT_{b,0}}{dy}\right]H(x'-\zeta_0(y))e^{-\frac{i\omega}{u_{x,0}}(x'-x)}dx' - \int_0^x \varepsilon_{u,y} f_y(x')\frac{ds_{ref}}{dy}e^{-\frac{i\omega}{u_{x,0}}(x'-x)}dx' \tag{17}$$

For the perfectly premixed case, the second two integrals become zero, because $h_{r,0}$ and $T_{b,0}$ are uniform in the transverse direction. Thus, the only contribution for perfectly premixed flames comes from equivalence ratio forcing. Considering the case of a constant flame angle premixed flame, perturbed only by convecting equivalence ratio fluctuations of the form $f_\phi = \exp(i\omega x/u_c)$ (where $u_c$ is the fluctuation phase speed), Eq. (17) results in:

$$\hat{s}_1 = \varepsilon_\phi \frac{h_{R,0}}{T_{b,0}}\left[\frac{\partial(h_R/h_{R,0})}{\partial(\phi/\phi_0)} - \frac{\partial(T_b/T_{b,0})}{\partial(\phi/\phi_0)}\right]\int_0^x \delta(x'-\zeta_0(y))e^{\frac{i\omega x'}{u_c}}e^{-\frac{i\omega}{u_{x,0}}(x'-x)}dx' \tag{18}$$

Here, $x > \zeta(y)$. Thus, for a constant flame angle premixed flame, $\zeta_0(y) = \cot(\theta_0)y$ and $L_{f,0} = R\cot\theta_0$, whereas the mean flow Strouhal number is defined as $St_{L_f} = \omega L_{f,0}/u_{x,0}$, and the Strouhal number based on the disturbance phase speed is defined as $St_c = \omega L_{f,0}/u_c$. Consequently:

$$St_c = St_{L_f} k_c \tag{19}$$

After substituting for $St_c$, simplifying, and evaluating where $\tilde{S} = h_{R,0}/T_{b,0}$, the entropy transfer function for equivalence ratio forcing takes the form:

$$\Im_{s,\phi} = \frac{(\bar{\hat{s}}_1 / \tilde{S})}{\varepsilon_\phi} = \frac{T_{u,0}}{T_{b,0}} \frac{\partial(h_R / h_{R,0})}{\partial(\phi / \phi_0)} \left( \frac{i(1 - e^{iSt_{L_f}(k_c - 1)})}{St_{L_f}(k_c - 1)} \right) e^{\frac{i\omega x}{u_{x,0}}} \tag{20}$$

Eq. (20) gives the entropy fluctuations downstream of the premixed flame configuration. Of note, for $k_c = 1$ (i.e., convective velocity equal to mean flow velocity), no contribution from velocity forcing exists. This simplification, as discussed above, may not accurately evaluate no-compactness effects but in this form is also discontinuous at $k_c = 1$.

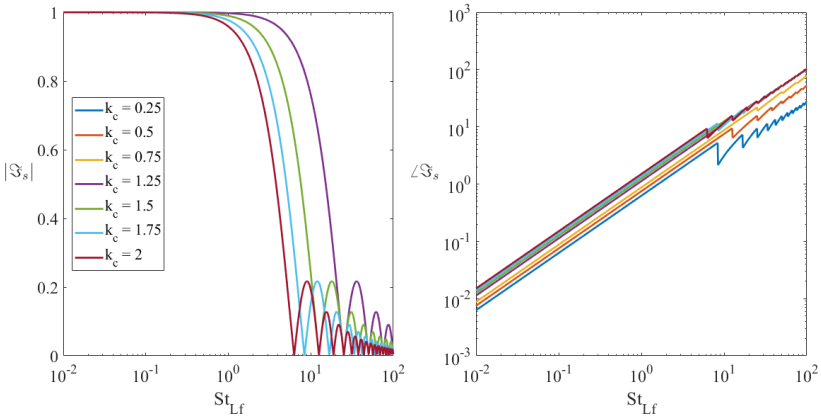


**Figure 37.** Strouhal number, $St_{L_f}$, and $k_c$ dependence of the magnitude (left) and phase (right) of the entropy transfer function $\Im_{s,\phi}$ for a premixed flame with equivalence ratio forcing.

Figure 37 shows the dependence of the magnitude and phase of the premixed flame entropy transfer function. Of note, $k_c = 1$ is not shown, because it is independent of $St_{L_f}$. For $k_c \neq 1$, the transfer function is around 1 and is nearly independent of $St_{L_f}$ until around $St_{L_f} \sim 1$. As the Strouhal number increases, the dependence on frequency is evident, with the typical low-pass-filter behavior. Moreover, because the dependence occurs as $(k_c - 1)$, the curves are similar for $k_c = 0.25$ and $k_c = 1.75$. Additionally, the phase of the transfer function increases with frequency for all cases, with a uniform slope for all $k_c$ values. The sharp jumps in the phase for all cases coincide with the nodes seen in the amplitude of the transfer function. These plots collectively illustrate the effect, and thus the importance, of including $k_c$ in the disturbance model for capturing entropy fluctuations.

For the non-premixed flame, we consider velocity disturbances propagating in the axial direction as above, as well as inlet $(x = 0)$ fuel and oxidizer mass fraction fluctuations given by:

$$\begin{aligned} Y_{f,1}(x = 0) &= \varepsilon_f Y_{f,i,0} e^{-i\omega t} \\ Y_{ox,1}(x = 0) &= \varepsilon_{ox} Y_{ox,i,0} e^{-i\omega t} \end{aligned} \tag{21}$$

Eq. (16) leads to:

$$s_0 = s_{ref}(y) - (v_f W_f + v_{ox} W_{ox}) D \frac{h_{R,0}}{T_{b,0} u_{x,0}} \int_0^x \frac{\partial Z_0}{\partial y} \delta(y - \xi_0(x')) dx' \tag{22}$$

Now, given frequency-domain entropy fluctuations in the linear limit, and noting that entropy fluctuations averaged in the transverse direction satisfy $\bar{\hat{s}}_1 = \int_0^R \hat{s}_1 dy$, and solving as a linear differential equation, Eq. (11) results in:

$$\bar{\hat{s}}_1 = \int_0^{L_{f,0}} \frac{e^{\frac{i\omega}{u_{x,0}}x'}}{u_{x,0}R}\Bigg\{-\int_0^R \hat{u}_{y,1}\frac{\partial s_0}{\partial y}dy + D(v_f W_f + v_{ox}W_{ox})\Big(\Big[\frac{u_{x,1}}{u_{x,0}}\frac{h_{R,0}}{T_{b,0}}\frac{\partial Z_0(x',\xi_0(x'))}{\partial y} - \frac{h_{R,0}}{T_{b,0}}\frac{\partial \hat{Z}_1(x',\xi_0(x'))}{\partial y} - \frac{\hat{h}_{R,1}}{T_{b,0}}\frac{\partial Z_0(x',\xi_0(x'))}{\partial y} + \frac{h_R,0\hat{T}_{b,1}}{T_{b,0}^2}\frac{\partial Z_0(x',\xi_0(x'))}{\partial y}\Big] - \hat{\xi}_1\frac{h_{R,0}}{T_{b,0}}\frac{\partial^2 Z_0(x',\xi_0(x'))}{\partial y^2}\Big)\Bigg\}dx' \tag{23}$$

After simplifying via the solutions for $Z_0$ and $\hat{Z}_1$, substituting Eq. (22), and assuming $\varepsilon = \varepsilon_f = \varepsilon_{ox}$, Eq. (23) is reduced to:

$$\bar{\hat{s}}_1 = -\frac{e^{\frac{i\omega}{u_{x,0}}x}}{u_{x,0}R}D(v_f W_f + v_{ox}W_{ox})\Big[\int_0^{L_{f,0}}\varepsilon\frac{h_{R,0}}{u_{x,0}T_{b,0}}\Big(-\frac{\partial\hat{Z}_1\big(x',\xi_0(x')\big)}{\partial y}\Big)dx' + \int_0^{L_{f,0}} e^{-\frac{i\omega}{u_{x,0}}x'}\frac{h_{R,0}}{u_{x,0}T_{b,0}}\Big(\frac{\hat{h}_{R,1}}{h_{R,0}} - \frac{\hat{T}_{b,1}}{T_{b,0}}\Big)\frac{\partial Z_0\big(x',\xi_0(x')\big)}{\partial y}dx'\Big] - \frac{e^{\frac{i\omega}{u_{x,0}}x}}{u_{x,0}R}\int_0^{L_{f,0}} e^{-\frac{i\omega}{u_{x,0}}x'}\varepsilon_{u,y}u_{x,0}f_y(x')\big(s_{ref}(y=R) - s_{ref}(y=0)\big)dx' \tag{24}$$

Importantly, the first two terms represent the entropy contribution due to mass fraction fluctuations, and the third term represents the entropy contribution due to velocity forcing. In addition, no dependence on $k_c$ is observed for the mass fraction fluctuation terms; i.e., their entropy contributions are constant with respect to $k_c$ and $St_{L_f}$, and vary only with ventilation parity. This aspect is clear because of the presence of the velocity forcing of the form $f_y(x') = \exp\big(i\omega x'/u_c\big)$ in the third term. Thus, defining the velocity forcing entropy contribution:

$$\hat{s}_{1,v} = -\frac{\varepsilon_{u,y}}{R}\int_0^{L_{f,0}} e^{-\frac{i\omega}{u_{x,0}}x'}e^{\frac{i\omega}{u_c}x'}\big(s_{ref}(y=R) - s_{ref}(y=0)\big)dx' \tag{25}$$

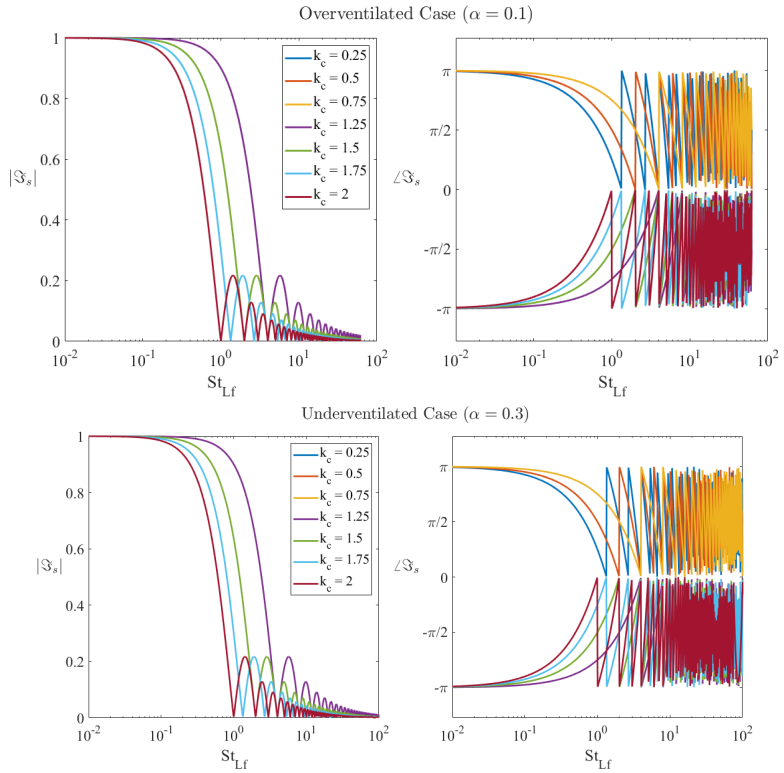


**Figure 38.** Strouhal number and $k_c$ dependence of the magnitude (left) and phase (right) of the entropy transfer function for overventilated (top) and underventilated (bottom) non-premixed velocity forced flames (Pe = 50).

Simplifying, where $\Delta s_{ref} = \left(s_{ref}(y=R) - s_{ref}(y=0)\right)$, we have:

$$\hat{s}_{1,v} = -\frac{\varepsilon_{u,y}}{R}\Delta s_{ref}\int_0^{L_{f,0}} e^{-\frac{i\omega}{u_{x,0}}x'} e^{\frac{i\omega}{u_c}x'} dx' \tag{26}$$

Thus, the velocity forcing entropy contribution is expressed as:

$$\hat{s}_{1,v} = -\frac{L_{f,0}}{R}\frac{\varepsilon_{u,y}\Delta s_{ref}}{iSt_{L_f}(k_c-1)}\left[e^{iSt_{L_f}(k_c-1)} - 1\right] \tag{27}$$

Here, $St_{L_f} = \omega L_{f,0}/u_{x,0}$. Thus, the entropy transfer function contribution due to velocity forcing takes the form:

$$\Im_{s,v} = \frac{(\hat{s}_{1,v}/\Delta s_{ref})}{(\hat{u}_{y,1}/u_{x,0})(L_{f,0}/R)} = -\frac{1}{iSt_{L_f}(k_c-1)}\left[e^{iSt_{L_f}(k_c-1)} - 1\right] \tag{28}$$

Figure 38 shows the non-premixed transfer function amplitude and phase for an overventilated and an underventilated case. Of note, in the case of $k_c = 1$, the magnitude of the transfer function is constant with respect to $St_{L_f}$ and is not shown. In both cases, the low Strouhal Number limit clearly extends to approximately $St_{L_f} = 1$. Furthermore, like the premixed flame equivalence ratio-based entropy transfer function described earlier, the magnitude in both cases is

symmetric about $k_c = 1$, because of the $(k_c - 1)$ term. In addition, the magnitude plots have the same profile for all values of $k_c$, with the rightmost curves occurring nearest to $k_c = 1$, and the leftwardness of the curve being dependent on the distance from $k_c$. Finally, the overventilated and underventilated flame configurations both have the same profile and maximum magnitude. Thus, for convecting velocity disturbances, the profile of the magnitude can be inferred to be insensitive to the flame configuration as well as the scale.

In summary, in the previous reporting period, our work on convectively compact flames was independent of flame geometry and the entropy generation was captured through simple integration across the heat release region. In this reporting period, we extended the prior frameworks to include convective non-compactness by considering geometry effects explicitly. Two model problems focusing on premixed and non-premixed flames were presented to illustrate this effect. Convective non-compactness was measured with the non-dimensional parameter $k_c$, which indicates the deviation of the phase speed of the imposed disturbance (velocity or mixture/equivalence ratio) from the mean flow speed. A key motivation was that prior modeling showed that when $k_c = 1$, the entropy transfer functions were independent of frequency. However, in this work, we extended the analytical results to show the existence of a strong low-pass-filter characteristic to the entropy transfer function, wherein the transfer function magnitude was constant in the $St_{L_f} \leq 1.0$ region with a symmetry in behavior around $k_c = 1$, because the dependence was $(k_c - 1)$ in the transfer function terms. For higher frequencies, the low-pass-filter nature implies that, assuming disturbance phase speeds equal to the mean flow speed can lead to erroneous results for the entropy transfer function. This finding has important implications for modeling the effect of indirect noise from these entropy transfer functions. In future work, we will further extend these models to consider phase speeds that are non-uniform and will consider the additional molecular-transport-based source terms in the entropy governing equation through a scaling study.

**Modeling *p′–q′* correlation/coherence**

The objective of this task is to study the correlation between the HRR measured by chemiluminescence and the generated noise, specifically direct noise. This correlation can be further applied to the separation of direct and indirect noise sources through partial coherence methods. In the literature, experimental attempts to separate indirect and direct noise sources in a combustor have relied on partial coherence methods relating temperature measurements to indirect noise sources. However, high-speed temperature measurements in combustors are difficult to perform, and no high-resolution, high-frequency measurements are currently available in the literature. If the same principles can be applied for chemiluminescence and direct noise, an alternative approach to source separation of combustor noise could be developed. However, the coherence between the HRR and direct noise is not fully understood, because little literature has reported coherence, and the few existing studies have shown values well below unity. The initial goal of this task was to investigate the effects of near-field effects and noncompactness on coherence to explain the low values of coherence found in the literature, and to provide an in-depth understanding of coherence.

As a motivator for this task, the coherence between acoustic measurements and globally integrated chemiluminescence intensity was calculated as part of Task 1, facility development at GT.

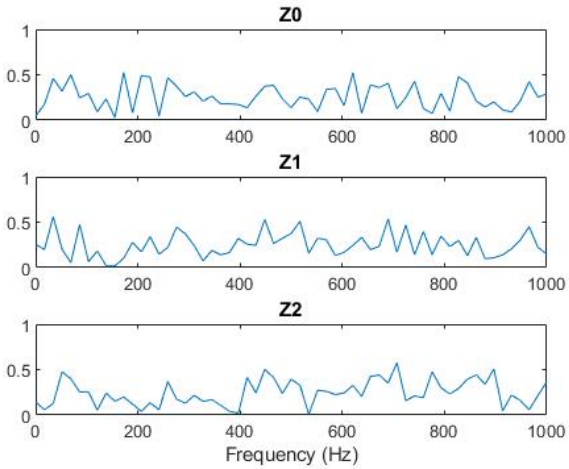


**Figure 39.** Coherence between global chemiluminescence and acoustic pressure measured in the GT rig for approach conditions and a lean (Z1) and rich (Z2) primary zone.

Overall, low values of coherence were observed for all frequencies. Although the available data were not sufficient to determine accurate values, they were sufficient to motivate further investigation of coherence. To obtain a physical understanding of coherence, we followed an analytical/numerical approach to coherence.

In a turbulent flame, the expansion caused by the local unsteady HRR acts as a distributed monopole source. The relationship between the unsteady heat release and pressure is described through the linear wave equation, written as:

$$\frac{\partial^2 p'(\vec{x},t)}{\partial t^2} - c_u^2 \nabla \cdot \left( \frac{\rho_u}{\rho_0} \nabla p'(\vec{x},t) \right) = (\gamma - 1) \frac{\partial \dot{q}'(\vec{x},t)}{\partial t} \tag{29}$$

Obtaining the solution to Eq. (29) without invoking the acoustically compact or far-field limit yields:

$$\hat{p}'(\vec{x}_0,\omega) = \frac{-i\omega(\gamma-1)}{4\pi c_u^2} \iint \hat{\dot{q}}'(\vec{x}_s,\omega) \frac{e^{ik|\vec{x}_s - \vec{x}_0|}}{|\vec{x}_s - \vec{x}_0|} dS \tag{30}$$

where the variables are their Fourier-transformed counterparts. Consequently, the equation necessary to calculate coherence can be constructed and is written as:

$$G_{QQ} = \iint \hat{\dot{q}}'(\vec{x}_{s_1},\omega) \hat{\dot{q}}'^{*}(\vec{x}_{s_2},\omega) \frac{e^{ik|\vec{x}_{s_1} - \vec{x}_0|}}{|\vec{x}_{s_1} - \vec{x}_0|} \frac{e^{ik|\vec{x}_{s_2} - \vec{x}_0|}}{|\vec{x}_{s_2} - \vec{x}_0|} dS_1 dS_2 \tag{31}$$

$$G_{pp} = \frac{\omega^2 (\gamma-1)^2}{16\pi^2 c_u^4} \iint \hat{\dot{q}}'(\vec{x}_{s_1},\omega) \hat{\dot{q}}'^{*}(\vec{x}_{s_2},\omega) \frac{e^{ik|\vec{x}_{s_1} - \vec{x}_0|}}{|\vec{x}_{s_1} - \vec{x}_0|} \frac{e^{ik|\vec{x}_{s_2} - \vec{x}_0|}}{|\vec{x}_{s_2} - \vec{x}_0|} dS_1 dS_2 \tag{32}$$

$$G_{Qp} = \frac{i\omega(\gamma-1)}{4\pi c_u^2} \iint \hat{\dot{q}}'(\vec{x}_{s_1},\omega) \hat{\dot{q}}'^{*}(\vec{x}_{s_2},\omega) \frac{e^{ik|\vec{x}_{s_2} - \vec{x}_0|}}{|\vec{x}_{s_2} - \vec{x}_0|} dS_1 dS_2 \tag{33}$$

$$\gamma_{Qp}^2 = \frac{\left|G_{Qp}\right|^2}{G_{pp}G_{QQ}} \tag{34}$$

With Eqs. (31) – (34), the coherence for any flame geometry can be calculated, given the spatiotemporal characteristics of the flame source. To proceed with the analysis, we define an isotropic, exponential decay form of the correlation of the unsteady heat release as:

$$\left\langle \hat{\dot{q}}'(\vec{x}_{s_1},\omega)\hat{\dot{q}}'^{*}(\vec{x}_{s_2},\omega)\right\rangle = \left\langle \hat{\dot{q}}'^{2}\right\rangle \exp\left(-\frac{\left|\vec{x}_{s_1}-\vec{x}_{s_2}\right|^2}{\Lambda^2}\right) \tag{35}$$

The geometry of the flame is taken to be a conical flame with a burner radius $a$ and flame length $L_f$, which covers a wide range of practical applications. The nondimensional parameters affecting coherence are now identified to be the normalized flame correlation length $\Lambda/a$, the compactness factor $a/\lambda$, the distance of the observer from the flame $R/a$, and the flame aspect ratio $L_f/a$. For long flames with $L_f > 2a$, normalizing by $L_f/2$ instead of the radius $a$ is sensible.

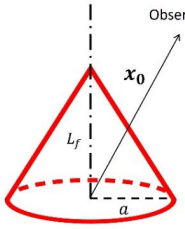


**Figure 40.** Geometry of a conical flame.

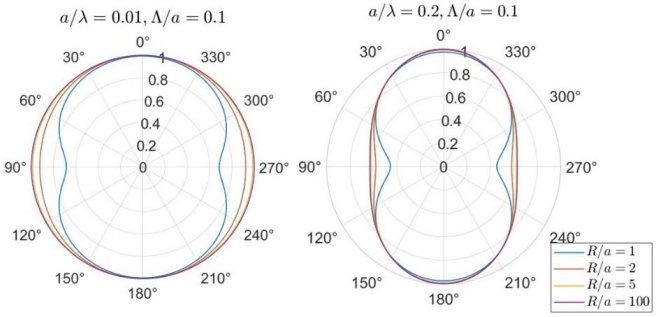


**Figure 41.** Polar plots of coherence for $\Lambda/a = 0.1, a/\lambda = 0.01$ (left) and $\Lambda/a = 0.1, a/\lambda = 0.2$ (right) for varying distance from the center, for a flame with $L_f = 0$.

As shown in Figure 41, near-field effects influence the coherence even at the acoustically compact limit, where the coherence in the far-field limits to unity. Furthermore, noncompactness reduces coherence even in the far-field limit. The minimum value of coherence is when $\phi = \pi/2$, and the maximum value of coherence is when $\phi = 0$.

At large $\Lambda/a$, the coherence is unity for most values of $a/\lambda$, and low coherence is observed at certain wavelengths that form narrowband valleys. The location of these valleys appears to be insensitive to $\Lambda/a$ and $R/a$; the location of the first valley is approximately $a/\lambda \approx 0.6$. As $\Lambda/a$ decreases, coherence is reduced at smaller compactness factors. Furthermore, coherence values do not rise back to unity and stay at lower values. Given that $\Lambda/a < 1$ in many applications of interest, our findings demonstrate that low coherence values can be observed at wavelengths considerably longer than the flame dimensions. Figure 42 also indicates only a weak dependence on the distance, in agreement with the prior observation that coherence does not go to unity even in the far-field limit.

On the centerline, a similar analysis is performed. Overall, the key differences between the coherence when $\phi = 0$ and $\phi = \pi/2$ can be summarized as follows. (a) When $\phi = 0$, coherence is near unity when either the compactness factor is large or the observer is in the far field, whereas when $\phi = \pi/2$, coherence is low even in the far field if the compactness factor is not sufficiently small. (b) Reduction in coherence when $\phi = \pi/2$ occurs at $\Lambda/a, \lambda/a$ values an order of magnitude higher than that when $\phi = 0$. Physically, this outcome is due to the propagation path differences approaching zero on the centerline, whereas a constant path difference exists in the order of the flame width on the burner plane.

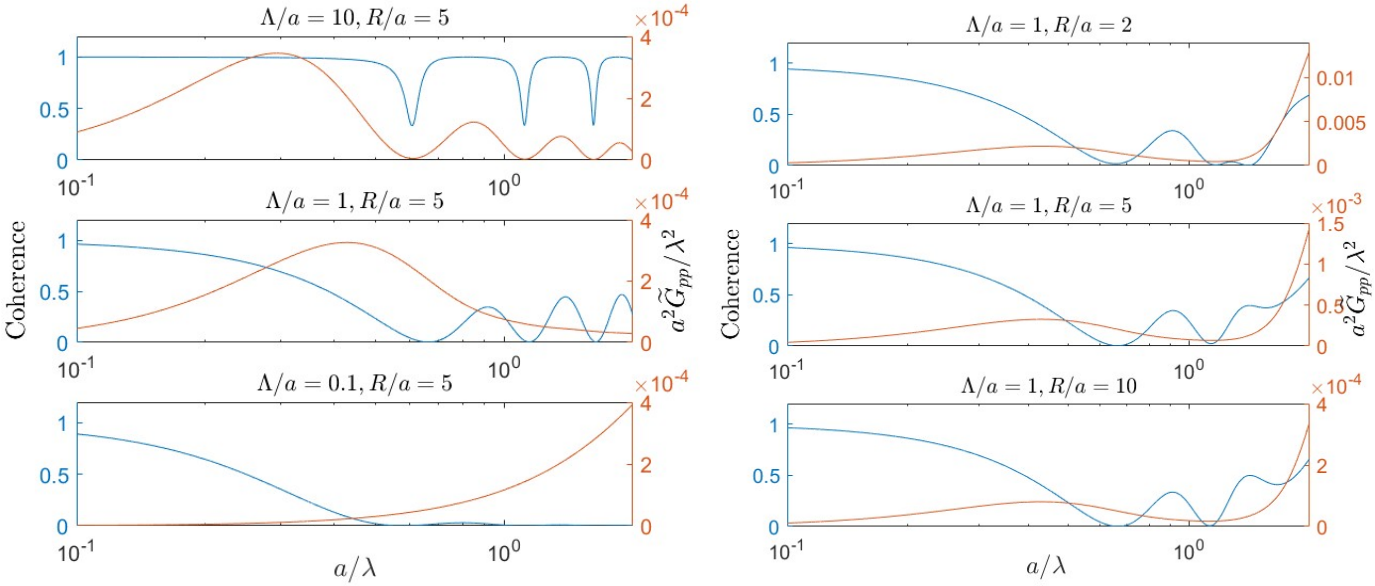


**Figure 42.** Coherence and acoustic power at $\phi = \pi/2$ for various values of $\Lambda/a$, $a/\lambda$, and $R/a$. $L_f = 0$.

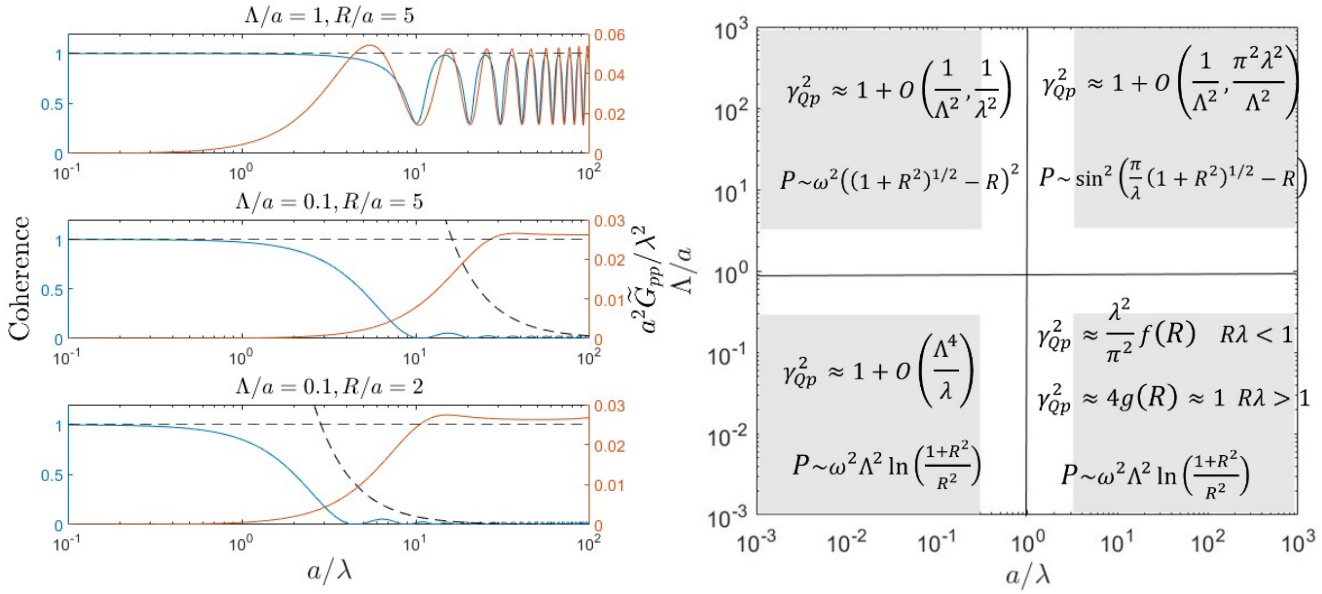


**Figure 43.** Coherence and acoustic power at $\phi = 0$ for various values of $\Lambda/a$, $a/\lambda$, and $R/a$ (left), and asymptotic scaling laws derived analytically (right). $L_f = 0$.

Figure 44 shows the effect of flame geometry on the coherence. In summary, coherence is highest perpendicular to, and lowest along the longest dimension of, the flame. That is, for flames where $L_f/a < 2$, peak coherence values occur at $\phi = 0$, whereas where $L_f/a > 2$, peak coherence values occur at approximately $\phi = \pi/2$. Furthermore, coherence is higher closer to the base of the conical geometry, where the most heat release is present. That is, the region of main heat release has the largest contribution to the globally integrated heat release and to the pressure fluctuations if the observer is close, thus leading to high coherence.

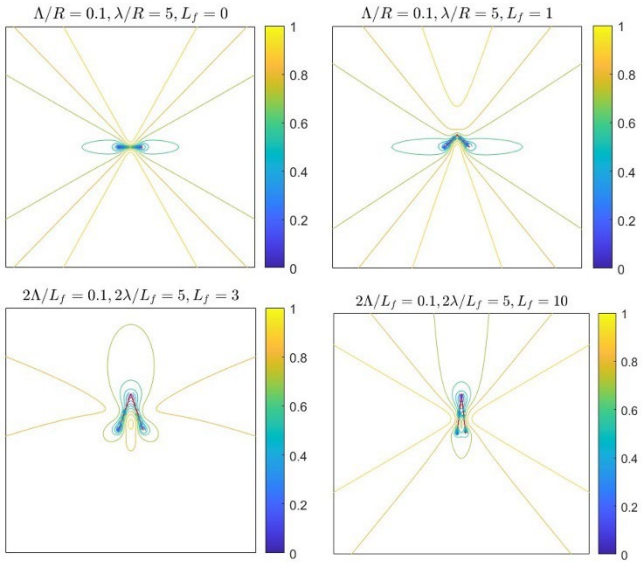


**Figure 44.** Coherence of conical flames of constant compactness factors and correlation lengths for various $L_f$.

## Milestones

- Extended framework for spray dynamics effects on the flame response
- Entropy generation by non-premixed flames for propagating disturbances
- Extended bi-global hydrodynamics study to develop an empirical transfer function to identify forcing frequencies that cause maximum amplification for the LES base flow
- Identification of new research opportunities for investigating the coherence between the global HRR and pressure fluctuations; demonstration that near-field and noncompactness effects can reduce coherence
- Formulation of an analytical framework for coherence studies; demonstration of the effect of flame geometry on coherence

## Major Accomplishments

The flame response framework was extended to a non-linear model for the spray dependence to account for spray dynamics effects. The entropy generation model includes the effects of propagating disturbances.

For the hydrodynamics task, the input–output empirical transfer function predicts amplitude-scaled, linear flow response with a supplied inlet forcing frequency. A sweep of forcing frequencies through the model can identify frequency bands that cause significant amplification. The transfer function can couple well with other tasks aimed at identifying flame response in the presence of in-flow velocity perturbations.

An analytical framework to estimate and study the coherence between the global HRR and direct noise has been developed. This framework provided a partial explanation regarding gaps in the theoretical and experimental literature, and identified the mechanisms of how coherence is reduced. This method of analysis can be used for further study of coherence, possibly extending to confined cases, as in a real combustor.

## Publications

**Published conference proceedings**

Wise, M., John, T. and Acharya, V. (2023, March). Convective Disturbance Effects on Entropy Generation. *13th US National Combustion Meeting, Paper# 180CTM-0210.*

Laksana, A., Patki, P., John, T., Acharya, V., & Lieuwen, T. (2023). Distributed Heat Release Effects on Entropy Generation by Premixed, Laminar Flames. *International Journal of Spray and Combustion Dynamics*. Vol. 15, Issue 3, pp. 139-146.

## Outreach Efforts

None.

## Awards

None.

## Student Involvement

- Graduate student Parth Patki worked on the hydrodynamic stability task under the mentoring of Ben Emerson.
- Graduate student Sungyoung Ha worked on the coherence modeling task under the mentoring of Vishal Acharya and Tim Lieuwen.
- Undergraduate student Michael Wise worked on the entropy generation task under the mentoring of Vishal Acharya.

## Plans for Next Period

The flame response framework will further consider spray dynamics aspects such as droplet transport, droplet grouping, and polydisperse sprays. The ROM will be validated with LES data in an ongoing study comparing the ROM equations to the full equations used for the LES. The entropy generation model will consider the effect of transport terms on entropy for diffusion-based flames and then extend to entropy generation of spray flames.

The hydrodynamics modeling will consider a tri-global framework for generic geometry hydrodynamics. In addition, the velocity ROM will be further built and validated with PIV measurements from the GT experiment task.

The coherence modeling analysis will be extended toward confined configurations to assess applicability to noise source separation in the GT or RTRC rig. An experiment with a canonical flame is planned to verify the analytical results and identify other physical processes affecting coherence.

# Task 4 – Facility Development at RTRC

Raytheon Technologies Research Center

## Objective

The objective of this task is to RQL combustors have been tested at RTRC under the program – one that includes "jailbar" vanes at the combustor exit and closely mirrors the GT design, with a specific focus on the higher-pressure operating points that are not possible for the GT rig, and another one that corresponds to the Pratt & Whitney FAA CLEEN single-sector combustor configuration. Collectively, the GT and RTRC rig capabilities encompass a broad range of operating conditions, thus resulting in a robust dataset for training the design tools.

## Research Approach

During the current reporting period, a third test entry was conducted. This entry was a relatively short test program (1 week) leveraging the FAA CLEEN test rig for the purpose of obtaining dual thermocouple probe data and several other test conditions, to complement the test program in 2022 with the same hardware (except for the fuel mixer). Unfortunately, the probe failed early in the test; however, significant new data were obtained regarding indirect noise with non-combustion operation by introducing entropy fluctuation into the combustor. Lessons learned from this year's entry will be applied to the final rig test in 2024 with the original ASCENT rig. In addition, 2021 data (ASCENT combustor) and 2022 data (CLEEN combustor) were comparatively analyzed.

Figure 45 illustrates the ASCENT and CLEEN combustors' geometric differences, noise spectra, and legacy scaling law plots (from 2021 and 2022 test entries). The most significant difference between the combustors is the relative distance from the combustion zone to the choked exit. The ASCENT rig has a much shorter distance and is typical of current generator aerocombustors, whereas the CLEEN rig is longer, to accommodate a variable-length side branch for studying swirler tonal instability by varying the combustor resonance acoustic modes (which was not used in this investigation, in which the length was fixed). The middle group of plots shows the noise spectra for the CLEEN rig peaks at a lower frequency and is more tonal than the relatively broadband spectra of the ASCENT rig (typical of aerocombustors). With wave decomposition to compute indirect noise (discussed below), the tonal behavior appears to be due to a coupling between the dilution jets and indirect noise.

The plots on the right side of Figure 45 show a legacy scaling comparison. As presented in earlier reporting, the ASCENT rig follows the scaling law quite well, whereas the CLEEN rig scaling is non-typical, tracking at a lower slope, although the scaling reasonably collapses the data.

Figure 46 shows some of the results of non-combustion testing during the third entry (2023), wherein controlled entropy fluctuations were introduced in the absence of combustion noise. Here, the dilution jets were increasing, heated from 200 to 1,000 ˚F while a cold front-end air supply was maintained. The typical unsteadiness of the dilution jets in cross flow was expected to introduce entropy fluctuations of hot and cold lumps of flow that convect through the choke, thus generating indirect noise that should radiate upstream as well downstream.

The plots in Figure 46 show the response of the two pressures upstream of the choke (1 = bulkhead; 3 = combustor exit) and one pressure downstream of the choke (6), as illustrated in the rig image. The top row shows the pressure spectra, and the bottom row shows coherence with the bulkhead pressure). As the temperature of the dilution jets is increased, at low frequency, both the coherence and pressure increase (particularly for 800 and 1,000 ˚F), as expected for indirect noise. A very high level of coherence for pressure signals across the choke was observed for the first time in the program. Normally, the flow noise downstream of the choke from shedding and shock wave hides the indirect noise. The absence of combustion and the apparently high level of entropy fluctuations (>800 ˚F mixing with ~100 ˚F air) made this observation possible, thus providing validation data for indirect noise modeling.

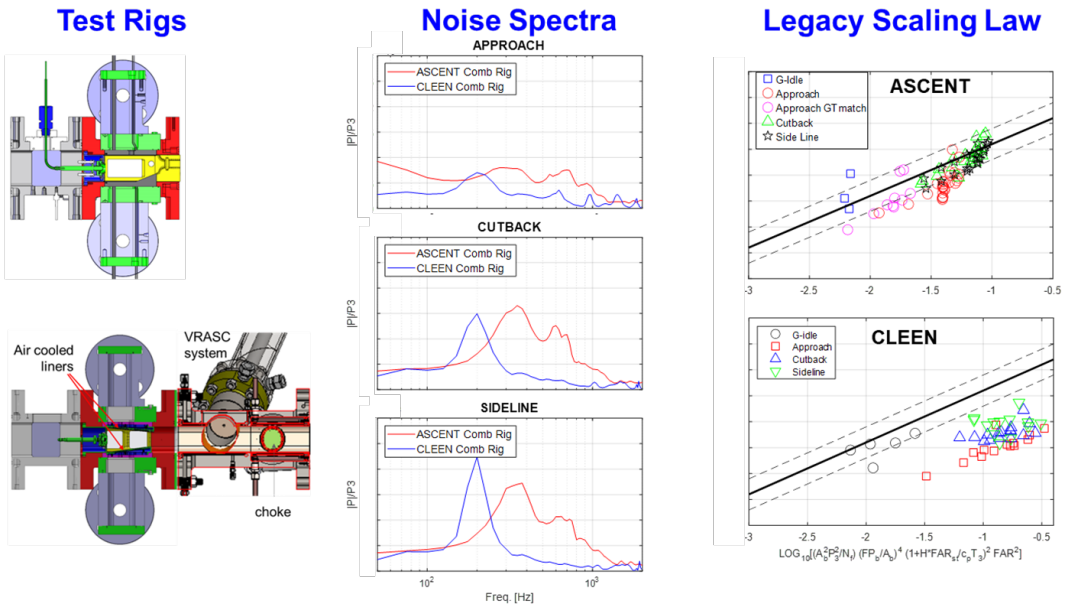


**Figure 45.** Noise comparison between ASCENT and CLEEN combustors.

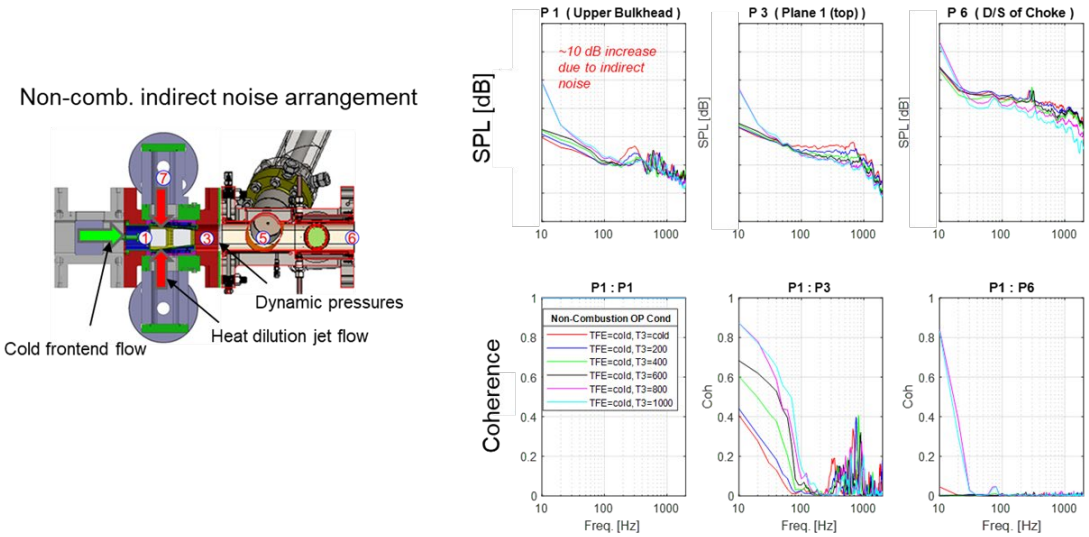


**Figure 46.** Non-combustion indirect noise test with the CLEEN combustor.

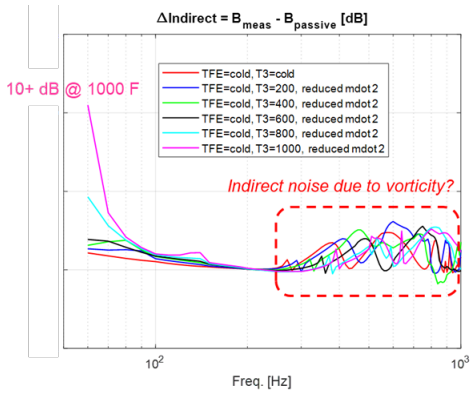


**Figure 47.** Computed indirect noise using wave decomposition consistent with measuredsound pressure levels (SPL)levels.

Indirect noise for this dataset was computed with wave decomposition and is shown in Figure 47. At low frequency, the computed indirect noise is consistent with the observed increase in SPL in Figure 46. This result is also a first for this program, providing validation of the wave-decomposition method of computing indirect noise.

Applying this indirect noise computation to previous datasets provides insight into noise generation in the CLEEN combustor. An example is shown in Figure 48 for FAR sweep of approach conditions. On the left side, the computed indirect noise shows a 3-dB level at low frequencies (independent of FAR) and a very significant increase at ~200 Hz that trends with FAR. Comparison of this frequency with the FEA model indicates that the peak acoustic velocity response in the dilution jets is related to the ~200-Hz indirect noise. The peak acoustic response is due to the plenum bulk mode of the dilution jet feed (illustrated in the image). We speculate that a feedback loop exists between indirect noise and the dilution jet fluctuations (perturbation from jets generates indirect noise that propagates upstream from choke triggering the next cycle of the jet fluctuation).

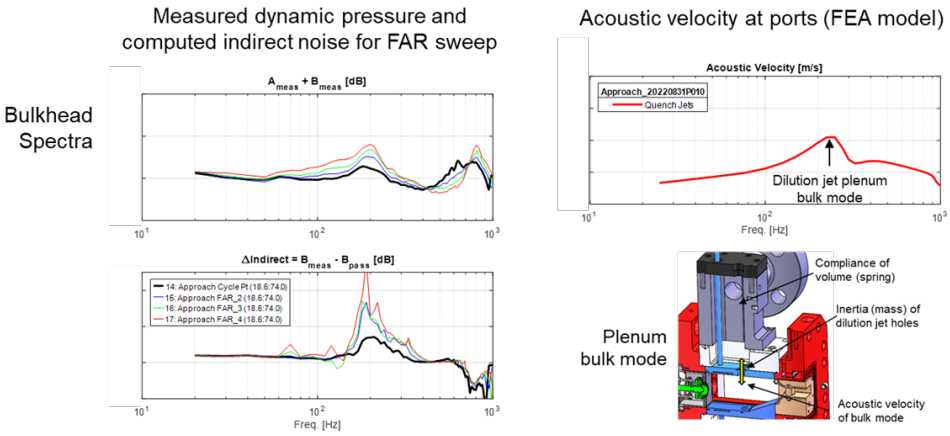


**Figure 48.** Indirect noise for the CLEEN combustor and relationship to acoustic mode.

## Milestones

- Completion of comparison between ASCENT and CLEEN combustor rig results
- Successful completion of the third RTRC experiment entry

## Major Accomplishments

- Validation of wave decomposition for computed indirect noise
- Understanding of the relationship between CLEEN noise spectra and indirect noise/dilution jet coupling

## Publications

None.

## Outreach Efforts

None.

## Awards

None.

## Student Involvement

None.

## Plans for Next Period

Planning and hardware development for the fourth (final) test entry program.

# Task 5 – Post-combustion Modeling

Raytheon Technologies Research Center

## Objective

The objective of this task is to develop transfer functions from the combustion zone to the nozzle, nozzle to turbine, and turbine to far field. This task involves physics modeling of the following aspects:

- Entropy wave transport post-combustion, as unsteady HRR disturbances at the flame generate entropy disturbances that are then transported through the post-combustion zone;
- Nozzle interactions for the dynamics of pressure disturbances through the nozzle, specifically the effect of the jail bar configuration used in both the GT and RTRC rigs;
- Turbine interactions for the dynamics of pressure disturbances through the turbine; and

- Far-field sound propagation.

Direct noise modeling will also be performed with a numerical Green's function approach with the heat release model.

## Research Approach

The post-combustion-zone physics involves the effects of combustion, unsteady HRR disturbances, and post-combustion geometry on the eventual noise generation outside the engine. This modeling involves the following:

- Direct generation of combustion noise due to heat release and the interaction of these pressure disturbances with the remainder of the engine geometry, which leads to far-field noise.
- Entropy disturbances generated by the flame interacting with geometric changes at the nozzle, and causing pressure disturbances that then interact with the remainder of the engine geometry and lead to far-field noise.

**Combustor flow field**

Figure 49(a) shows the RMS of the entropy perturbation within the combustor, by using the GT LES data integrated along the *z* direction. Much of the entropy perturbation is located near the mixing region of the dilution jets. Some entropy perturbation is observed near the flame and cooling flows, but is small with respect to that of the dilution jets. Figure 49(b) shows the area-weighted entropy as a function of frequency along the streamwise direction, and Figure 49(c) shows the entropy power spectrum at two specific locations along the flow. The spectrum near the flame has significantly low-frequency content, but the entropy rolls off at higher frequencies. The peak at 2500 Hz is associated with the quarter wavelength mode of the combustor is discussed later. In the region between the flame and the dilution jets, the entropy content is reduced because of advective dispersion, as described in previous studies. In the absence of dilution jets, this dispersion would be expected to continue up to the combustor exit. Close to the dilution jets, the entropy once again increases at all frequencies because of turbulence. This increased entropy is then advected downstream to the combustor exit. The low-frequency content reduces rapidly, but at frequencies greater than 300 Hz, the entropy level near the combustor exit is greater than that near the flame. Peaks are also present in the entropy spectrum near the choke at 700 Hz and 1000 Hz; these peaks are only weakly present near the flame but are more prominent downstream of the dilution jets. The 2500-Hz peak near the flame is not present near the choke. These findings suggest that not all entropy near the choke is from the flame region alone.

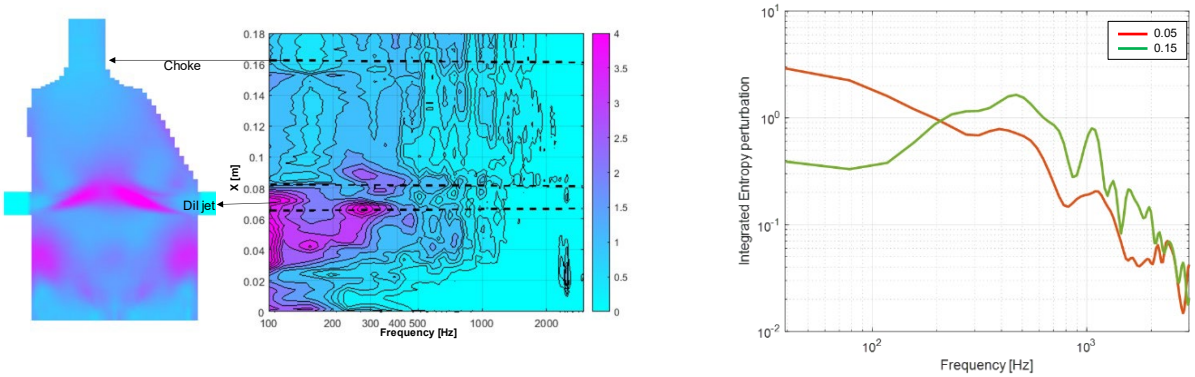


a) RMS of entropy b) Area-weighted integral c) Entropy power spectrum at two streamwise locations

**Figure 49.** Entropy distribution within the combustor.

**Direct noise computation**

The direct noise from the unsteady heat release within the combustor can be computed with the approach outlined by Dowling. The Helmholtz equation (Eq. (36)), where the source term is a function of the HRR per unit volume $(\dot{q}'_v)$, is solved with a finite element package for the unsteady acoustic pressures. The time-averaged density $(\bar{\rho})$ and speed of sound $(\bar{c})$ are obtained from the LES flow field, and the unsteady HRR is obtained from the LES flow field.

$$-\frac{1}{\overline{\rho c}}\frac{\partial^2 p'}{\partial t^2}+\frac{\partial}{\partial x_i}\left(\frac{1}{\overline{\rho}}\frac{\partial p'}{\partial x_i}\right)=-\frac{\gamma-1}{\overline{\rho c}}\frac{\partial \dot{q}'_V}{\partial t} \tag{36}$$

The total integrated HRR from the LES is uniformly distributed over the region of the combustor between the bulkhead and dilution jets.

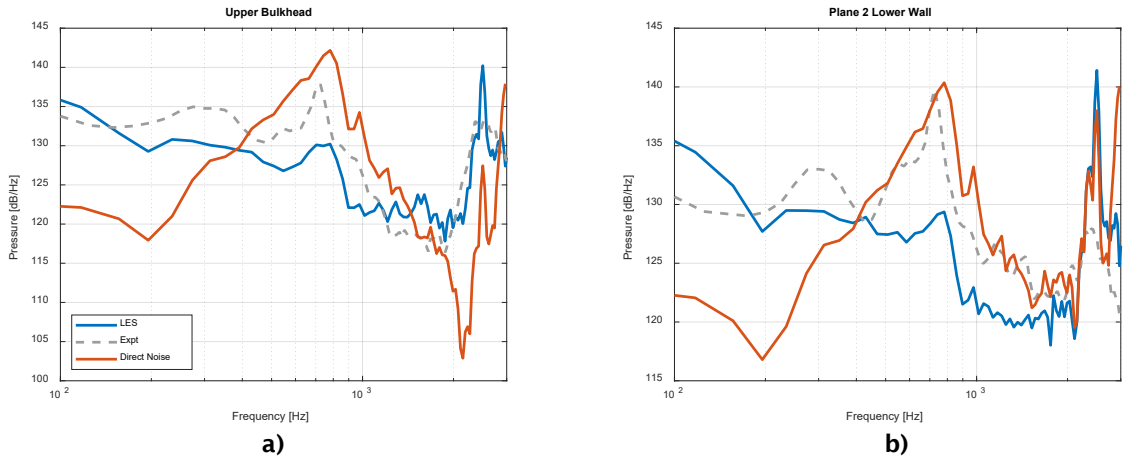


**Figure 50.** Computed direct noise and LES unsteady pressures at the (a) upper bulkhead and (b) lower ramp.

Figure 50 shows the PSD of the computed direct noise with Eq. (36), along with the LES pressures and measured RTRC experimental data at two locations within the combustor. The general shape of the power spectrum between the LES and the measured data is similar, with differences observed near 700-Hz and 2500-Hz frequencies. The LES flow field is saved for 0.17 s at a rate of 10,000 samples per second for a total of 1,700 time steps. The 700-Hz frequency is driven largely by entropy and the turbulence within the flow (discussed below). The lower frequencies are thus not completely free of turbulent noise. Many time steps would be expected to be necessary to fully resolve this entropy driver frequency. The experimental data have been obtained for 30 s; hence, any turbulence-related noise is averaged out. The 2500-Hz tone observed in the LES and the experiment is driven by the longitudinal mode of the combustor. The LES pressures at this frequency are less damped than those in the experiment, probably because the assumption of adiabatic walls in the LES is not entirely true for the combustor rig. This aspect is particularly exaggerated downstream of the dilution jets, where the mean flow temperature is cooler. The experimental rig has a small amount of cooling flow near the observation windows, which further extracts energy and tends to damp out the longitudinal mode to a greater extent than predicted by the LES.

Despite the above-described limitations of the LES dataset, the direct noise computation interestingly predicts the 700-Hz frequency somewhat accurately. However, the lower frequency is significantly lower in magnitude than the experiment as well as the LES. This difference is due primarily to indirect noise sources within the combustor.

**Total noise computation**

The total noise within the combustor is a combination of the direct noise from the unsteady heat release and pressure perturbations generated through the accelerating entropy inhomogeneities near the combustor exit. The acceleration of these entropy inhomogeneities through the choked region at the combustor exit results in acoustic pressure perturbations traveling backward into the combustor and forward into the downstream turbine stages. Accurately estimating the entropy near the combustor exit is not easy for modern combustors including dilution jets or other crossflow features. The current approach is to use the linearized Navier–Stokes equations (LNSEs) for non-reacting flows, as shown in Eq. (37). The LNSEs are obtained by assuming small perturbations for temperature, velocity, and pressure within the flow, and assuming that these perturbations do not in turn affect the mean flow. The LNSEs are modeled as a forced response in the frequency domain with the HRR term as the forcing function and solved with a finite element solver.

$$\frac{D\rho'}{Dt}=\frac{\partial\rho'}{\partial t}+\overline{u}_i\frac{\partial\rho'}{\partial x_i}=-u_i'\frac{\partial\overline{\rho}}{\partial x_i}-\overline{\rho}\frac{\partial u_i'}{\partial x_i}-\rho'\frac{\partial\overline{u}_i}{\partial x_i}$$
$$\overline{\rho}\frac{Du_i'}{Dt}=\overline{\rho}\frac{\partial u_i'}{\partial t}+\overline{\rho u}_j\frac{\partial u_i'}{\partial x_j}=-\overline{\rho}u_j'\frac{\partial\overline{u}_i}{\partial x_j}-\rho'\overline{u}_j\frac{\partial\overline{u}_i}{\partial x_j}-\frac{\partial p'}{\partial x_i}+\eta\left[\frac{\partial^2u_i'}{\partial x_k\partial x_k}+\frac{1}{3}\frac{\partial}{\partial x_i}\left(\frac{\partial u_k'}{\partial x_k}\right)\right] \quad (37)$$
$$\frac{Dp'}{Dt}=\frac{\partial p'}{\partial t}+\overline{u}_i\frac{\partial p'}{\partial x_i}=-u_i'\frac{\partial\overline{p}}{\partial x_i}-\kappa\overline{p}\frac{\partial u_k'}{\partial x_k}-\kappa p'\frac{\partial\overline{u}_i}{\partial x_i}+(\kappa-1)\left\{\Phi'+\lambda\frac{\partial^2T'}{\partial x_k\partial x_k}+\dot{q}_V'\right\}$$

For this set of equations, the time-averaged velocity, density, and pressures are used as the background mean flow. Sharp velocity gradients in the boundary layer and near the dilution jets can result in numerical instabilities when solving the LNSEs. These instabilities are ameliorated by the first smoothing out these gradients before solving the equations. Because the LNSE includes the mean flow velocity, the effect of the high Mach number near the choke is included, and no special treatment must be performed. The region downstream of the choke is treated as a perfectly matched layer, and any acoustic perturbations propagating downstream are absorbed by this region without any reflections. The walls of the combustor are treated as adiabatic slip walls. The outcome of solving this set of equations is the acoustic pressures, along with density and velocity perturbations within the combustor, which can then be used to calculate entropy perturbation as an input to the turbine propagation model.

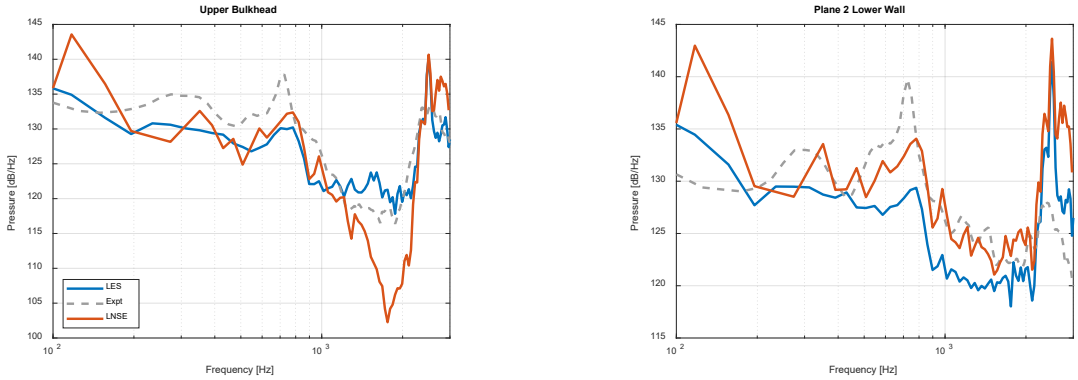


a) b)

**Figure 51.** Total noise inside the combustor, predicted by the LNSEs at the (a) upper bulkhead and b) lower ramp.

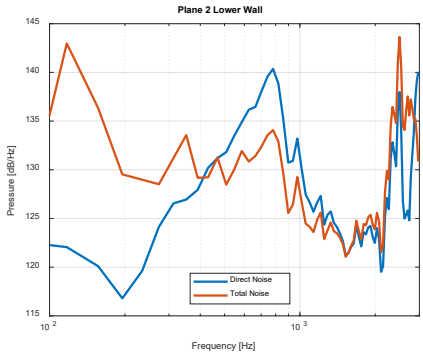


**Figure 52.** Direct and total noise predictions within the combustor.

Figure 51 shows a comparison of the acoustic pressure spectrum predicted by the LNSEs, with the LES and measured experimental data. The LNSEs predict the acoustic pressure within the combustor reasonably well. The acoustic levels at the low frequencies compare very well with both the LES and the experimental findings. The differences at these frequencies with the direct noise computations (Figure 50) are due to entropy-related noise or indirect noise. The peak at

700 Hz is also predicted by the LNSE but is smaller than that predicted by the direct noise alone, and therefore may be a result of the combination of unsteady heat release fluctuation and the entropy-generated noise at this frequency. Comparison of the predictions of the LNSE and the direct noise indicates that the largest effect of entropy is at low frequencies below approximately 800 Hz. Some differences are observed at higher frequencies but are likely to be due to the incorrect impedance at the choke used in the Helmholtz equation. Thus, the indirect noise at low frequencies can be as much as 10 dB higher than the direct noise.

**Modal decomposition of the flow field with spectral proper orthogonal decomposition**

Modal decomposition of the flow field is performed with spectral proper orthogonal decomposition (SPOD), which decomposes the variables according to the spectral energy at each mode and frequency. Figure 53 shows the mode energy associated for six modes as a function of frequency for the entropy and pressure perturbations. The most energetic mode clearly shows several distinct frequencies, as shown in the figure.

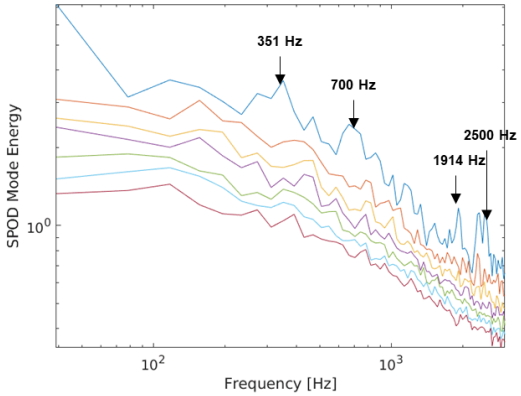


**Figure 53.** SPOD modal energy for the first six entropy–pressure modes.

Figure 54 shows the pressure and entropy mode shapes at 2500 Hz. The mid-plane view of the pressure perturbation (Figure 54a) indicates that this mode is associated with the longitudinal mode of the combustor. The mid-point of this mode is located at the dilution jet region; hence, potential exists for coupling between the dilution jets and the acoustic mode, as seen in the entropy mode shapes in Figure 54c and Figure 54d. The coupling with the longitudinal mode results in pumping of the dilution jets at 2500 Hz, thereby resulting in strong vortex formation. Figure 54c shows that this mode may also couple with the flame, thus resulting in a longitudinal mode within the flame shear layer.

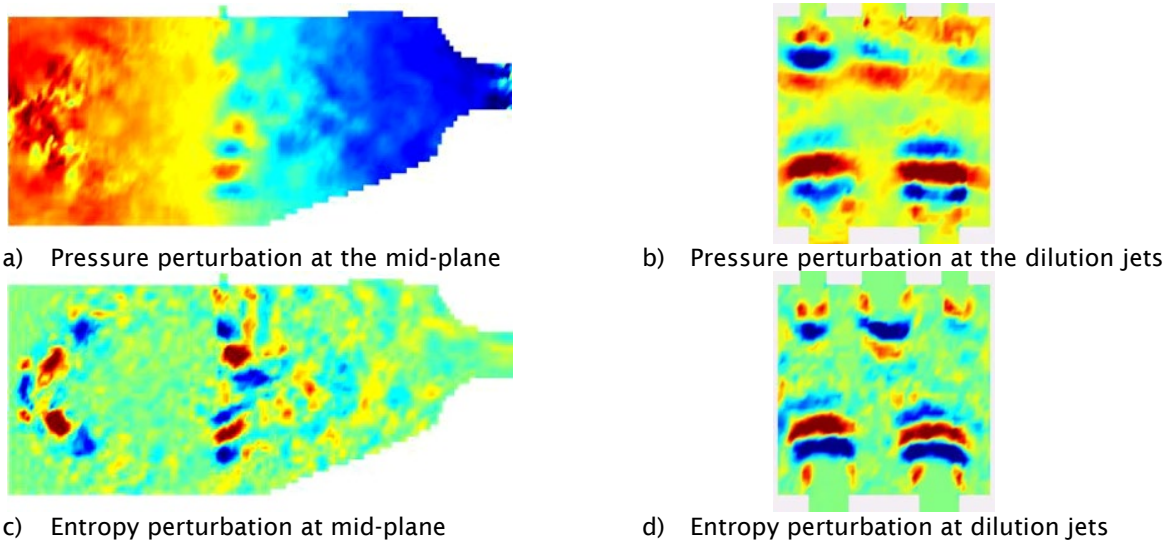

a) Pressure perturbation at the mid-plane

b) Pressure perturbation at the dilution jets

c) Entropy perturbation at mid-plane

d) Entropy perturbation at dilution jets

**Figure 54.** Snapshots of pressure and entropy mode shapes at 2500 Hz at one time instance.

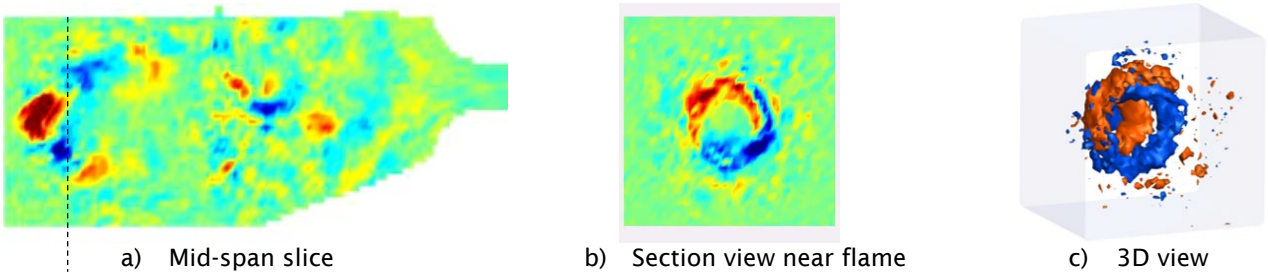

a) Mid-span slice

b) Section view near flame

c) 3D view

**Figure 55.** Snapshots of entropy mode shape at 1914 Hz at one time instance.

Figure 55 shows snapshots of three views of entropy mode associated with 1915 Hz. Clearly, this mode represents the swirl mode of the flame, characterized by a counterclockwise motion. This mode is dependent on the swirler design and the fuel and air flow rates, and is not an acoustic mode of the combustor.

Figure 56 shows snapshots of the entropy mode at different time instances. This mode at 700 Hz is somewhat unexpected but is also observed in the unsteady acoustics measurements in the RTRC experiments, as well as in the direct and indirect noise computations from the LES flow field. The SPOD mode shapes suggest that the entropy associated with this frequency is convected from the flame to the choke region with almost no dispersion. The convection wavelength for this mode is very close to the distance from the flame to the dilution jets and from the dilution jets to the choke. The entropy generated at the flame convects to the dilution jet and is reinforced by entropy by further addition from the dilution jets.

Typically, scalar fields at a particular frequency disperse within the flow field when they convect more than two wavelengths. This finding is true for the entropy transport at frequencies larger than 700 Hz for this combustor flow field. At 700 Hz, the entropy transport from the flame to the dilution jet and the dilution jet to the choke are each almost exactly two wavelengths. Because of reinforcement at the dilution jets, the entropy at 700 Hz convects with minimal dispersion. At lower frequencies, the reinforcement at the dilution jets is absent, because the entropy inhomogeneities arrive at the dilution jets with random phasing. The noise computation shown in Figure 52 underpredicts the measurement at 700 Hz, probably because the entropy addition from the dilution jets is driven by turbulence, and hence the phasing is somewhat random. With longer simulation times, this randomness is expected to “average out” and increase the spectral level of the tone at 700 Hz.

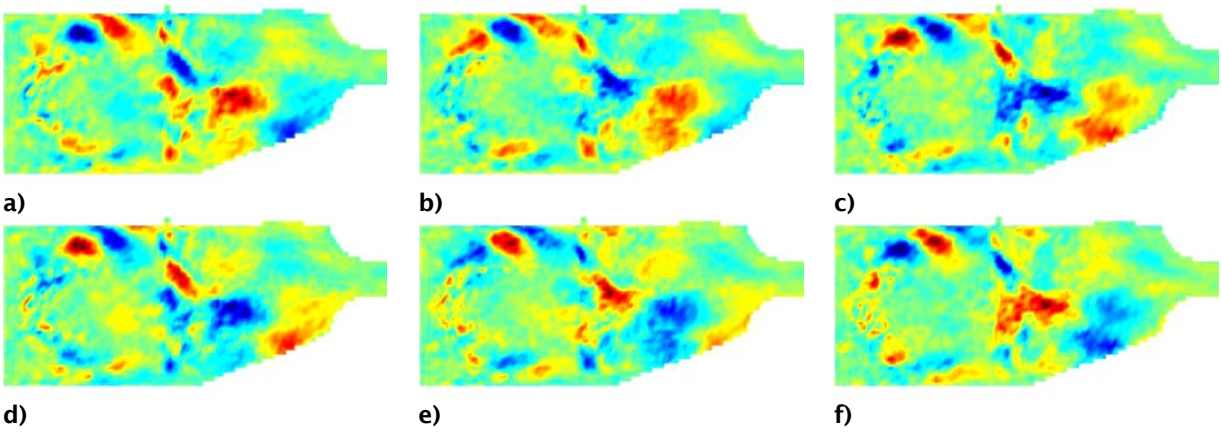


**Figure 56.** Snapshots of the entropy mode at 700 Hz at successive time intervals.

At 351 Hz, an increase in modal energy is again observed (Figure 53) because the distance from the flame to the dilution jets, and from the dilution jets to the choke, now corresponds to one wavelength of convection distance. However, the energy at the dilution jets at this frequency is not sufficiently significant and does not result in strong acoustics. Nevertheless, the frequency is visible in the acoustics computations and the RTRC experimental data.

**Turbine and nozzle wave interactions**

Tasks 1.3 and 1.4 focus on wave propagation, transmission, and reflection through the turbine section downstream of the combustion chamber. The turbine consists of two sections (high pressure and low pressure), both of which consist of multiple rows. Our studies focused on the first stage of the high-pressure turbine, which consists of a stator and a rotor. The stator is also commonly called the nozzle guide vane. In combustor rigs, such as the two rigs studied here, only a nozzle that has a similar minimum area to that of the nozzle guide vane, but otherwise has no flow turning function, is present. To distinguish between wave propagation in the real turbine and in the combustor rig nozzle, this task is split into two: Task 1.3 is concerned with the combustor nozzle analysis, and Task 1.4 is concerned with a single-stage high-pressure turbine. For both tasks, HiFi lattice Boltzmann method (LBM) simulations are conducted, and existing ROMs are revisited. Where applicable, corrections to the existing ROMs are proposed, on the basis of the learning from the LBM results. The existing ROM for the turbine is the actuator disk theory (ADT) by Cumpsty and Marble. Most of the work in Year 3 focused on turbine modeling and improvements to the ADT ROM; details are reported herein.

***Turbine interaction modeling: direct noise:*** This task focuses on simulations of a high-pressure public-domain turbine rig from the Polytechnic University of Milan and the German Aerospace Center to investigate direct and indirect noise propagation through a representative high-pressure turbine stage. A comprehensive set of HiFi LBM simulations was performed in Years 1 and 2 for high-subsonic and transonic turbine flow conditions and was successfully validated against experimental data from the German Aerospace Center. The sound power reflection coefficient and transmission coefficient agreed well between the simulation and experiment. The remaining portion of the sound power ($1 - R - T$), where $R$ is the reflection, and $T$ is the transmission), which is neither reflected nor transmitted, was found to be approximately 60% of the total sound power. We hypothesized that this portion of the power is related to sound dissipation caused by the conversion of acoustic energy into shed vorticity from the blade and vane trailing edges and other sharp geometrical features. A comparison to ADT indicated that the theory overpredicted the transmitted sound, because it does not account for such sound dissipation effects. Various simulations were performed in Year 2 to demonstrate that a large amount of the sound power is dissipated in the turbine.

In Year 3, the focus was on a detailed analysis of the mechanism of sound dissipation and finding a ROM correction term to account for these effects. The additional analysis focused on the wake region of the stator row, as shown in Figure 57. Study of the flow field downstream of the vane trailing edge, in the presence of acoustic excitation, clearly indicated that, in addition to an oscillating pressure field at the acoustic forcing frequency, the vorticity field also displays oscillations at the same frequency. This finding underscores that vorticity generation indeed occurs in the vicinity of the trailing edges.

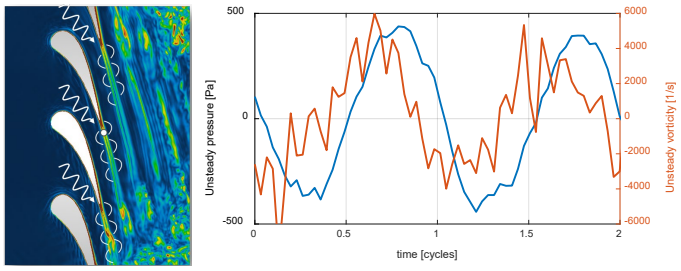


**Figure 57.** Cyclic vorticity shedding in the wake of the stator vanes in response to the acoustic forcing.

To quantitatively capture the sound dissipation effect, we applied the theory of Howe to the current LBM data. The model is based on a splitter plate in a duct with uniform mean flow Mach number *M* on both sides, and is based on the assumption that sound approaches the trailing edge with a phase difference in Θ between the pressure side and suction side of the plate. Sound diffraction at the trailing edge is modeled with application of the Kutta condition to determine the strength of the shed vorticity. The phase therefore determines how efficiently acoustic energy is converted into vorticity generation. The solution of this diffraction problem is greatly simplified for a plane wave, which is considered here. For double-sided forcing, the dissipated sound power $\Pi_D$ for an incident plane wave on both sides of the plate ($2\Pi_0$) is given by the following solution that includes only the Mach number and phase angle as parameters controlling the amount of sound power dissipation:

$$\frac{\Pi_D}{2\Pi_0} = 1 - \left(\frac{1-M}{1+M}\right)^2 \sin^2\left(\frac{\Theta}{2}\right) - \cos^2\left(\frac{\Theta}{2}\right) \tag{38}$$

This equation has the following solutions:

$\Theta = 0°$: $\frac{\Pi_D}{2\Pi_0} = 0$ (no dissipation)

$\Theta = 90°$: $\frac{\Pi_D}{2\Pi_0} = \frac{2M}{(1+M)^2}$ (same as single-sided forcing)

$\Theta = 180°$: $\frac{\Pi_D}{2\Pi_0} = \frac{4M}{(1+M)^2}$ (maximum dissipation)

Figure 58 shows the bandpass-filtered pressure field from an LBM solution with 600-Hz forcing. The results indicate that, despite the plane wave forcing, the wavefront shows a phase difference ($\theta \neq 0°$) between the pressure and suction side near the trailing edge. This aspect is further visualized through the time history of two monitor points on opposing sides of the vane and near the trailing edge. The phase angle from the time signal is calculated to be ~80˚, which falls roughly in the middle of the expected dissipation values according to Eq. (38).

Applying Eq. (38) to the simulation data (Figure 59) shows that very good agreement (except at $M = 0$, where the model is not applicable) between theory and LBM can be achieved by assuming a phase angle of 95˚. Using the value of 80˚ obtained from the spot check in the simulation would underpredict the amount of dissipation. For *M*, the time-averaged absolute Mach number is calculated near the exit of the vane row. In reality, this model is a simplification of the actual shedding mechanism, which does not include the effect of the turbulent boundary layers on both sides of the vane/plate and the associated sheared wake flow. In addition, the calculated phase angles may show some sensitivity with respect to the precise location in the vicinity of the trailing edge. Therefore, in the following, the phase angle is considered to be a tuning parameter that can be used to control the amount of dissipation to better match the simulation data and also provides a way to parametrically study the impact of dissipation on overall noise transmission through the turbine and into the far field, when used within the noise prediction toolchain.

ADT by Cumpsty and Marble is applied for both turbine operating conditions, for that stator alone; the comparison is shown in Figure 60. The amplitude of the reflected pressure is predicted well by the theory for all frequencies considered. As expected, the transmitted sound is overpredicted, because ADT does not account for sound dissipation effects. A

correction to the transmitted acoustic pressure from ADT is proposed, wherein the correction is applied with respect to the transmitted sound power in the following form:

$$\Pi_T = \Pi_{T,ADT} - \Pi_D \quad \Rightarrow \quad \frac{\Pi_T}{2\Pi_0} = \frac{\Pi_{T,ADT}}{2\Pi_0}\left(1 - \frac{\Pi_D}{\Pi_{T,ADT}}\right)$$

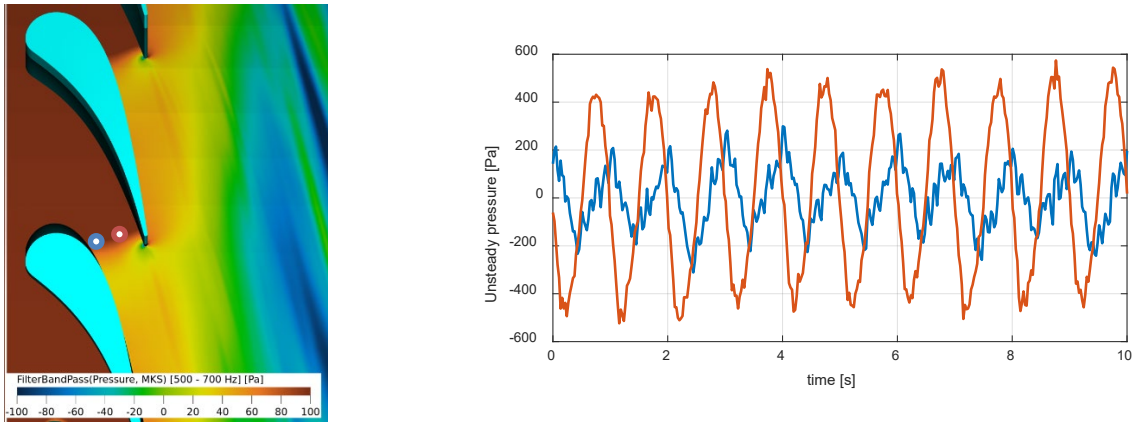


**Figure 58.** Pressure at the forcing frequency and phase angle between two monitor points near the trailing edge.

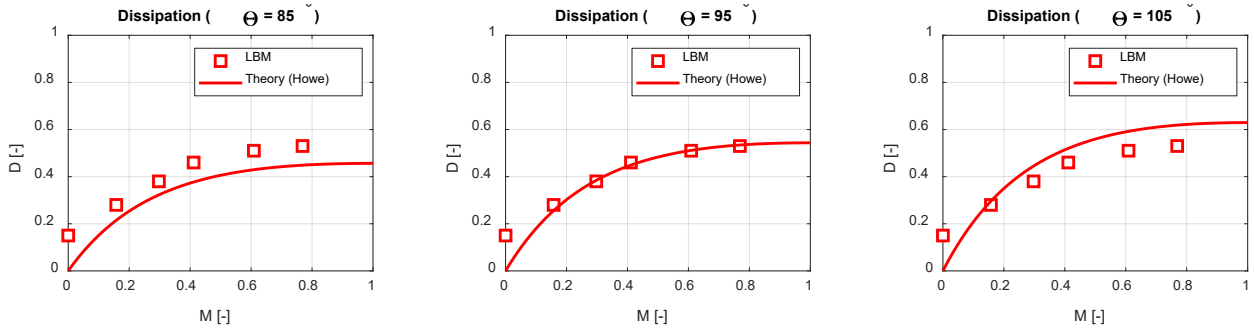


**Figure 59.** Application of the splitter plate dissipation model to LBM data for different phase angles Θ.

The acoustic pressure amplitude ($p \propto \sqrt{\Pi}$) downstream of the actuator disk can be calculated through multiplication by the following correction term $C_p$:

$$C_p = \frac{p^+_{2,C}}{p^+_{2,ADT}} = \sqrt{1 - \frac{\Pi_D}{\Pi_{T,ADT}}} = \sqrt{1 - \frac{4M}{(1+M)^2}\sin^2\left(\frac{\Theta}{2}\right)} \tag{39}$$

Of note, the dissipation correction is assumed to be applied with respect to the predicted transmitted sound power based on ADT, not the incident sound power. With this correction term in place, the level of agreement between LBM and ROM significantly improves, as shown in Figure 60.

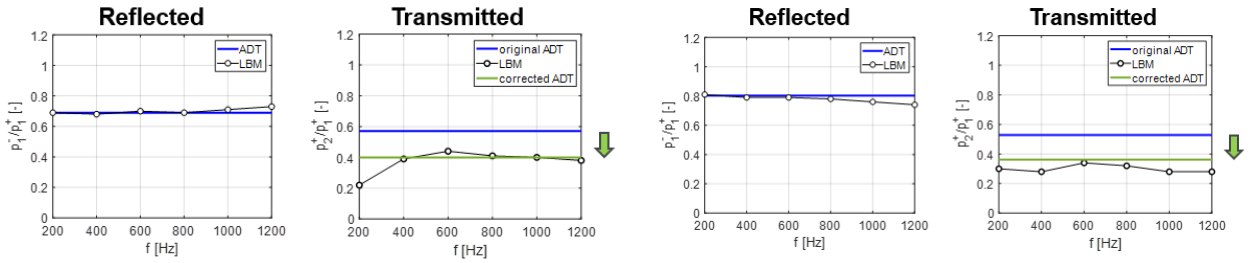


(a) High subsonic flow (OP3) (b) Transonic flow (OP1)

**Figure 60.** ADT applied to the stator row for various operating conditions.

A comparison of ADT to LBM is also performed for other Mach numbers. Figure 61 shows the predicted reflection and transmission pressure amplitudes for the stator row. The highest two Mach conditions correspond to OP3 and OP1 of the turbine stage. For this higher Mach regime, which is representative of a high-pressure turbine operating condition, ADT and LBM agree very well in terms of reflection and in terms of transmission, when the correction term is enabled. This observation is equivalent to that in Figure 60. As the Mach number through the stator is reduced, ADT and LBM begin to deviate, even for the reflection coefficient: ADT predicts lower reflection and higher transmission. Because these lower Mach numbers are not relevant to realistic operating conditions, they are not further analyzed here.

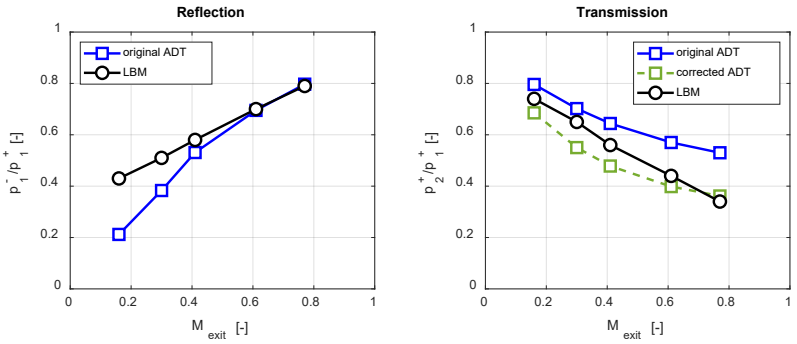


**Figure 61.** ADT applied to the stator row for different Mach numbers, with and without dissipation correction.

We next focus on the high Mach regime. The dissipation correction can be applied to the rotor as well. A sample calculation is provided below, to demonstrate that this approach yields correct values. The rotor exit velocity must be known in the relative frame of reference, to calculate the Mach number *M* for Eq. (38). This value (if the exit flow angle is assumed to be 0) is simply given by:

$$\mathrm{M}_R = \sqrt{\mathrm{M}^2 + \left(\frac{2\pi r n}{c_0}\right)^2}$$

where *M* is the rotor exit Mach number in the absolute frame, $c_o$ is the speed of sound, *r* is the rotor radius, and *n* is the rotor rotational speed. For simplicity, the rotational speed at the rotor midspan is used. The total dissipation for the stator and rotor is then given by the sum of the stator dissipation and the transmitted-power "weighted" rotor dissipation:

$$D_{S+R} = D_S + D_R = D_S + T_S\left[1 - \left(\frac{1-M_R}{1+M_R}\right)^2 \sin^2\left(\frac{\Theta}{2}\right) - \cos^2\left(\frac{\Theta}{2}\right)\right] \tag{40}$$

Table 3 summarizes the calculation results with Eq. (40) for both turbine operating conditions. In both cases, the rotor dissipation is on the order of 50% and hence is similar to the contribution from the stator. However, because less than 20% of the original sound power is transmitted through the stator ($T_S$), the added dissipation of the rotor is less than 10%; consequently, the total sound power dissipation coefficient in both cases is on the order of 60%, in agreement with the dissipation values determined directly from the LBM simulation of stator plus rotor.

**Table 3.** Prediction of turbine stage sound dissipation.

| | $D_S$ | $T_S$ | $M_R$ | $D_R$ | $D_S + D_R$ (Eq. (40)) | $D_S + D_R$ (LBM) |
|---|---|---|---|---|---|---|
| OP3 | 0.51 | 0.12 | 0.42 | 0.45 | 0.57 | 0.61 |
| OP1 | 0.53 | 0.19 | 0.68 | 0.52 | 0.62 | 0.61 |

In conclusion, Eq. (39) can be applied to ADT to correct the transmitted pressure amplitudes. This equation must be applied for each row and requires the exit Mach number for each stage row in the respective reference frame of the stage. The phase angle $\Theta$ can be set for each row separately. In the present cases, a single value of $\Theta = 95°$ was found to be sufficient.

***Turbine interaction modeling: indirect noise:*** Beyond investigating the direct noise propagation through the turbine, we performed additional simulation work to investigate indirect noise generation and transmission through the turbine stage, in the form of injected unsteady temperature perturbations upstream of the turbine. High-fidelity simulations were performed, wherein the acoustic driver upstream of the turbine was replaced with circumferentially positioned injection ports. This setup, shown in Figure 62, closely mimics the experimental setup of the Polytechnic University of Milan (PoliMi) and the German Aerospace Center (DLR) rig. Each injector was installed at 70% span with 1/3 pitch offset in the circumferential direction, as measured from the vane leading edge toward the pressure side. This setup was already considered in Years 1 and 2 but was revisited in Year 3 for further simulation work and more in-depth validation with published data that were not available until Year 3 of this program.

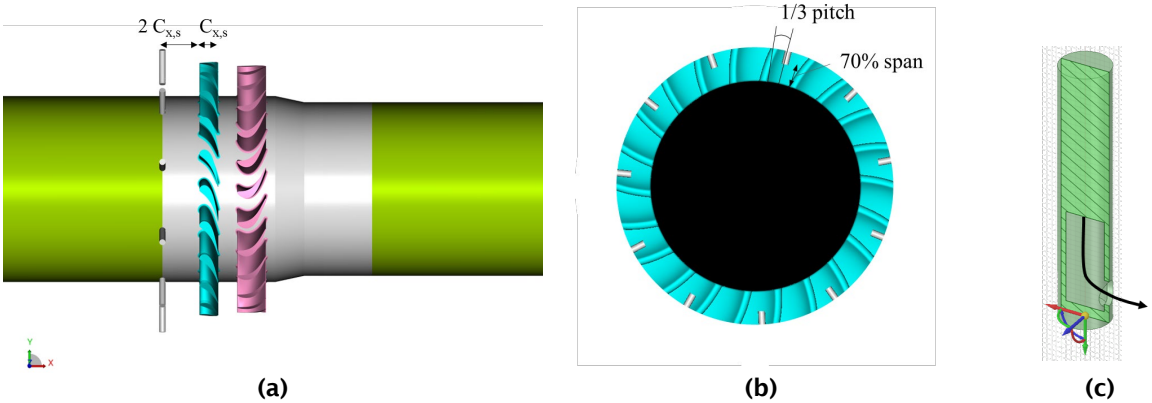


**Figure 62.** Simulation domain details for indirect noise studies, using 11 circumferentially arranged injectors for entropy wave generation. (a) Side view, (b) front view, and (c) cut-away view of a single injector.

The simulations were run with a constant elevated injection temperature first to create hot streaks, and then adjusted to provide a sinusoidal time variation with a period of $f$ = 90, 250, or 400 Hz. Entropy wave generation was accomplished through time-harmonic variation in the injection temperature, while the total injection pressure remained constant. The peak-to-peak temperature is given by $\Delta T_s = T_{s,streak} - T_{s,ref}$, where $T_{s,ref}$ is the reference "cold" temperature in the bulk flow, and $T_{s,streak}$ is the maximum "streak" temperature of the injected air. The simulations were first run with a constant elevated injection temperature $T_{s,streak}$ and then adjusted to provide the following time variation:

$$T_s(t) = 0.5\left(T_{s,streak} + T_{s,ref}\right) + 0.5\left(T_{s,streak} - T_{s,ref}\right)\cos\left(2\pi f_{source}\right) \tag{41}$$

Three injection amplitudes were considered (Figure 63), the lowest corresponding to the value used in the DLR experiment.

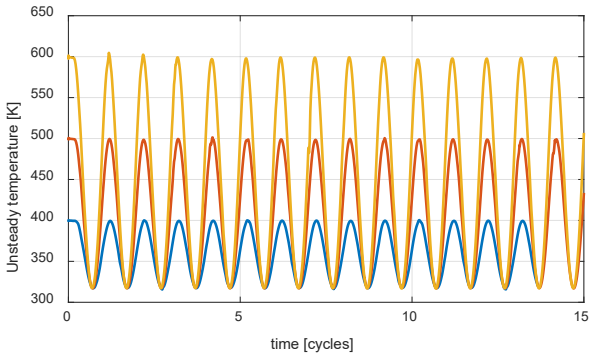


**Figure 63.** Temperature amplitudes of the injected entropy waves for three injection ratios: $T_{inj}/T_{ref}$ = 1.26, 1.58, or 1.89, where $T_{ref}$ = 320.1 K.

The unsteady temperature field interacts with the turbine and creates acoustic waves as the temperature hotspots convect through the accelerated non-uniform turbine flow field. Figure 64 shows the total temperature field during one injection cycle.

The simulations were subsequently repeated for other forcing amplitudes. According to ADT, the noise generation from the entropy wave interaction with the turbine should be frequency independent. The following discussion is focused on the 250-Hz simulation results, for two reasons: (a) the numerical buffer regions was not designed for the 90-Hz forcing wavelength and includes large reflection from the domain exit, and (b) the first non-planar cut-on mode occurs around 308 Hz (upstream) and 318 Hz (downstream). The 400-Hz excitation includes higher-order modes that are not representative of the test setup.

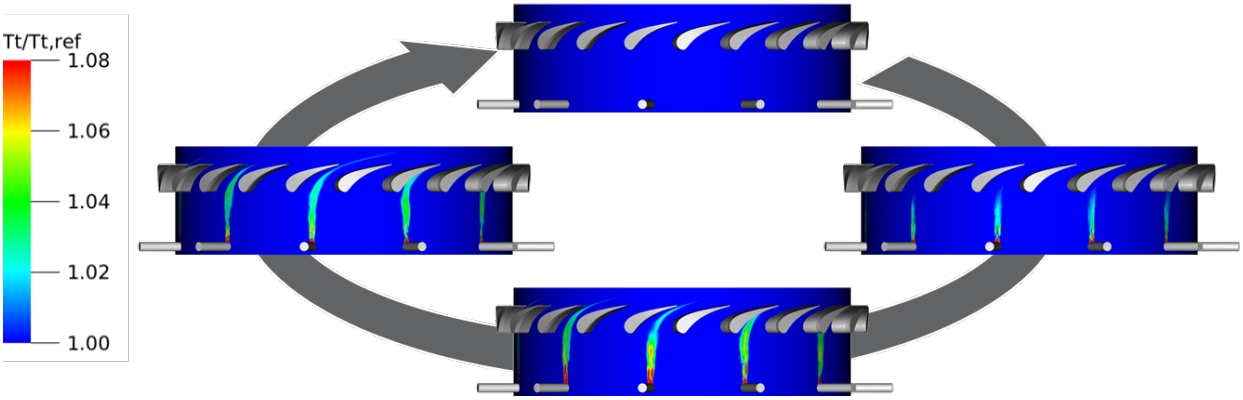


**Figure 64.** Entropy wave injection cycle (rotor blades not shown) for high-subsonic turbine flow.

The DLR experiment was conducted at 90 Hz. The noise data published by Knobloch et al. do not contain absolute sound power levels but only relative levels with respect to cold injection. However, Pinelli et al. have recently published simulation data including an absolute value for the downstream noise for the 90-Hz forcing. No upstream power data were included. Here, the 250-Hz plane-wave forcing case was post-processed, and the upstream and downstream propagating sound power was calculated via modal decomposition of the pressure. The results are summarized in Table 4.

**Table 4.** Predicted entropy wave sound power levels for $T_{inj}/T_{ref}$ = 1.26 compared with data from the literature.

| | RTRC (250 Hz) | | | | Pinelli et al. (116.6 Hz) | DLR EXP (90 Hz) |
|---|---|---|---|---|---|---|
| | Plane 1 | Plane 2 | Plane 3 | Plane 4 | | |
| Upstream | 105.1 dB | 105.1 dB | 105.1 dB | 105.1 dB | 100.3 dB | – |
| Downstream | 96.6 dB | 97.6 dB | 98.3 dB | 98.4 dB | 98.0 dB | 98.7 dB |

The major observations are as follows:

- The forcing frequency differed in all three cases (RTRC, Pinelli et al., and DLR experiment). However, all cases involved only plane waves, and differences due to frequency should be marginal.
- The upstream sound power is higher than the downstream noise, in agreement with the predictions by Pinelli et al. and the acoustic field visualization shown in Figure 65.
- The upstream sound power is insensitive to the data extraction location, and the values are 4.8 dB higher than the values reported by Pinelli et al.
- The downstream sound power levels are sensitive to the data extraction location, with values slightly increasing toward the downstream direction. This finding is likely to be related to the presence of hydrodynamic fluctuations.
- The downstream power levels are consistent overall with the experimental data and the predictions by Pinelli et al.

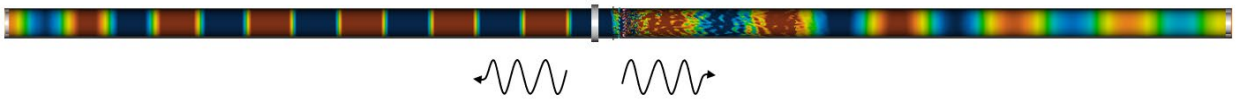

**Figure 65.** Visualization of the upstream- and downstream-propagating acoustic pressure because of entropy wave interaction with the turbine stage.

Notably, because of the nature of the entropy wave generation by flow injectors, a certain amount of vorticity wave generation is inherently included. Although the injection temperature was carefully controlled in the present simulations, the amount of vorticity wave generation has not been examined separately. Relatedly, Pinelli et al. did not simulate the injectors upstream of the stator vanes explicitly but instead injected the measured temperature profile from the experiment.

In summary, the direct noise validation cases were well defined, and the agreement between experimental findings and LBM simulations was very good. Because of the nature of the entropy wave generation in the experiments, no comparable extensive dataset is available for validation. The predicted indirect noise levels downstream of the turbine stage for the case considered here are consistent with the reported literature data.

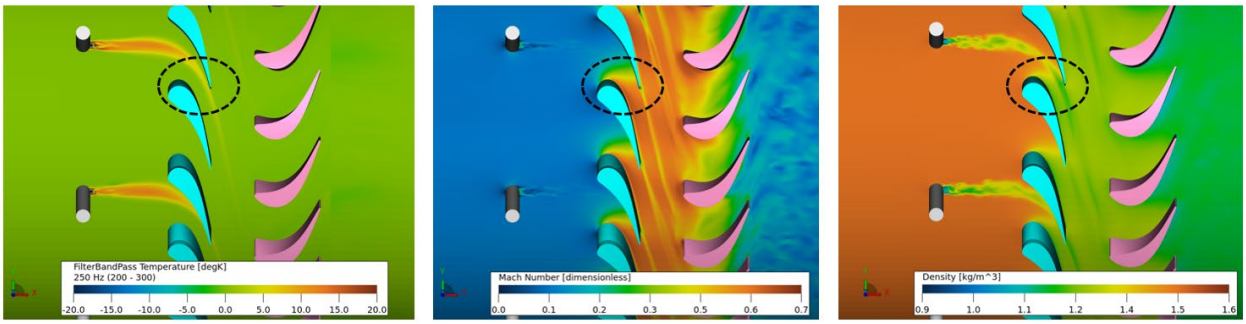


**Figure 66.** Visualization of important flow regions for noise generation: the entropy wave field (left), the non-unform mean flow inside the vane passage (middle), and the unsteady density field (right).

In general, two main mechanisms are responsible for the sound generation: (a) strong local flow acceleration in regions of high-velocity gradients (monopole source) and (b) unsteady drag exerted on the vanes/blades through the density fluctuations (drag force). The first mechanism is negligible for low Mach numbers but very important for the encountered high-Mach-number flows inside the turbine stage, in regions with strong local flow acceleration. The second mechanism is particularly pronounced when the entropy wave is close to the leading edge or trailing edge. Qualitatively, the important flow regions and quantities for the turbine simulations are shown in Figure 66.

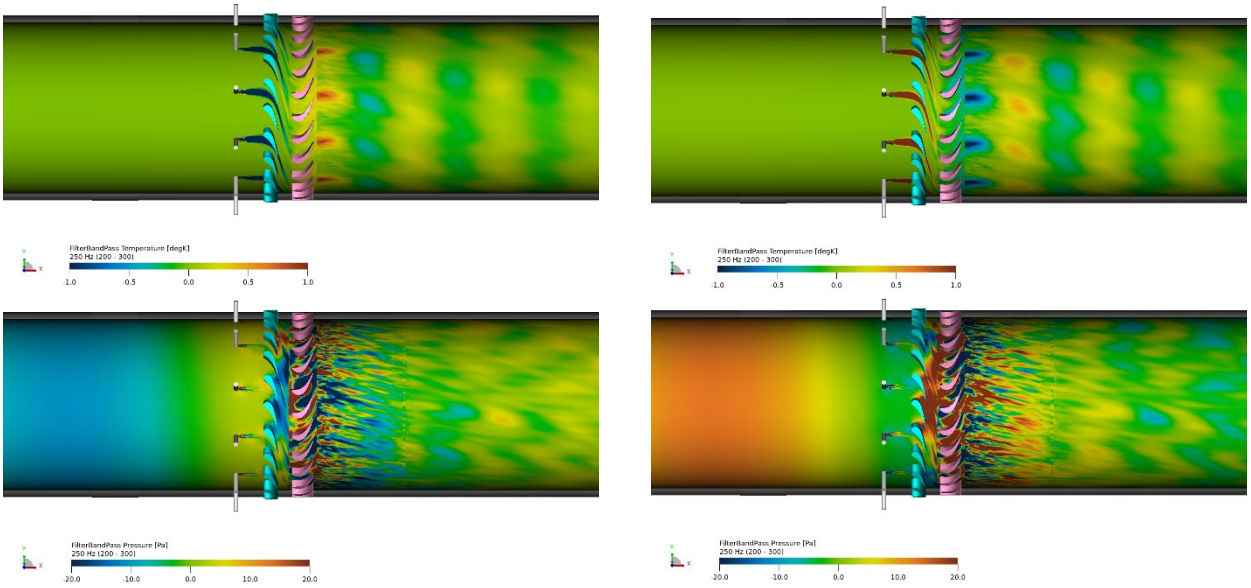


(a) Time $t_1$ (b) Time $t_2$

**Figure 67.** Visualization of entropy wave interaction with the stator vane passage (top) and resulting acoustic pressure generation (bottom), for two time instances in the injection cycle.

Snapshots of the temperature and pressure fields for different time instances during the injection cycle are shown in Figure 66. A strong acoustic pressure field is clearly generated in the interstage passage between the stator and rotor when the entropy wave travels through the stator vane passage. The resulting upstream propagating acoustic wave is visible, as well as the highly dispersed entropy waves downstream of the rotor. The downstream propagating sound is not clearly visible, because of the presence of strong hydrodynamic fluctuations downstream of the rotor. As shown previously in Figure 65, an acoustic wave further downstream of the rotor is clearly identifiable. After the sound is generated, it travels upstream and downstream. In the latter case, the sound interacts with the rotor and creates additional back-reflections within the stator-rotor passage. In addition, vorticity waves are generated at the stator trailing edges and can result in additional noise through interacting with the rotor's leading edge.

Pinelli et al. have shown that the injector placement relative to the stator vane (i.e., the clocking) plays a role of the upstream generated noise: levels are 2–4 dB higher for injections in which direct impingement on the vane leading or trailing edge is achieved than for injections in which the entropy wave is centered between two vane passages. For the downstream generated noise, however, the sound power levels were found to be largely independent of the injector clocking relative to the stator vanes.

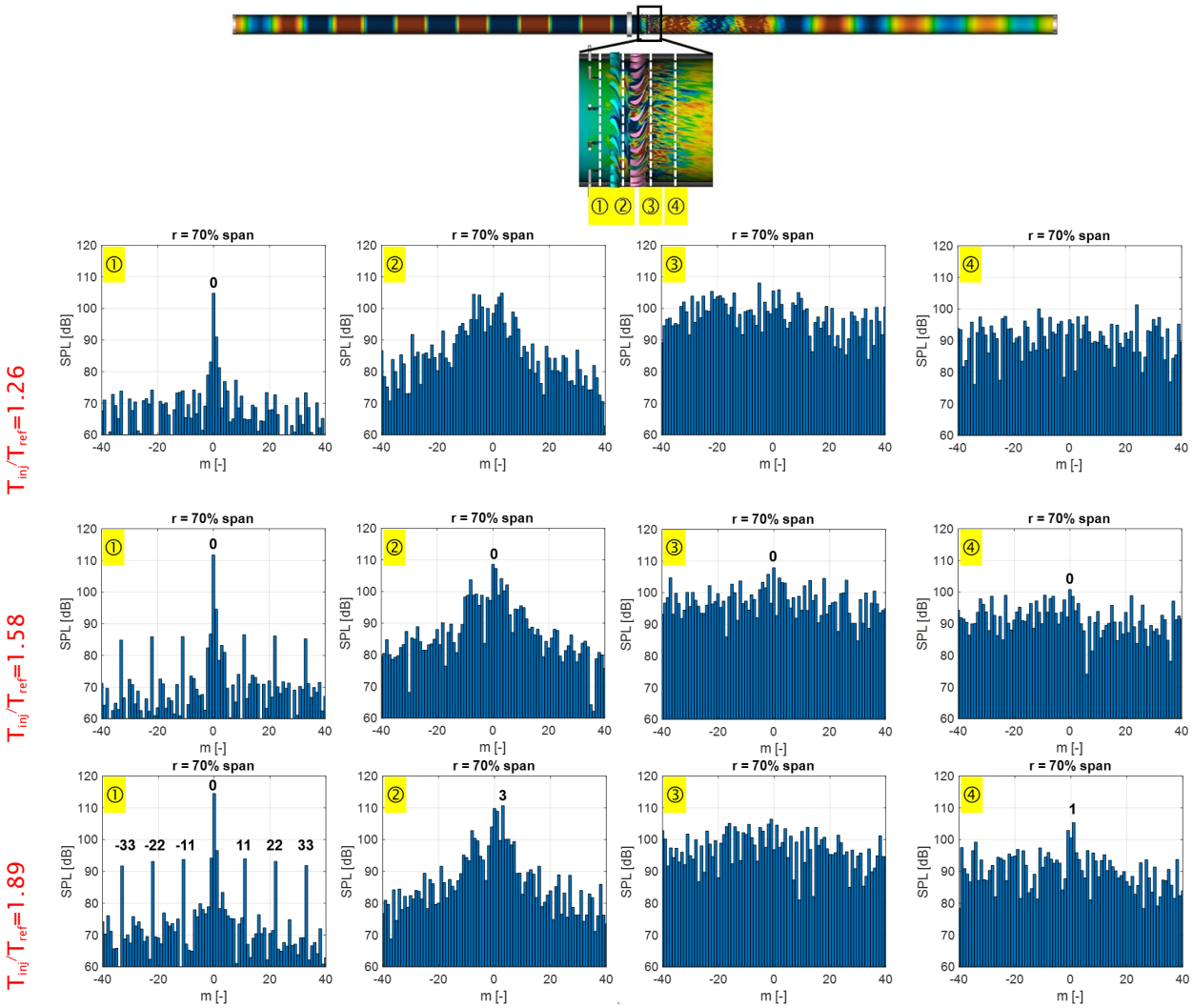


**Figure 68.** Modal analysis of the pressure field at $f$ = 250 Hz, at different cut planes.

A modal analysis of the pressure field at different cut planes in the flow field is shown in Figure 68 for all three injection amplitudes. Upstream of the stator, at plane 1, a single dominant plane wave mode ($m$ = 0) is observed, whereas the injector-related direct pressure field ($m$ = ±11, ±22, ±33, …) is at least 20 dB lower. In the interstage region (plane 2), a mixture of low-order modes is detected. All these modes are cut off. Whereas a strong $m$ = 1 mode remains visible on plane 4 for the highest injection rate case, it decays, and the $m$ = 0 mode is the remaining acoustic mode downstream that carries sound power. The modal amplitudes downstream are significantly lower than those upstream. The multitude of modes in the downstream section is due to the presence of turbulent flow.

According to theory, the sound power should scale as $\propto \Delta T^2$, which provides a good approximation of the simulation cases for both upstream and downstream indirect noise, as plotted in Figure 69.

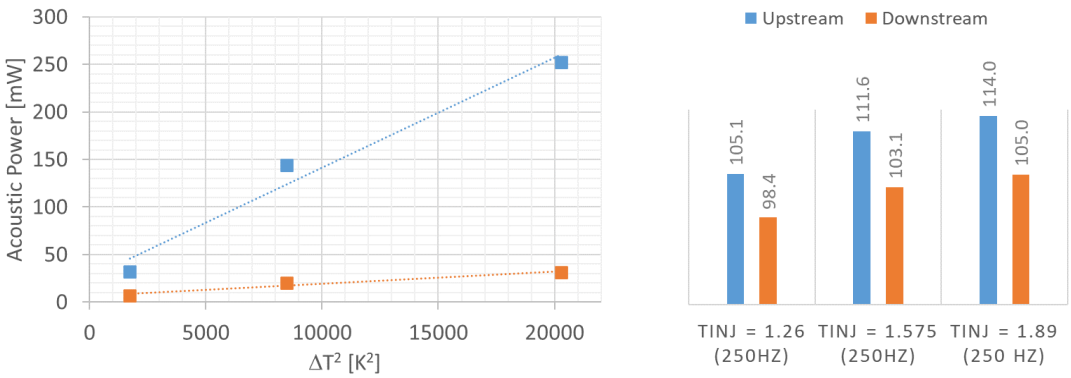


**Figure 69.** Sound power scaling for the simulated indirect noise case. Left: linear; right: d**B.**

For the highest injection case, a phased injection simulation was also run, wherein the injection by injector $i$ is phase-delayed by a time delta corresponding to $n_{inj}/f_{forcing} \cdot i$, where $n_{inj}$ is the number of total injectors, and $f_{forcing}$ is the forcing frequency. Thus, a continuous circumferentially traveling injection phase pattern is created. The acoustic field is described by a very strong $m = 1$ mode in the near field (Figure 70). Upstream (on plane 1) it is of similar magnitude as the plane-wave mode with synchronized forcing, whereas in the interstage (plane 2) and downstream (plane 4), this $m = 1$ mode remains very high in amplitude—higher than any modes created with the plane wave forcing approach. However, as this mode is cut off, it decays exponentially and does not contribute to the radiated sound power.

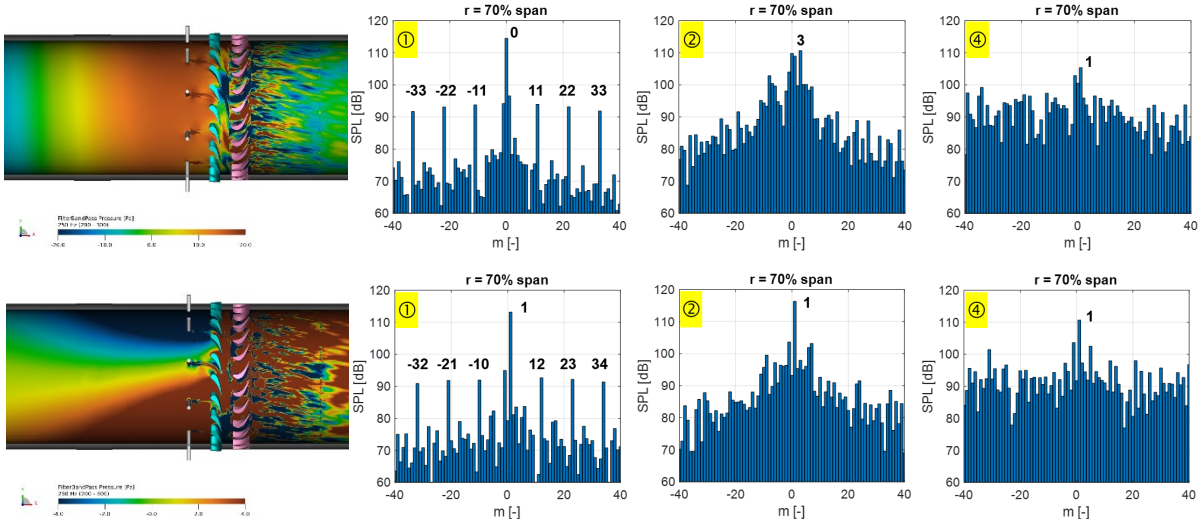


**Figure 70.** Top: Pressure modes for simultaneous forcing ($m = 0$); bottom: pressure modes for phased forcing ($m = 1$) for different cut planes. Plane 1: upstream of stator; plane 2: interstage; plane 3: downstream of rotor.

The acoustic field far upstream and downstream is characterized by the plane wave mode alone. This mode remains created with the phased injection case, but its amplitude is substantially reduced (Figure 71). The calculated sound power level is reduced by more than 15 dB. The phased injection creates higher sound power downstream than upstream. The simulation cases illustrates that even cut-off modes can contribute to the overall sound power, via scattering into propagating modes.

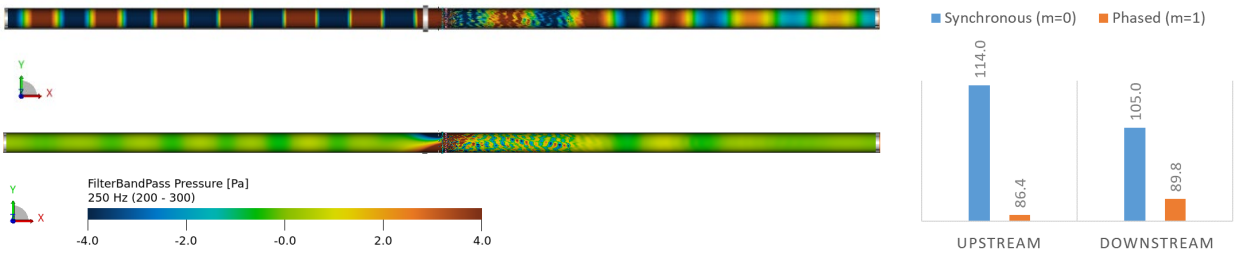


**Figure 71.** Left: visualization of the upstream- and downstream-propagating acoustic pressure for an entropy wave with $T_{inj}/T_{ref}$ = 1.89, for different forcing types. Top: synchronous injection, creating an $m$ = 0 mode. Bottom: Phased injection, creating an $m$ = 1 mode. Right: sound power levels.

As the wave is transported through the turbine stage, its amplitude is drastically reduced, even for the relatively low frequency of 250 Hz considered here, for two potential reasons: (a) shear dispersion due to the nonuniform mean flow and (b) dissipation by the turbulent flow. For combustors, the second effect is found to be negligible; for turbines, this effect has yet to be quantified. Figure 72 shows how the wave amplitude of the localized entropy waves is reduced by ~75% across each vane/blade row.

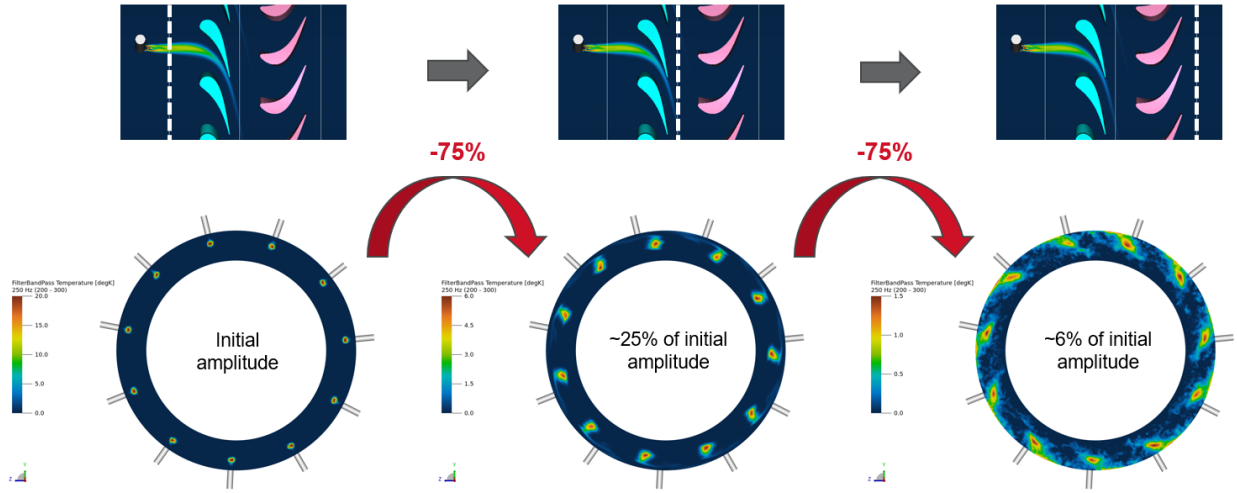


**Figure 72.** Entropy wave amplitude change during transport through the turbine.

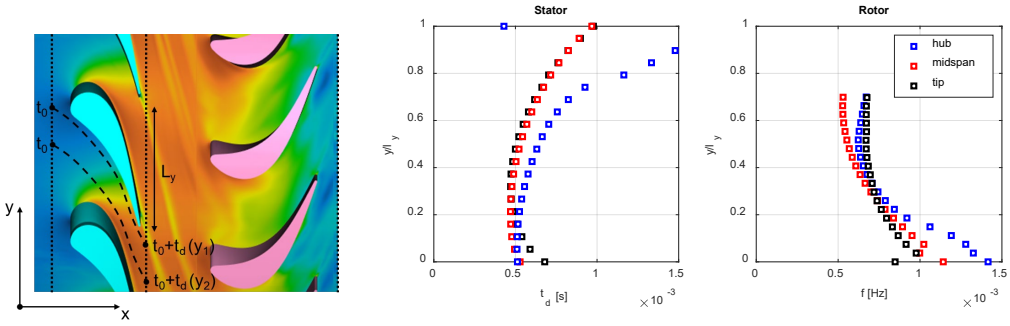


**Figure 73.** Time delay for entropy waves traveling along different streamlines as they pass through the vane and blade passages.

The dispersion effect can be calculated through a streamline analysis of the mean flow field for stator and rotor. This calculation is performed for condition OP3 by seeding 20 × 20 streamlines from the inlet to the outlet of each row. The time delay is then calculated along each streamline, so that a time delay profile for the entropy waves between the vanes can be calculated. Figure 73 illustrates this process.

These profiles can now be integrated across the vane/blade pitch, to obtain the 2D transfer function for each radial section.

$$TF(r) = \left| \frac{1}{L_\theta} \int_0^{L_\theta} e^{i\omega t_d(r,\theta)} d\theta \right| \tag{42}$$

Although the time delay profiles are quite different for each radial slice, the transfer function is relatively less sensitive to radial section. The spanwise average 1D transfer function is then given by:

$$TF = \left| \frac{1}{L_r L_\theta} \int_0^{L_\theta} \int_{r_h}^{r_t} e^{i\omega t_d(r,\theta)} dr d\theta \right| \tag{43}$$

The results are plotted for the stator, the rotor, and the combination of both in Figure 74. Despite the different flow profiles in the stator and rotor, the transfer functions are very similar. The combined transfer function is the product of both individual transfer functions, and shows substantial amplitude reduction with increasing frequency.

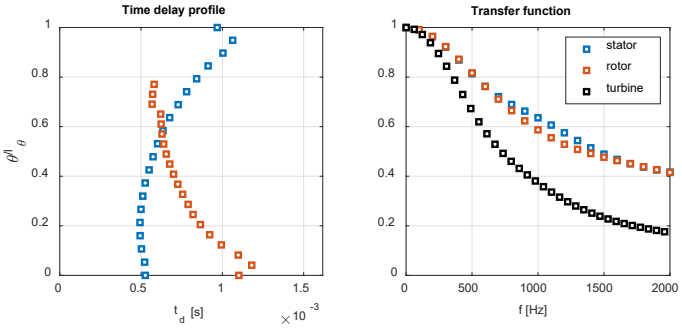


**Figure 74.** Average time delay profiles across the flow passage (left) and corresponding transfer functions.

On the basis of the work of Bauerheim et al., a generic velocity profile can be introduced and integrated to determine the shear dispersion behavior. This process eliminates the need for a mean flow solution, and the model can be calibrated for each turbine design by using such generic velocity profiles. The generic velocity profile is given by:

$$\upsilon_x = \left( \frac{\theta}{L_\theta} \right)^{\eta/n_g} \left( 1 - \frac{\theta}{L_\theta} \right)^{(1-\eta)/n_g} \tag{44}$$

where $\eta$ describes the asymmetry of the velocity profile, and $n_g$ describes the profile shape. This profile can then be used to calculate the time delay as follows:

$$t_d = \frac{L_x}{\upsilon_{x,0}} \frac{\eta^{\eta/n_g} (1-\eta)^{(1-\eta)/n_g}}{\upsilon_x} \tag{45}$$

By selection of $\eta$ and $n_g$, the profile can be adjusted to match the simulation data. This process is demonstrated for both stator and rotor profiles. As shown in Figure 75, the simulation data can be matched quite well. One challenge is that the velocity profiles vary along the span, with different fitting parameters, so no single set is adequate.

However, as indicated in Figure 74, the transfer function itself (which is calculated from the velocity profiles) is not very sensitive to the model parameters. To match the 1D ADT assumption, a single model parameter fit is used to match the data in Figure 74. Through that approach, Figure 74 can be updated with the model, which is shown in Figure 75 and represents the simulation data quite well. The final parameters are $\eta = 0.15$ and $n_g = 1.5$ for the stator, and $\eta = 0.7$ and $n_g = 1.65$ for the rotor.

Finally, a sensitivity study of the model is provided in Figure 77. A stronger asymmetric velocity profile and a more parabolic velocity profile (higher nonuniformity) have the strongest impact on the transfer function. As expected, the impact is most pronounced at higher frequencies. In the absence of any data, these models could be used to bound the problem (worst and best case).

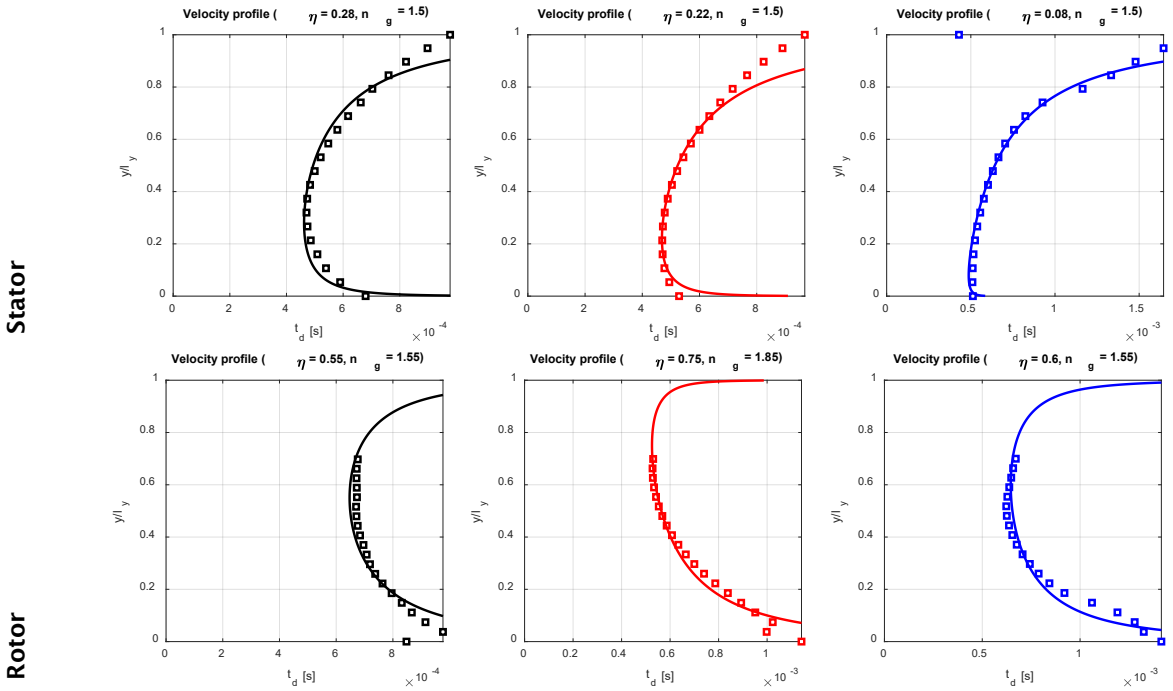


**Figure 75.** Time delay profiles as predicted by the model.

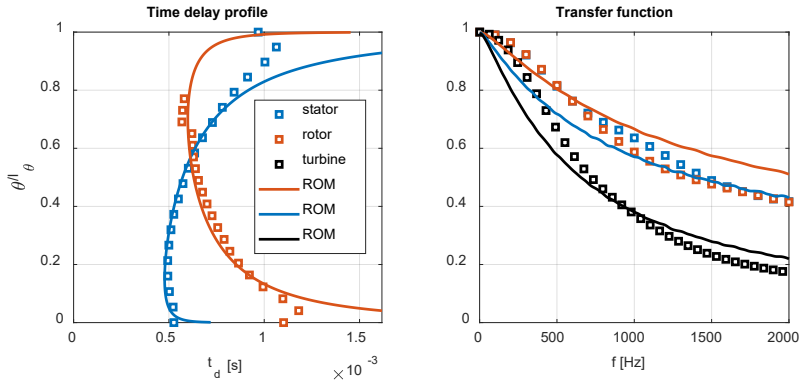


**Figure 76.** Average time delay profiles and transfer function using the ROM.

A correction term can now be added to ADT, to account for shear wave dispersion for each row. In its original form, ADT assumes that the entropy wave $\sigma$ remains constant across each row. On the basis of the parametrized velocity profile, the correction term for each row is given by:

$$\sigma_2 = C_s \sigma_1$$
$$C_s = \left| \frac{1}{L_\theta} \int_0^{L_\theta} e^{i\omega t_d(\theta)} d\theta \right| \tag{46}$$

The time delay is calculated with Eqs. (44)–(45). This process is straightforward after the parameters $\eta$ and $n_g$ are defined. With use of this term, the entropy wave amplitude continues to decay as the wave convects through the different turbine stages, thus diminishing the importance of this term as an indirect noise source beyond the first few vane/blade rows.

Impact of velocity asymmetry

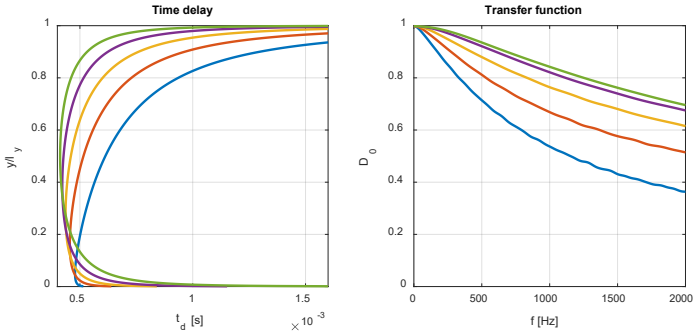


Impact of velocity profile

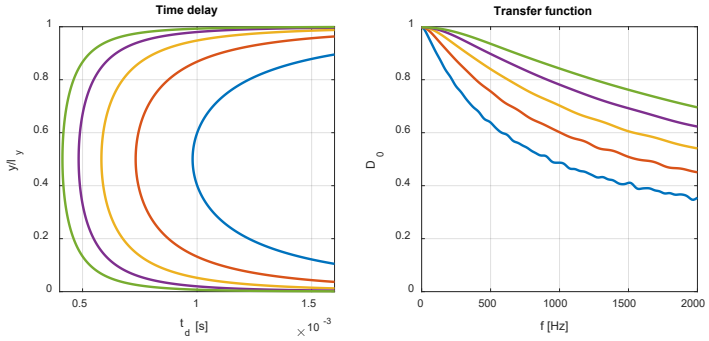


**Figure 77.** Sensitivity study of the shear dispersion model with respect to the two tuning parameters.

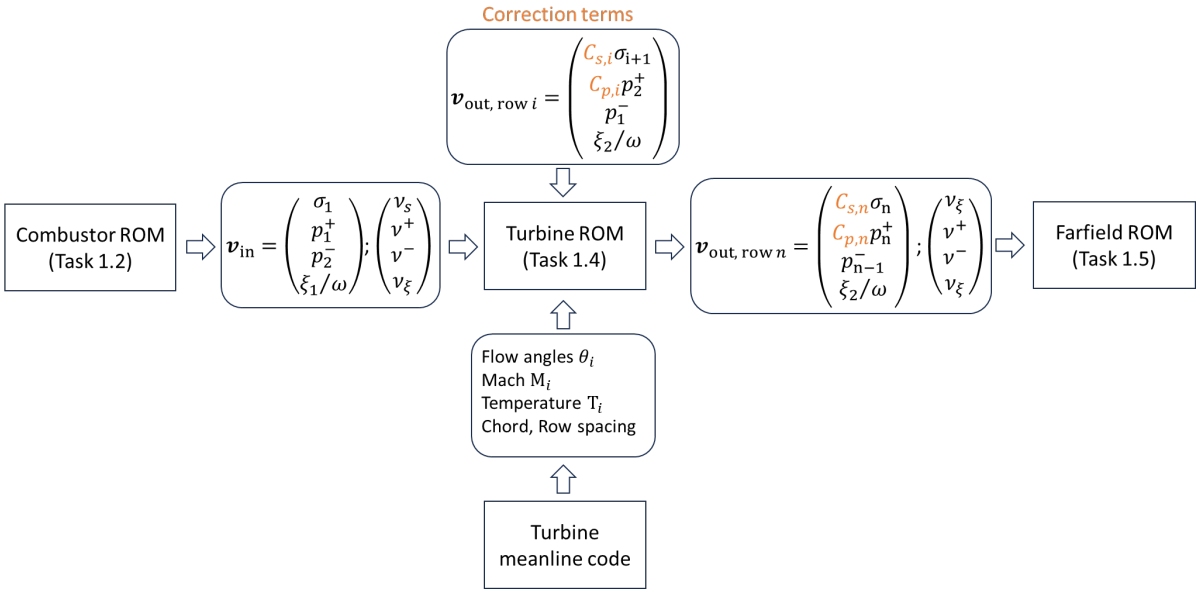


**Figure 78.** Flowchart for the turbine ROM.

In summary, two correction terms for the turbine ROM were derived and implemented. The flow chart in Figure 78 shows how the different tasks are connected and how the correction terms are implemented. The inputs and outputs of the turbine ROM are defined by the wave amplitudes for each wave type (acoustic, entropy, or vorticity) and each frequency. These values come from the combustor exit region (Task 1.2). In addition, to calculate the wave propagation through the turbine, the inlet and outlet Mach numbers are needed, as well as the inlet and outlet flow angles, and the wave angles to be considered. The first two values are typically available from a meanline solution for a given turbine design and operating condition. The wave angles, in contrast, also come from the combustor exit. Together, these quantities are used to construct the matrices to solve the ADT ROM. For multi-row applications, an additional phase-delay matrix is introduced that requires the spacing between the different rows, which is defined as the distance between the axial mid-chord locations of the rows plus the interstage gap. The turbine ROM calculates the outgoing wave amplitudes that feed into the far-field noise tool. This process is summarized in Figure 78, including where the derived corrections are applied. Of note, applying the dissipation correction only to the downstream propagation acoustic waves (not upstream) is suggested.

**Far-field noise modeling**

Task 1.5 focuses on the development of a modeling tool chain that predicts the propagation of combustion noise as it emitted from the engine core exit to the far field. During Years 1 and 2, a HiFi far-field propagation modeling process with ACTRAN/DGM, a time-domain aeroacoustics solver based on linearized Euler equations, was developed to obtain the far-field transfer functions. This process was previously found to yield noise directivities in reasonable agreement with those published in the literature and with engine test data. However, the drawback of this HiFi modeling approach was that it involved multiple computation steps, consisting of (a) CFD computation to generate the mean flow field, (b) mapping of the CFD-generated mean flow field to the acoustic mesh, and (c) computation of acoustic propagation through the mean flow field. Consequently, if the flow condition changes, then these steps must be repeated to compute the new far-field transfer functions. In the previous approach, the geometry was also detailed and not parametrizable, thus making simulations time-consuming to rerun when the geometry was altered. Furthermore, the time-domain linearized Euler equation solver (ACTRAN DGM) occasionally caused numerical instability problems, which posed difficulties in obtaining valid results in some situations.

In Year 3, the team aimed to improve the tool chain by replacing the HiFi modeling process with a new ROM with more parametrizable geometry and a simplified mean flow field, as shown in Figure 79. As illustrated in Figure 79, the new (FE-based) ROM process consolidated some of the steps into a single step, thus largely simplifying the far-field propagation tool chain.

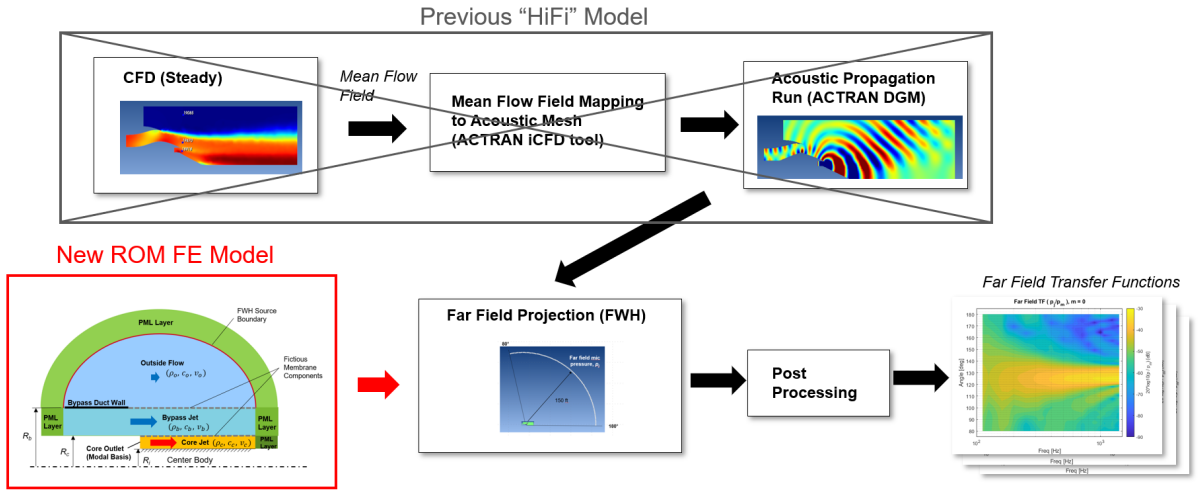


**Figure 79.** Simplified process for computing far-field transfer functions. The previous HiFi modeling consisting of multiple steps has been replaced with a new ROM.

This ROM models the engine aft geometry as simple concentric ducts that represent the core and the bypass duct components. The aft center body is also simplified as a simple cylinder instead of a conical shape. This geometry can be described by only several geometric parameters, such as the duct diameters, and thus is easily parametrizable. The mean flow field is also assumed to consist of three distinct regions of uniform flow that represent the core flow, the bypass flow, and the outer flow regions. Each of the three uniform flow regions is then characterized by three parameters, ($\rho$, $c$, and $v$), which are the density, speed of sound, and velocity. Another notable aspect of this ROM is the use of ACTRAN/TM, a frequency-domain aeroacoustic solver based on Mohring's wave equation. The main advantage of using this frequency-domain solver is that, unlike ACTRAN/DGM, it does not have the numerical instability problem, thus making the computation process more robust.

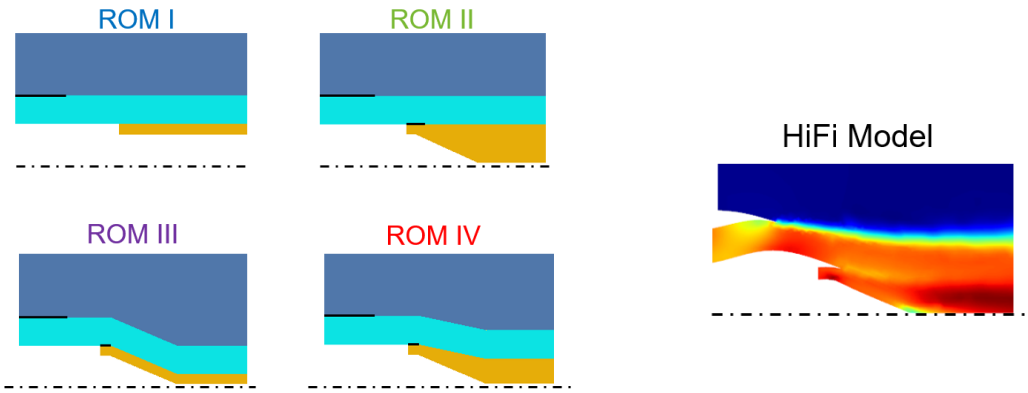


**Figure 80.** Four versions of the ROM and the reference HiFi model.

To understand the impact of the geometry and flow simplifications on the far-field acoustic pressures, we created several versions of the ROM with strategically varied geometries. Figure 80 shows four versions of ROM (labeled I to IV): ROM I is the simplest, and ROM IV is closest in geometry to the HiFi model shown on the right.

Figure 81 shows a comparison of far-field ROM results against that of the HiFi model. As shown in Figure 81(a), some differences exist in the far-field acoustic pressures between the ROM I and the HiFi model. Subsequently, the agreement is improved when the ROM geometry is made more similar to that of the HiFi model (by going from ROM I to ROM IV).

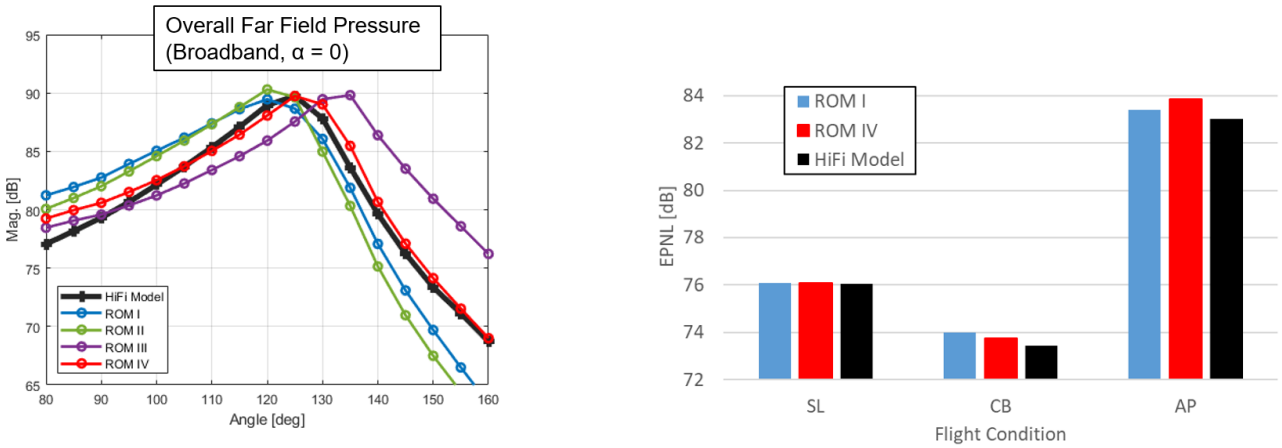


**(a)** **(b)**

**Figure 81.** Far-field ROM results versus the HiFi model: (a) overall far-field pressures, and (b) EPNL values.

Figure 81(b) below shows the equivalent perceived noise level (EPNL) values computed with ANOPP, a system-level noise prediction code, for the four ROM cases and the HiFi model for three different flight conditions: sideline, cutback, and approach. (Of note, EPNL values are computed on the basis of the assumption that no sources of noise exist other than the core noise. Moreover, the scaling is arbitrary, because noise sources of arbitrary magnitudes are used.) As shown in the figure, the differences in EPNL values among ROM I, ROM IV, and the HiFi model were generally small (less than 1 dB EPNL). This finding suggested that the EPNL values are relatively insensitive to small changes, such as the directivity peak angle shift indicated in Figure 81(a). A comparison of the results across all three flight conditions suggested little benefit in making the geometry more realistic by going from ROM I to ROM IV in terms of EPNL values. Therefore, ROM I with largely simplified geometry appears to be sufficient.

The far-field propagation ROM process developed during Year 3 represents a significant improvement over the previous modeling process in terms of robustness, practicality, and usability as a modeling tool. The process was further streamlined by reducing the number of computational steps necessary to compute far-field transfer functions. A more robust aeroacoustics solver was also used as the computational engine, thus eliminating the problem of numerical instability occasionally encountered when the solver was used for the previous modeling approach. The more parametrized nature of this tool also facilitates computing far-field transfer functions for a variety of engine geometry and flight conditions, thereby enabling more extensive investigations into the physics of combustion noise far-field propagation by running large numbers of simulations with a wide range of geometry and flow conditions. Finally, “generalized” far-field transfer functions including geometry and flow parameters can be obtained in the future.

## Milestones

- Development of an LNSE model for predicting direct and indirect noise, whose results compare favorably with the rig measurements.
- Creation of a far-field ROM FE model and validation against the HiFI model

## Major Accomplishments

A model decomposition technique based on SPOD was used to identify the key entropy and pressure related modes within the combustor. The SPOD identified a longitudinal acoustic mode (at 2500 Hz) as well as a lower-frequency mode (near 700 Hz) that is primarily entropy driven. This entropy mode is affected by the convection of the entropy perturbation from the flame to the dilution jet and further to the jail bars. At close to 700 Hz, the convection time scales of the entropy perturbation from the flame to the dilution jet and from the dilution jets to the jail bars are almost in phase, thus

reinforcing the perturbation at this frequency. The SPOD analysis also shows the rapid decay of the entropy at high frequencies and helps explain the low-frequency nature of the entropy noise from combustors.

Linearized Navier-Stokes computations were introduced to predict the direct and indirect noise by using the mean flow field within the combustor and unsteady HRR at the flame. The result of this approach compares favorably with measurements in the RTRC rig. Therefore, this approach may be viable for combustor noise prediction. Currently the mean flow field and the unsteady HRR are both obtained from the full LES computation. Future efforts will validate this approach by using the mean flow field computed with a Reynolds-averaged Navier–Stokes equation simulation and ROM for the unsteady HRR.

The nozzle interaction task has been completed. Results from Year 2 and carrying into Year 3 have shown that ADT applied to a 1D nozzle agrees reasonably well with LBM for upstream generated noise. The downstream generated noise was not easily identified from the rig tests; therefore, further model exploration was not considered. Instead, we focused on the turbine wave interaction task, which was considered more relevant to a real engine and noise prediction toolchain development.

For the turbine wave interaction task, related to direct noise, simulations and comparison to analytical models substantiated that a large amount of sound power is dissipated in the turbine stage through vorticity generation. A correction term was proposed that accounts for sound power dissipation effects in ADT. For indirect noise, entropy wave transport was simulated, and the sound generation mechanism inside the turbine was studied, including the modal content of the pressure field. The effect of cut-off mode creation from entropy waves inside the turbine was also investigated, and sound power remained generated at the cut-on plane wave mode. Entropy wave dispersion was investigated inside the turbine stage, and a transfer function for each row and a combined transfer function for the full stage were calculated according to HiFi simulation results. A generic velocity profile model was implemented, and a correction term to ADT was proposed that accounts for entropy wave dispersion effects in the noise prediction model.

For the far-field propagation modeling task, a ROM FE model was developed to further parametrize and streamline the far-field prediction tool. The ROM model predictions were compared and validated against the previous HiFi model in terms of far-field acoustic pressures and EPNL values for the three certification flight conditions.

## Publications
None.

## Outreach Efforts
None.

## Awards
None.

## Student Involvement
None.

## Plans for Next Period
1. The LES flow field from GT will be further interrogated to obtain direct noise estimates. An approach based on proper orthogonal decomposition is currently being evaluated to separate important effects within the combustor that contribute to direct and indirect noise.
2. For the nozzle interaction task, the team will further evaluate and refine the tools and processes developed for the RTRC rig and will then apply them to the GT rig for further validation and cross-comparison.
3. For the turbine interaction task, the team will continue to improve the ADT to account for acoustic dissipation effects and will then perform parametric studies to investigate different source types of turbine–wave interaction. This effort will include spinning wave modes and higher-order modes entering the turbine stage and different turbine designs. The results will be compared with the ADT, to evaluate this theory against a more diverse set of source types. Additionally, we will apply the improved ROM to a multi-stage turbine design with parameter variations to provide insight into the effects of realistic turbine design features on the expected sound transmission behavior.